

# Development of four-terminal devices utilising thin-film solar cells

**Radha Krishnan**  
Kothandaraman

Photovoltaic Materials and Devices Group, ESE, EEMCS, TU Delft



# Development of four-terminal devices utilising thin-film solar cells

by

**Radha Krishnan**  
Kothandaraman

in partial fulfillment of the requirements for the Master of Science in

**Sustainable Energy Technology**

at the Delft University of Technology,  
to be defended publicly on Wednesday November 21, 2018 at 10:00 AM.

Student number: 4623169  
Supervisor: Dr. René. A. C. M. M. van Swaaij, TU Delft  
Thesis committee: Prof. Dr. Arno. H. M. Smets, TU Delft  
Dr. Henk van Zeijl, TU Delft  
Dr. ir. Rudi Santbergen, TU Delft  
Mr. Hans Linden, Solliance Solar Research

*This thesis is confidential and cannot be made public until November 21, 2018.*

An electronic version of this thesis is available at <http://repository.tudelft.nl/>.



# Acknowledgement

First of all, I would like to express my sincere gratitude to Dr. René van Swaij for guiding me out throughout the course of my thesis. I thoroughly enjoyed our conversations on weekly Friday meetings, gave me deeper insight on my topic and made me strive to achieve better results. I will forever be grateful to have been under your supervision. I thank you again for your immense support and motivation.

I would like to thank Mr. Marcel Simor and Mr. Hans Linden for providing me with solar cell samples and for being part of my graduation committee. Special thanks to Marcel for being a wonderful mentor and answering my endless queries.

I would like to thank Dr. ir Rudi Santbergen for helping me with my simulation doubts and always greeting me with a warm smile. Your insights have helped to understand optics in a better manner. I would like to thank Martijn Tijssen and Stefaan Heirman for helping me endlessly with fabrications and measurements.

I am thankful to Prof.dr. Arno Smets for agreeing to be a part of my graduation committee. You have been a source of inspiration and your online course fuelled my interest to pursue my Masters in Delft. I would like to thank Dr. Henk van Zeijl for sparing his time and being a part of my graduation committee.

I would like to thank Nasim, Robin and Juan Camilo for taking time out of their busy schedule to help me in my research progress. Special thanks to Thierry, Yifeng and Paolo for being extremely flexible with Amigo bookings. Thank you so much guys!

Next, I would like to thank my office buddies Venky, Michel, Sandeep and Taha for being so nice and providing me with best possible atmosphere to work in. Venky, I can't thank you enough for all your help from Amigo depositions till Latex code.

Thank you so much Anjali for being my go to person and words can't express my gratitude for being there for me through my thick and thin. Thank you so much Sathish anna and Kamalesh for making me feel at home away from home. You both have been my support system during difficult times. Thank you Dhyanu for helping me with my coding troubles.

Thank you Amma, KK, Jay and Choti for all your love and support. Special thanks to Shresta my beautiful new born niece for motivating me to finish my thesis soon so that I could go and see her.

*Radha Krishnan K  
Delft, November 2018*



# Abstract

Single junction solar cells suffer from two primary loss mechanisms due to spectral mismatch: thermalisation and non-absorption losses. A photon with energy greater than the bandgap of the solar cell can be absorbed to excite an electron-hole pair and the excess energy received is released as heat constituting thermalisation losses. On the other hand, a photon with energy lower than the bandgap of the solar cell is not absorbed and leads to non-absorption losses. William B. Shockley and Hans-Joachim Queisser worked out the theoretical efficiency limit of the single junction solar cell based on the spectral mismatch and assuming band-to-band recombination, arrived at a conclusion that the maximum possible theoretical efficiency of a single junction solar cell is 33.1%.

To go beyond the theoretical efficiency limit, a high bandgap solar cell (top cell) can be optically coupled to a low bandgap solar cell (bottom cell) such that the high energetic photons are absorbed in the top cell and the non-absorbed photons from the top cell in the bottom cell. This explains the principle of tandem solar cells. In this work, a tandem solar cell structure known as four terminal device (4TD) is utilised. In a four terminal device tandem cell, the top and bottom cells are mechanically stacked together to have the same optical path, but are electrically isolated to ensure independent performance. This reduces the fabrication complexity involved in a two terminal tandem device structure.

To access the efficiency potential of various 4TD configurations before the actual fabrication of such devices, a theoretical model was derived in this work. The model predicted an absolute efficiency gain of 2% in the bottom cell for a combination of a-SiO<sub>x</sub>:H-CIGS (top cell-bottom cell) and a 3.5% efficiency gain for a a-SiO<sub>x</sub>:H-CIS devices. Based on the theoretical model, different combinations of 4TD's were fabricated. All such devices showed a gain in efficiency in the bottom cell and the combination of a lower bandgap a-SiO<sub>x</sub>:H-CIS devices showed a maximum efficiency gain of 4.40%.

The performance analysis of different combinations of 4TD's revealed that the extent of efficiency gain in the bottom cell is higher for a low performing bottom cell and the potential of the current 4TD configuration is limited by the transmission of the top cell. Using GenPro4 simulations, the optical system of the 4TD were analysed and possible solutions were explored. The infrared (IR) transmission of the top cell showed a drastic improvement from 55% to 80% by replacing the Asahi substrate with textured IO:H substrate. The new optimised top cell possess a combination of excellent spectral response in shorter wavelength and a good transparency in the IR region, thus making it more suitable for high efficiency 4TD configuration.



# Contents

<b>List of Figures</b>	<b>ix</b>
<b>List of Tables</b>	<b>xiii</b>
<b>1 Introduction</b>	<b>1</b>
1.1 The need for a clean and green energy . . . . .	1
1.2 Working of a solar cell. . . . .	2
1.3 Spectral utilisation . . . . .	3
1.3.1 Two terminal devices (2TD) . . . . .	6
1.3.2 Four terminal devices (4TD) . . . . .	6
1.4 Goal and outline of this thesis. . . . .	7
<b>2 Experimental methodology</b>	<b>9</b>
2.1 Sample Preparation . . . . .	9
2.2 Fabrication . . . . .	9
2.2.1 Plasma enhanced chemical vapour deposition. . . . .	9
2.2.2 RF magnetron sputtering . . . . .	10
2.2.3 Metal evaporation . . . . .	11
2.3 Thin-film characterisation . . . . .	11
2.3.1 Activation energy Measurements . . . . .	11
2.3.2 Spectroscopic ellipsometry . . . . .	12
2.3.3 Spectrophotometry . . . . .	12
2.4 Solar cell characterisation. . . . .	13
2.4.1 Illuminated Current density-Voltage (J-V) . . . . .	13
2.4.2 External Quantum Efficiency (EQE) . . . . .	14
2.4.3 Calculation of Efficiency . . . . .	15
<b>3 Theoretical efficiency determination of four terminal devices</b>	<b>17</b>
3.1 Four terminal devices - 4TD. . . . .	17
3.1.1 Spectral Photovoltaic-output. . . . .	18
3.2 Figures of merit - Top cell . . . . .	19
3.2.1 High $V_{OC} \times FF$ product . . . . .	19
3.2.2 External Quantum Efficiency (EQE) . . . . .	19
3.2.3 Transparency . . . . .	21
3.3 Effect of the top cell on the bottom cell . . . . .	21
3.3.1 Variation of $J_{SC}$ of the bottom cell . . . . .	22
3.3.2 $V_{OC} \times FF$ product of the bottom cell . . . . .	23
3.4 Theoretical determination of efficiency of a 4TD . . . . .	24
3.5 Conclusion . . . . .	25
<b>4 Fabrication of a-SiO<sub>x</sub>:H solar cell with high <math>V_{OC} \times FF</math> product</b>	<b>27</b>
4.1 Thin film material properties as a function of growth rate. . . . .	27
4.2 Optimisation of a-SiO <sub>x</sub> :H solar cell based on growth rate of DYK . . . . .	28
4.2.1 Reference a-SiO <sub>x</sub> :H solar cell. . . . .	28
4.2.2 Optimisation of p-layer . . . . .	29
4.2.3 Optimisation of n-layer . . . . .	32
4.2.4 Fabrication of solar cell with high $V_{OC} \times FF$ product . . . . .	34
4.2.5 Comparison with Cell A . . . . .	35
4.3 Conclusion . . . . .	36

<b>5</b>	<b>Analysis of various a-SiO<sub>x</sub>:H solar cell stacks</b>	<b>37</b>
5.1	Motivation . . . . .	37
5.2	Analysis based on figures of merit. . . . .	38
5.2.1	$V_{OC} \times FF$ product . . . . .	38
5.2.2	External Quantum Efficiency (EQE) . . . . .	39
5.2.3	Transmission of the top cell . . . . .	39
5.2.4	Theoretical efficiency determination of 4TD using different top cell stacks . . . . .	40
5.3	Top cell characterisation . . . . .	42
5.3.1	External quantum efficiency (EQE) . . . . .	42
5.3.2	Transmission of the top cell . . . . .	43
5.3.3	$V_{OC} \times FF$ product . . . . .	44
5.4	Conclusion . . . . .	44
<b>6</b>	<b>Fabrication and characterisation of four terminal devices</b>	<b>45</b>
6.1	Fabrication of 4TD . . . . .	45
6.1.1	Top cell fabrication . . . . .	45
6.1.2	Bottom cell fabrication. . . . .	46
6.1.3	4TD fabrication . . . . .	47
6.2	Characterisation of 4TD. . . . .	48
6.2.1	a-SiO <sub>x</sub> :H (2.03 eV)-CIGS configuration . . . . .	48
6.2.2	a-SiO <sub>x</sub> :H (1.96 eV)-CIGS configuration . . . . .	48
6.2.3	a-SiO <sub>x</sub> :H (2.03 eV)-CIS configuration . . . . .	51
6.2.4	a-SiO <sub>x</sub> :H (1.96 eV)-CIS configuration . . . . .	52
6.3	Limitation of the current 4TD configuration . . . . .	54
6.4	Conclusion . . . . .	55
<b>7</b>	<b>Optical analysis of a-SiO<sub>x</sub>:H solar cell using GenPro4 simulations</b>	<b>57</b>
7.1	Motivation . . . . .	57
7.2	Optical simulation of a-SiO <sub>x</sub> :H solar cell . . . . .	58
7.2.1	Optical simulation of top cell with back contact . . . . .	58
7.2.2	Optical simulation of top cell on a flat substrate . . . . .	60
7.3	Reduction of parasitic absorption in the top cell . . . . .	61
7.4	Reduction of reflection losses . . . . .	63
7.5	Efficiency potential of a-SiO <sub>x</sub> :H solar cell as top cell . . . . .	65
7.6	Conclusion . . . . .	66
<b>8</b>	<b>Conclusions and Recommendations</b>	<b>67</b>
8.1	Conclusions. . . . .	67
8.2	Recommendations . . . . .	67
	<b>Bibliography</b>	<b>69</b>
<b>A</b>	<b>Appendix A</b>	<b>75</b>
<b>B</b>	<b>Appendix B</b>	<b>77</b>
B.1	Electrical parameters of p-layer for different RF power . . . . .	77

# List of Figures

1.1	Consumption pattern of different sources of energy over the last 15 years [1]. . . . .	1
1.2	(A) Representation of a semiconductor material with bandgap $E_G$ ; and (B) A simple model to explain working of a solar cell [2]. . . . .	2
1.3	Representation of (A) Non-absorption losses; and (B) Thermalisation losses [2]. . . . .	3
1.4	Variation of photon flux of Sun's spectrum with wavelength and photon energy. . . . .	4
1.5	Theoretical efficiency limit of a single junction solar cell with indication of primary losses [2]. . . . .	4
1.6	Theoretical efficiency limit (a) 2 Terminal devices (2TD); and (b) 4 Terminal devices (4TD) [3]. . . . .	5
1.7	Perovskite-c-Si 2 terminal tandem solar cells [4]. . . . .	6
1.8	Perovskite-c-Si 4 terminal tandem solar cells [4]. . . . .	7
2.1	Representation of a PECVD chamber [5]. . . . .	10
2.2	Representation of RF magnetron sputtering chamber, image courtesy: Dr.Rene van Swaaij. . . . .	10
2.3	Representation of a metal evaporation system [6]. . . . .	11
2.4	Schematic representation of an ellipsometry measurement [7]. . . . .	12
2.5	(A)Schematic representation of a transmittance measurement in an IS; and (B)Schematic representation of a reflectance measurement in an IS [8]. . . . .	13
2.6	J-V curve of a-SiO <sub>x</sub> :H solar cell. . . . .	14
2.7	Schematic representation of EQE setup [9]. . . . .	14
2.8	EQE and 1-R plot of a-SiO <sub>x</sub> :H solar cell. . . . .	15
3.1	(A) the loss mechanism in Shockley-Queisser limit [2]; and (B) representation of a four terminal device. . . . .	17
3.2	(A)spectral PV output of a CIGS solar cell; and (B)comparison of spectral PV output of a CIGS solar cell with spectral irradiance. . . . .	18
3.3	Schematic representation of CIGS solar cell indicating thickness of each layer in the device stack[10]. . . . .	19
3.4	Comparison of EQE of a-SiO <sub>x</sub> :H with CIGS solar cell. . . . .	20
3.5	(A)spectral PV output of a-SiO <sub>x</sub> :H solar cell; and (B)spectral gain in the CIGS solar cell with a-SiO <sub>x</sub> :H solar cell as the top cell. . . . .	20
3.6	Transmission of the a-SiO <sub>x</sub> :H solar cell. . . . .	21
3.7	Spectral irradiance (A) on the top cell; and (B) on the bottom cell. . . . .	22
3.8	Comparison between the measured and calculated EQE - (A) method 1; and (B) method 2. . . . .	23
3.9	$V_{OC} \times FF$ product of the CIGS solar cell at different illuminated light intensity. . . . .	24
4.1	Simplistic representation of the deposition process of thin films by a plasma source [11]. . . . .	27
4.2	Comparison of EQE of Reference solar cell and Cell A. . . . .	29
4.3	Effect of RF power on the growth rate of p-a-SiO <sub>x</sub> :H layer (the dotted line represents the growth rate of DYK). . . . .	29
4.4	Effect of RF power on $E_{04}$ and $\sigma(D)$ of p-a-SiO <sub>x</sub> :H layer. . . . .	30
4.5	EQE comparison of the reference solar cell with optimised p-layer. . . . .	31
4.6	EQE response of solar cell with 7 nm and 10 nm thick p-layer. . . . .	32
4.7	Effect of RF power on the growth rate of n-nc-SiO <sub>x</sub> :H layer (the dotted line represents the growth rate of DYK). . . . .	32
4.8	Effect of RF power on $E_{04}$ and $\sigma(D)$ of n-nc-SiO <sub>x</sub> :H layer. . . . .	33
4.9	EQE and 1-R comparison of cell B with solar cell with 14 W n-layer. . . . .	34
4.10	Refractive index ( $n$ ) as a function of wavelength for n-nc-SiO <sub>x</sub> :H at 10 W and 14 W. . . . .	34
4.11	External parameters of a-SiO <sub>x</sub> :H with varying i-layer thickness (A) open circuit voltage; and (B) fill factor; and (C) short circuit current; and (D) efficiency. . . . .	35
4.12	Comparison of the Cell D with Cell A. . . . .	36

5.1	Schematic representation of a-SiO <sub>x</sub> :H solar cell stack. A back contact is deposited at the bottom of the stack after carrying out reflectance and transmittance measurements. . . . .	37
5.2	Reflectance and transmittance measurement of a-SiO <sub>x</sub> :H solar cell stacks. . . . .	38
5.3	Comparison of the solar cells based on their $V_{OC} \times FF$ product. . . . .	38
5.4	Comparison of EQE of solar cells on different substrates: (a) 130 nm i-layer; and (b) 200 nm i-layer. . . . .	39
5.5	Comparison of transmission of solar cells on different substrates: (a) 130 nm i-layer; and (b) 200 nm i-layer. . . . .	40
5.6	EQE of the CIGS solar cell in different 4TD configuration. . . . .	41
5.7	Efficiency contribution of the top and bottom cell in a 4TD configuration. . . . .	41
5.8	$V_{OC} \times FF$ product of CIGS solar cell at various $J_{SC}$ . . . . .	42
5.9	Comparison of EQE of various high bandgap solar cells in PVMD group with perovskite solar cell. . . . .	43
5.10	Comparison of transmission of various high bandgap solar cells in PVMD group with perovskite solar cell. . . . .	43
6.1	Top cell design layout. . . . .	45
6.2	Methodology for taking out external wiring from the solar cell. . . . .	46
6.3	CIGS/CIS solar cell layout utilised in this work. . . . .	46
6.4	Methodology for taking out external wiring from the front contact of the bottom cell. . . . .	47
6.5	Image of 4TD with a-SiO <sub>x</sub> :H top cell and CIS bottom cell. . . . .	47
6.6	Variation in short-circuit current of CIGS in stand alone configuration and as a bottom cell with 2.03 eV(left) and 1.96 eV(right) a-SiO <sub>x</sub> :H top cell. . . . .	49
6.7	Variation in open-circuit voltage of CIGS in stand alone configuration and as a bottom cell with 2.03 eV(left) and 1.96 eV(right) a-SiO <sub>x</sub> :H top cell. . . . .	49
6.8	Variation in fill factor of CIGS in stand alone configuration and as a bottom cell with 2.03 eV(left) and 1.96 eV(right) a-SiO <sub>x</sub> :H top cell. . . . .	50
6.9	Variation in shunt resistance of CIGS in stand alone configuration and as a bottom cell with 2.03 eV(left) and 1.96 eV(right) a-SiO <sub>x</sub> :H top cell. . . . .	50
6.10	Efficiency comparison of CIGS in stand alone configuration and as a bottom cell with 2.03 eV(left) and 1.96 eV(right) a-SiO <sub>x</sub> :H top cell. . . . .	50
6.11	EQE comparison of CIGS and CIS solar cell. . . . .	51
6.12	Variation in short-circuit current of CIS in stand alone configuration and as a bottom cell with 2.03 eV(left) and 1.96 eV(right) a-SiO <sub>x</sub> :H top cell. . . . .	52
6.13	Variation in open-circuit voltage of CIS in stand alone configuration and as a bottom cell with 2.03 eV(left) and 1.96 eV(right) a-SiO <sub>x</sub> :H top cell. . . . .	53
6.14	Variation in fill factor of CIS in stand alone configuration and as a bottom cell with 2.03 eV(left) and 1.96 eV(right) a-SiO <sub>x</sub> :H top cell. . . . .	53
6.15	Variation in shunt resistance of CIS in stand alone configuration and as a bottom cell with 2.03 eV(left) and 1.96 eV(right) a-SiO <sub>x</sub> :H top cell. . . . .	53
6.16	Efficiency comparison of CIS in stand alone configuration and as a bottom cell with 2.03 eV(left) and 1.96 eV(right) a-SiO <sub>x</sub> :H top cell. . . . .	54
6.17	Optical response of the a-SiO <sub>x</sub> :H (1.96 eV)-CIGS 4TD configuration. . . . .	55
7.1	(A) optical response of the current top cell; and (B) relative distribution of $J_A$ in the current top cell. . . . .	58
7.2	Absorption spectra of a-SiO <sub>x</sub> :H solar cell from GenPro4 simulations in comparison with the measured parameters. A 190-nm thick i-layer is used as input thickness to match the measured EQE of the solar cell. . . . .	59
7.3	Comparison between simulated and measured reflectance and transmittance of Asahi substrate. . . . .	59
7.4	Schematic representation of Cell A on a flat glass substrate. . . . .	60
7.5	Comparison of simulated and measured reflectance and transmittance of a-SiO <sub>x</sub> :H solar cell on a flat glass substrate. . . . .	60
7.6	(A) optical response of cell A; and (B) relative distribution of $J_A$ in Cell A. . . . .	61
7.7	Extinction coefficient of AZO and IO:H. . . . .	62
7.8	Schematic representation of Cell B. . . . .	62
7.9	(A) optical response of Cell B; and (B) relative distribution of $J_A$ in Cell B. . . . .	63

---

7.10 Schematic representation of Cell C. . . . .	64
7.11 (A) optical response of Cell C; and (B) relative distribution of $J_A$ in Cell C. . . . .	64
7.12 Simulated EQE of the 4TD using Cell C as the top cell. . . . .	65
A.1 Comparison of the transmission of different optical filters. . . . .	75



# List of Tables

3.1	Electrical parameters of CIGS solar cell from Solliance. . . . .	18
3.2	Electrical parameters of commonly used top cell in 4TD configuration. . . . .	19
3.3	Theoretical 4TD efficiency for different solar cells with a-SiO <sub>x</sub> :H solar cell as the top cell. . . . .	24
4.1	Growth rate of layer's in a-SiO <sub>x</sub> :H solar cell stack. . . . .	28
4.2	Deposition parameters of the reference a-SiO <sub>x</sub> :H solar cell [9]. . . . .	28
4.3	Comparison of electrical parameters of the reference solar cell with cell A [12]. . . . .	28
4.4	External parameters of a-SiO <sub>x</sub> :H solar cell with optimised p-layer. . . . .	31
4.5	External parameters of solar cell with variation of p-layer thickness. . . . .	31
4.6	External parameters of solar cell with optimised n-layer. . . . .	33
4.7	External parameters of solar cell with varying i-layer thickness. . . . .	35
4.8	External parameters of solar cell with optimised p and n-layer. . . . .	36
5.1	Ranking based on the figures of merit. . . . .	40
5.2	Electrical parameters of the CIGS solar cell - Solliance. . . . .	40
5.3	Electrical parameters of high bandgap solar cells fabricated in comparison with perovskite solar cell. . . . .	42
6.1	4TD efficiency for CIGS solar cells with a-SiO <sub>x</sub> :H (2.03 eV) solar cell as the top cell. . . . .	48
6.2	4TD efficiency for CIGS solar cells with a-SiO <sub>x</sub> :H (1.96 eV) solar cell as the top cell. . . . .	49
6.3	4TD efficiency for CIS solar cells with a-SiO <sub>x</sub> :H (2.03 eV) solar cell as the top cell. . . . .	51
6.4	4TD efficiency for CIS solar cells with a-SiO <sub>x</sub> :H (1.96 eV) solar cell as the top cell. . . . .	52
7.1	Electrical parameters of cells used in the efficiency estimation. . . . .	65
7.2	Theoretical 4TD efficiency for Cell C and CIGS configuration. . . . .	65
A.1	Average transmission of optical density filters used in this work . . . . .	75
B.1	Comparison of optical and electrical parameters of p layer with DYK. . . . .	77
B.2	Comparison of optical and electrical parameters of n-layer with DYK. . . . .	77



# Introduction

## 1.1. The need for a clean and green energy

Energy is derived from the utilisation of resources in any form and is the driving factor for life and economy in this world. As shown in Figure 1.1, the current energy demand is fulfilled by mainly utilising fossil fuels such as coal, oil and natural gas. These three resources are classically known as conventional fuels [13]. The global demand for energy has doubled during the last 40 years and is expected to increase by as much as an order of magnitude by 2050 [14]. The increase in energy demand is predominantly due to rise in population and per capita consumption of energy [15].

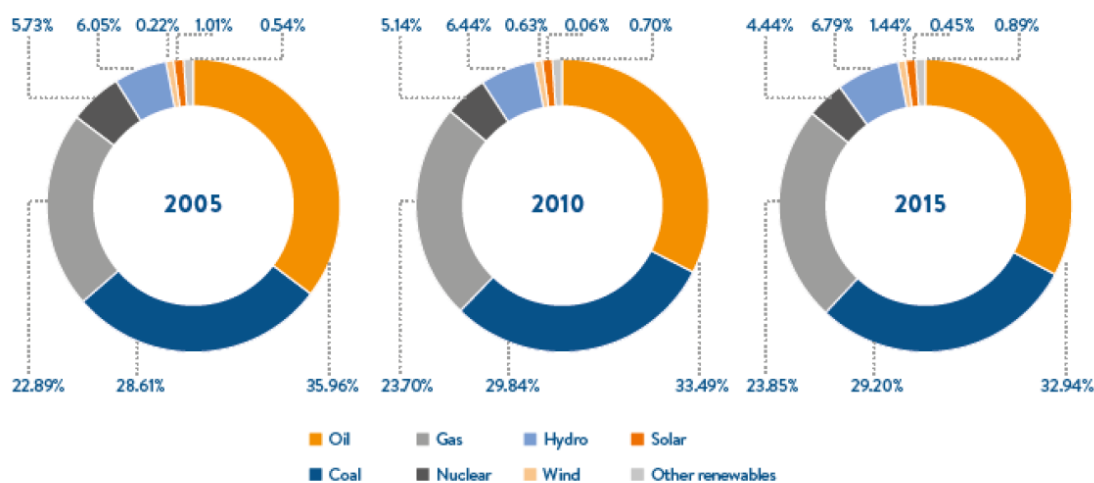


**Figure 1.1:** Consumption pattern of different sources of energy over the last 15 years [1].

Excessive exploitation of fossil fuels to meet the current energy demand results in faster depletion of the fossil fuel reserves [16]. Studies suggest that with the current rate of depletion, oil, gas and coal resources are expected to last only for 35, 37 and 107 years respectively [17]. Moreover, these reserves are concentrated in few countries leading to a monopoly in supply chain aspect of energy export. The monopoly can result in instability in the energy prices and impose concern over energy security of a country.

Apart from these aspects, the usage of fossil fuel has a profound impact on the environment. Burning of fossil fuels result in emission of large quantity of oxides of sulphur and nitrogen along with CO<sub>2</sub> [13]. Studies suggest that energy accounts for almost two-third of total greenhouse gas (GHG) emissions [18]. The increase in GHG results in the depletion of ozone layer and causes global warming. The extraction of energy from fossil fuel needs to be mitigated to ensure a low rate of GHG emissions and subsequently prevent the catastrophic

effect of climate change [19]. Considering the economic, geo-political and more importantly the environmental impacts of fossil fuels, a shift to a clean and green form of energy is essential. A way to achieve this is by shifting to a more sustainable form of energy.

Solar energy is one of the sustainable form of energy resources with highest theoretical energy potential [20]. A way of transforming solar energy to electricity is by using photovoltaic (PV) devices. In recent years, the PV technology is achieving grid parity in many locations owing to drop in production cost due to experience curve effects and upscaling of production units [21]. In this thesis, we will look into technological aspects of PV devices.

## 1.2. Working of a solar cell

A solar cell works on the principle of the photovoltaic effect. The photovoltaic effect is defined as the generation of a voltage or potential difference at the junction of two different materials upon exposure to incident light [2]. Albert Einstein[2] proved that the incident light is composed of discrete energy packets called photons, where each photon correlates to a quantum of energy ( $E$ ) depending on its oscillating frequency ( $\nu$ ) as given by Equation 1.1, where  $h$  is Planck's constant,  $c$  and  $\lambda$  are the speed and wavelength of the incident light respectively.

$$E = h\nu = \frac{hc}{\lambda} \quad (1.1)$$

Figure 1.2-(A) represents a semiconductor material with bandgap  $E_G$ . In an ideal semiconductor material, electrons can only occupy positions below the valence band edge  $E_V$  and above the conduction band edge  $E_C$ . The difference between the valence band and the conduction band defines the bandgap of a semiconductor material. An electron-hole pair is generated in a semiconductor material when a photon of energy  $E_{ph} \geq E_G$  is absorbed by an electron in the valence band.

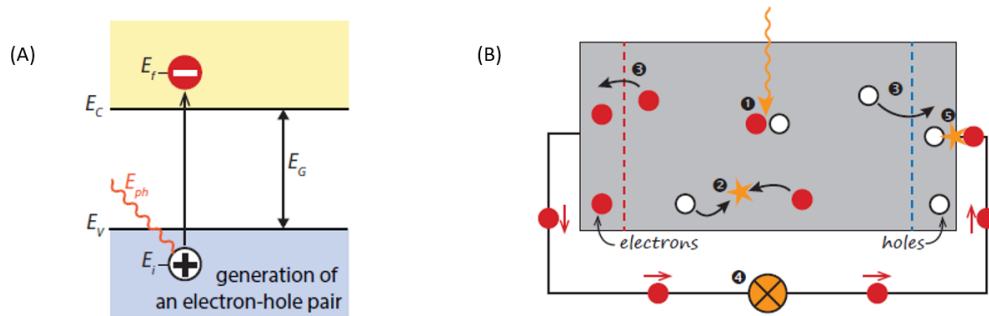


**Figure 1.2:** (A) Representation of a semiconductor material with bandgap  $E_G$ ; and (B) A simple model to explain working of a solar cell [2].

Working of a solar cell can be explained with the help of Figure 1.2-(B). The numbers in the Figure 1.2-(B) are explained as follows.

1. Photon with energy  $E_{ph} \geq E_G$  generates an electron-hole pair.
2. The generated electron-hole pair recombine and release energy in the form of photons or result in lattice vibrations. To extract useful work out of the generated electron-hole pair they need to be separated and not recombine.
3. To avoid recombination, an electron and hole selective membrane are placed on the sides of the absorber layer which aids the separation of generated electron-hole pair.
4. The energy stored in the separated electron is utilised by making it pass through an external electric circuit.
5. The electron recombine with hole after extraction of its stored energy.

### 1.3. Spectral utilisation

In this section, a brief description about primary losses involved in a single junction solar cells and about energy distribution in the sun's spectrum are discussed to give an overview about the spectral mismatch in a solar cell.

A single junction solar cell suffers from two primary losses known as thermalisation and non-absorption. As shown in the Figure 1.3-(A), photons with energy lower than the bandgap of a semiconductor material are not absorbed and constitute to non-absorption losses. Photons with energy greater than the bandgap of a semiconductor material are absorbed, but the difference in energy between the incident photon and the bandgap of the semiconductor material is released as heat and are referred to as thermalisation losses.

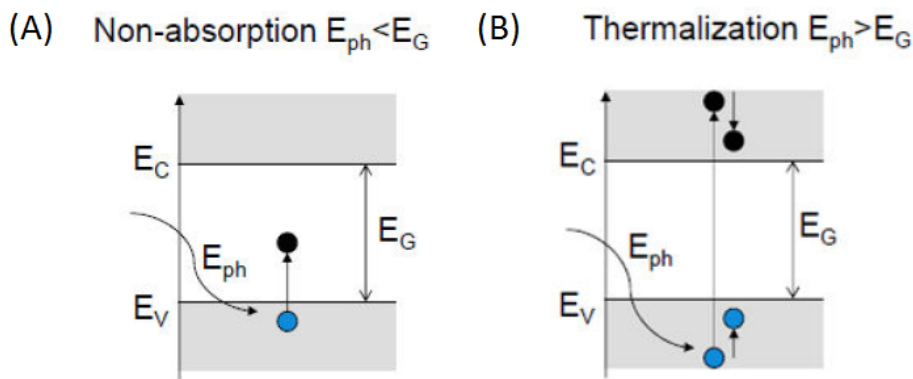
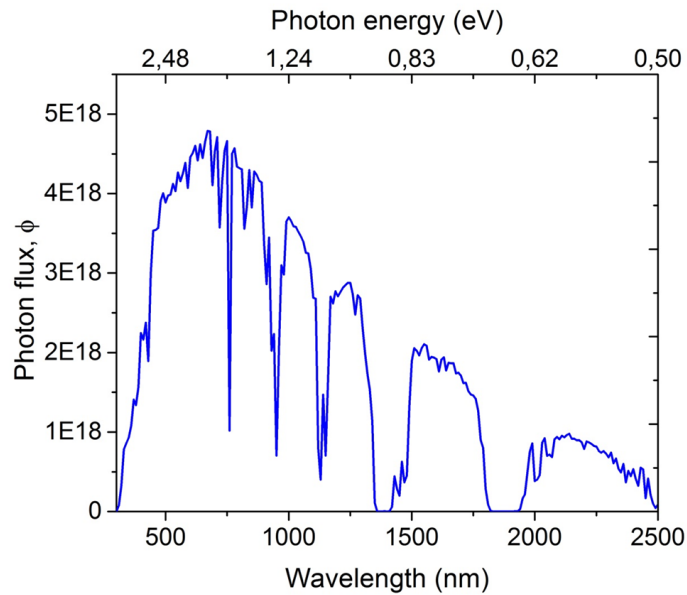


**Figure 1.3:** Representation of (A) Non-absorption losses; and (B) Thermalisation losses [2].

As mentioned in section 1.2, the light source is composed of photons with different energy quanta based on its wavelength. The total irradiance ( $I$ ) of the Sun's spectrum is given by Equation 1.2, where  $\phi(\lambda)$  defines the photon flux at wavelength  $\lambda$ . The integral range indicates the spectral range of Sun's spectrum.

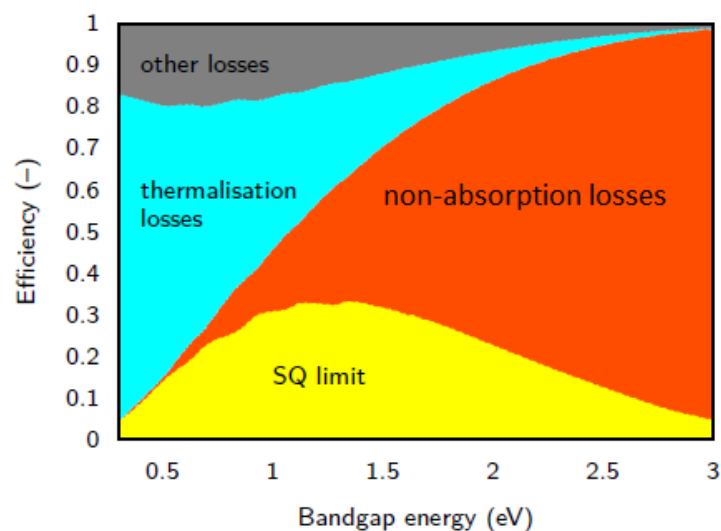
$$I = \int \frac{hc}{\lambda} \cdot \phi(\lambda) d\lambda = 1000 W m^{-2}. \quad (1.2)$$

Figure 1.4 shows the variation of photon flux in Sun's spectrum with respect to both wavelength and photon energy. The photon flux shows a gradual decrease with increasing wavelength. The variation of photon flux with photon energy results in uneven distribution of the Sun's energy. It is to be noted that about 90% of solar irradiance is obtained within a spectral range of 280 to 1400 nm.



**Figure 1.4:** Variation of photon flux of Sun's spectrum with wavelength and photon energy.

Depending on the mismatch of the available spectral energy and the bandgap of a semiconductor material, the extent of thermalisation and non-absorption losses tend to differ [8]. Taking spectral mismatch into consideration, William B. Shockley and Hans-Joachim Queisser worked out the theoretical efficiency limit of a single junction solar cell, which is widely known as Shockley-Queisser (S-Q) limit. Figure 1.5 represents the theoretical limit proposed by S-Q indicating the various losses involved in a solar cell. As per S-Q limit, a maximum theoretical efficiency of a single junction solar at A.M 1.5 spectrum is 33.1% for a solar cell with a bandgap of 1.34 eV [22].



**Figure 1.5:** Theoretical efficiency limit of a single junction solar cell with indication of primary losses [2].

The S-Q limit is based on direct bandgap semiconductor material, where major recombination mechanism is radiative recombination. For an indirect bandgap material like crystalline silicon in which Auger recombination is an important loss mechanism, an efficiency limit of 29.43% has been calculated by Richter et al. [23]. It is clear that the spectral losses limits the efficiency of a single junction solar cell and better spectral utilisation is required to go beyond the S-Q limit and Richter limit.

As shown in Figure 1.5, the high bandgap solar cells largely suffer from non-absorption losses whereas thermalisation losses dominate for the low bandgap solar cells [2]. To reduce these losses, a high bandgap solar cell (top cell) can be optically coupled to a low bandgap solar cell (bottom cell), such that, high energetic photons in the A.M 1.5 spectrum get absorbed in the top cell and the non-absorbed photons are absorbed in the bottom cell. This explains the concept of tandem solar cells.

Theoretical efficiency limit performed on tandem solar cell revealed that, a solar cell with infinite number of absorber layers can produce an efficiency of 68% under 1 sun light intensity and 88% under extreme conditions [24]. Practically, fabrication of such a device is extremely difficult. A more realistic approach is to limit the solar cell architecture with just two different absorber layers. A solar cell with two different absorber layers can either be formed by interconnecting them in series (2 terminal tandem) or in parallel (4 terminal tandem) configuration. Figure 1.6 shows the maximum theoretical efficiency potential of 2 terminal (2T) and 4 terminal (4T) devices as a function of bandgap of the top and bottom cell. These device structures will be discussed in more detail in the next section. A theoretical efficiency of about 46% is possible in both the configuration by tuning the bandgap of top and bottom cell [25]. The high efficiency potential of these devices motivate us to investigate further on 2T and 4T configuration and are discussed in the next section.

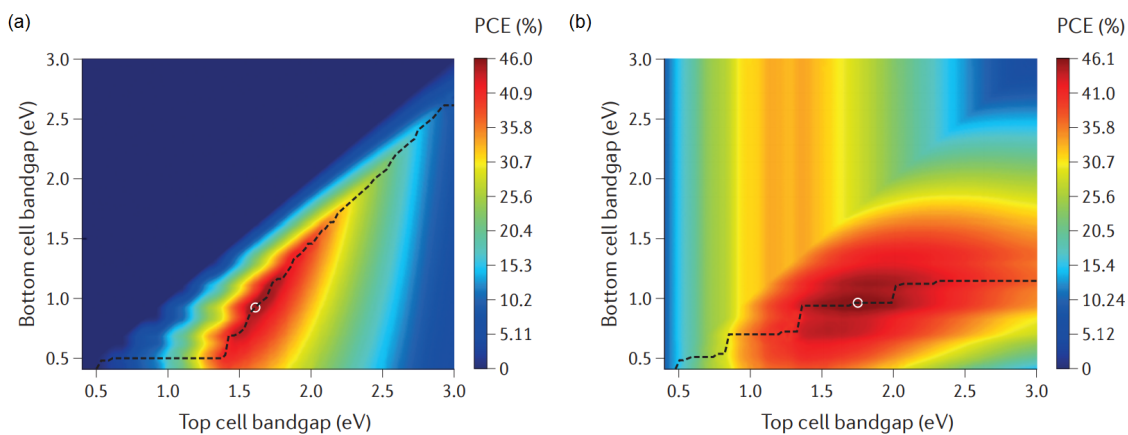


**Figure 1.6:** Theoretical efficiency limit (a) 2 Terminal devices (2TD); and (b) 4 Terminal devices (4TD) [3].

### 1.3.1. Two terminal devices (2TD)

Figure 1.7 shows the schematics of a 2TD configuration. The top cell used in this configuration is  $\text{CH}_3\text{NH}_3\text{PbI}_3$  perovskite solar cell with a bandgap of 1.63 eV [26] and bottom cell used is a silicon heterojunction solar cell with a bandgap of 1.1 eV. Perovskite based solar cells are widely used as a top cell in tandem devices due to their high absorption coefficient, tunable bandgap, sharp absorption edge and low production cost [27]. In this configuration, the top cell absorbs the high energetic photons and the photons not absorbed at the top cell are absorbed in the bottom cell. By this way, both the thermalisation and non absorption losses are minimised. The device gives a combined efficiency of 23.6% which is beyond the efficiency of both the individual solar cells.

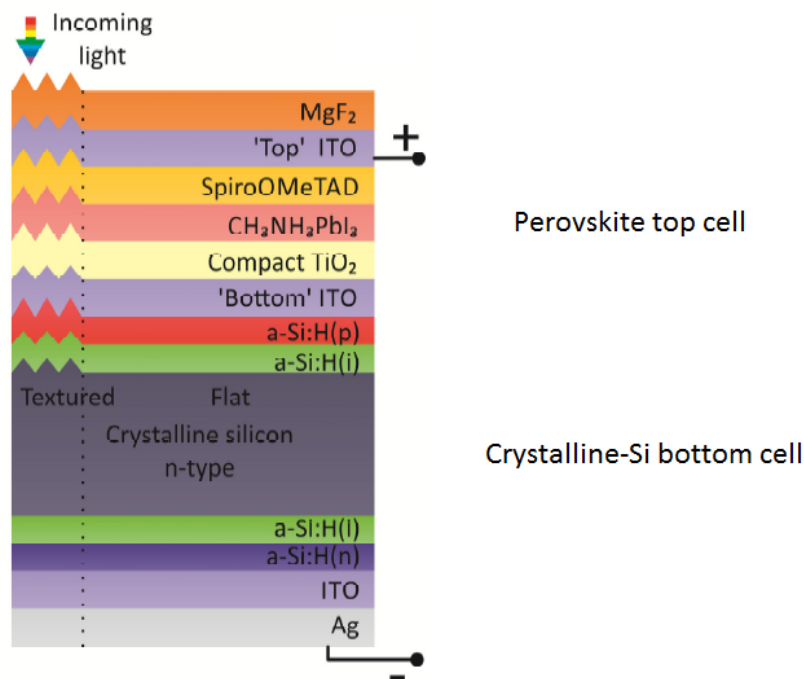


**Figure 1.7:** Perovskite-c-Si 2 terminal tandem solar cells [4].

As seen in Figure 1.7, the top cell is grown onto the surface of the bottom cell. The growth conditions of the top cell thus needs to be taken care of so as to not affect the working of the bottom cell. As the top and bottom cells are interconnected in a series configuration, the efficient operation of this configuration depends on the current matching between both the cells. The bandgap of the top cell and their absorber layer thickness needs to be chosen carefully to match the current of the bottom cell thus drawing constraints over choice of the top cell [28]. Moreover, the 2TD devices are extremely sensitive to spectral variation. The module performance gets severely affected at lower illumination level as the short-circuit current has a linear dependency on the intensity of irradiation [29]. These restrictions and drawbacks of 2TD configuration can be overcome with the help of a four terminal device configuration.

### 1.3.2. Four terminal devices (4TD)

Figure 1.8 shows the schematics of a 4TD configuration. The evident difference in the 4TD configuration in comparison to 2TD configuration is in the interconnection of the two cells. The top and bottom cells are independent entities and are mechanically stacked on each other to have the same optical path. The cells are electrically isolated by placing an insulating medium such as glass between each other. This allows independent operation of both the cells and also provides more flexibility in its design, enabling wide choice in top and bottom cells.

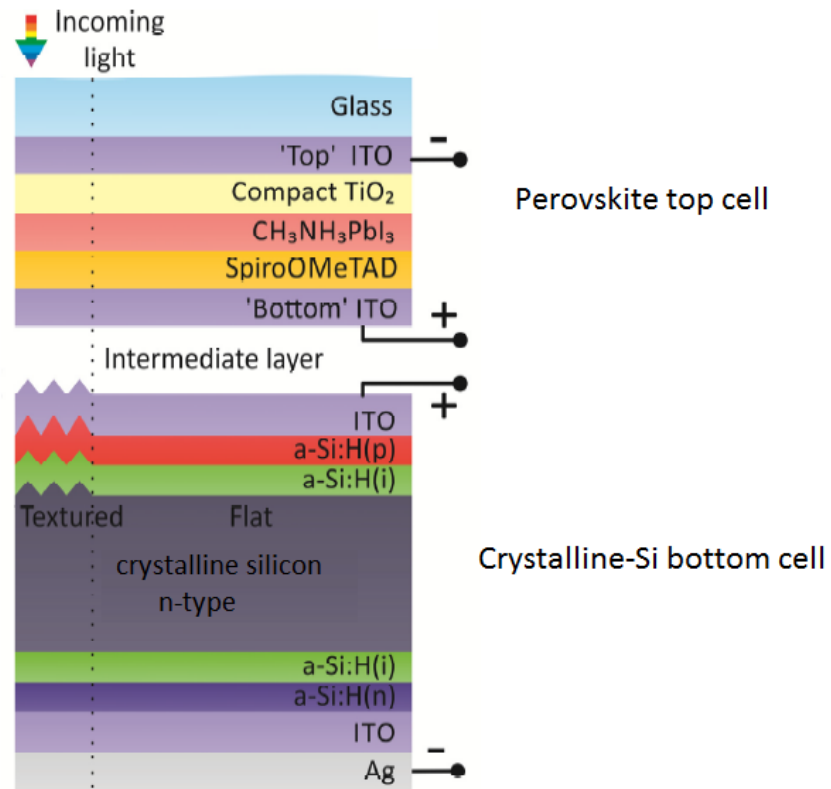


Figure 1.8: Perovskite-c-Si 4 terminal tandem solar cells [4].

In a 4TD configuration, separate inverter and MPPT controller systems are essential for efficient operation of top and bottom cell, thus adding to the cost of balance-of-system [28]. The optical path of light needs to travel through three layers of transparent conductive oxide to reach the absorber layer of bottom cell leading to increase in parasitic losses. In spite of these shortcomings, efficiency gain using 4TD configuration has been demonstrated with GaInP based top cell [30, 31] and Perovskite based top cell [28, 32] to name a few. Chaudhary [33] in his thesis work in the PVMD group, utilised an a-SiO<sub>x</sub>:H solar cell as top cell and demonstrated an efficiency gain of 0.5% using poly-Si solar cell as the bottom cell. In this work, an a-SiO<sub>x</sub>:H solar cell is utilised as top cell in combination with CIGS and CIS based solar cell to investigate the potential of a-SiO<sub>x</sub>:H solar cell as top cell in a 4TD configuration.

## 1.4. Goal and outline of this thesis

Among thin film silicon solar cells, the a-SiO<sub>x</sub>:H solar cell has a high  $V_{OC} \times FF$  product of 0.761 V [34]. A top cell based on a-SiO<sub>x</sub>:H solar cell would thus reduce the thermalisation losses by collecting the high energetic photons at a high  $V_{OC} \times FF$  product and possibly result in a gain in efficiency in a 4TD configuration. This makes a-SiO<sub>x</sub>:H an interesting candidate in the choice of top cell in a 4TD configuration.

But the demonstrated gain in efficiency using an a-SiO<sub>x</sub>:H solar cell as a top cell in a combination with c-Si based bottom cell is limited [33]. This motivates us to utilise a-SiO<sub>x</sub>:H solar cell on thin film solar cell such as CIGS/CIS solar cell which has a tunable bandgap and a wider spectral response range compared to that of a c-Si solar cell. The goal of this work is *to investigate the potential of a-SiO<sub>x</sub>:H solar cell as a top cell in a 4TD configuration.*

The structure of this thesis is as follows: In Chapter 2, the steps involved in sample preparation from cleaning till fabrication steps and ways to characterise the fabricated samples are discussed in detail. Design requirements for a top cell and a way to estimate the theoretical efficiency of a 4TD configuration are explained in detail in Chapter 3. Chapter 4 presents an overview on procedure adopted to fabricate a-SiO<sub>x</sub>:H solar cell with a high  $V_{OC} \times FF$  product. In chapter 5, various a-SiO<sub>x</sub>:H solar cell stacks are analysed based

on several figures of merit such as EQE,  $V_{OC} \times FF$  product and transmission. In chapter 6, development and characterisation of 4TD devices are carried out. Chapter 7 deals with the optical simulation which gives an idea about the potential of a-SiO<sub>x</sub>:H based top cell. Finally, the conclusion based on the research performed is summarised and recommendations are suggested in Chapter 8.

# 2

## Experimental methodology

This chapter is divided into 3 parts based on the chronological order in which experiments were carried out. The first section provides information regarding the cleaning procedure adopted in this work. The second section explains about all the fabrication techniques which were adopted for fabrication of thin film layers and solar cells. Finally, all the characterisation techniques used in this work are explained.

### 2.1. Sample Preparation

In this work, Corning glass XG and Asahi VU were used as substrate to carry out thin film depositions. A substrate dimension of 2.5 cm × 10 cm was used throughout the work. To carry out optical and electrical characterisation on individual thin film layers, they were deposited on Corning glass substrate and for solar cell fabrication, a textured fluorine doped tin oxide (Asahi VU) [35] substrate was used.

The primary and one of the most important step involved in fabrication of thin film sample is cleaning. Both Asahi Vu and Corning glass XG samples were cleaned by ultrasonic cleaning. In ultrasonic cleaning process, the cavitation bubbles generated by the sonic waves in the ultrasonic bath hits the surface of the substrate to remove dust, finger impressions and other particulate impurities to produce high quality sample for further processing [36]. The cleaning procedure adopted in this work involves two steps. First, the samples were cleaned in an ultrasonic bath with acetone for 15 minutes followed by drying it with nitrogen air. Next, the samples were cleaned in an ultrasonic bath with isopropanol (IPA) for 15 minutes followed by drying it with nitrogen air.

### 2.2. Fabrication

#### 2.2.1. Plasma enhanced chemical vapour deposition

In this work, the p, i and n thin film layers were deposited through radio-frequency plasma enhanced chemical vapour deposition (RF PECVD). Figure 2.1 represents a typical PECVD reaction chamber. The process chamber is maintained at ultrahigh vacuum using a combination of turbo-molecular and foreline pump and the temperature inside is maintained with the help of a heater. The chamber consist of two electrodes. The electrode at the top is grounded and has a provision to mount substrate. The electrode at the bottom is connected with an RF generator. Moreover, the bottom electrode is perforated to allow the flow of precursor gases [5]. A plasma is produced when the precursor gases are subjected to an oscillating electric field through an RF generator. The plasma results in generation of reactive radicals, ions and electrons. As the substrate is grounded and has at a lower potential compared to the plasma, it attracts positive and neutral ions enabling the thin film growth. The thin film growth occurs by adsorption of vapour phase gas particles on the substrate [8]. Depending on the material to be deposited, the gases that are fed to the chamber can be varied.

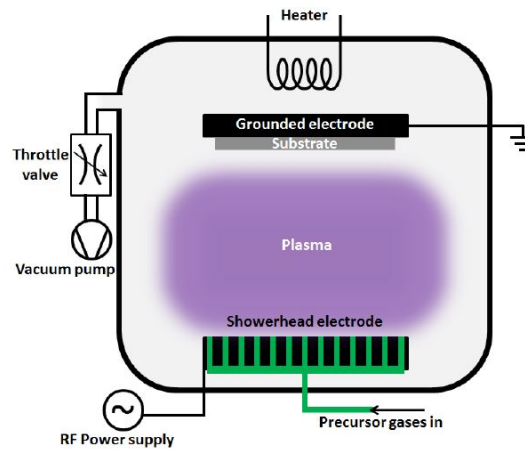


**Figure 2.1:** Representation of a PECVD chamber [5].

In this work, PECVD system called Amigo by Elettrovava S.p.A [37] was used for the deposition of both intrinsic and the doped layers. The system consist of six deposition processing chambers (DPC), a transfer chamber (TC) and a load lock chamber (LLC) with a provision to process 5 substrate. The p-type layer were processed in DPC1, n-type layer in DPC2, i-a-Si layer in DPC3 and i-a-SiO<sub>x</sub>:H layer in DPC5.

### 2.2.2. RF magnetron sputtering

In this work, depositions of transparent conductive oxide (TCO) were carried out using RF magnetron sputtering. It comes under the class of physical vapour deposition [2]. Figure 2.2 represents a typical RF magnetron sputtering system. The anode has a provision to mount the substrate and the cathode contains the target material. The process occurs in a vacuum chamber and in an inert argon atmosphere. An argon plasma is produced between the electrodes due to an oscillating electromagnetic field. The kinetic energy of the produced argon ions is utilised and used to bombards the surface of the target material, resulting in ejection of atoms from the target material [2]. The released target atom, evaporates and diffuses towards the anode (substrate) and facilitates the growth of the thin film.

In this work, the depositons of aluminum-doped zinc oxide (AZO) were carried out in DPC6 of Amigo. The chamber contains a ceramic target of 2 % Al<sub>2</sub>O<sub>3</sub> and 98 % ZnO by weight. Deposition of indium-doped tin oxide (ITO) was carried out in a sputtering unit called as Zorro. The ITO targets consist of 10 % SnO<sub>2</sub> and 90 % In<sub>2</sub>O by weight.

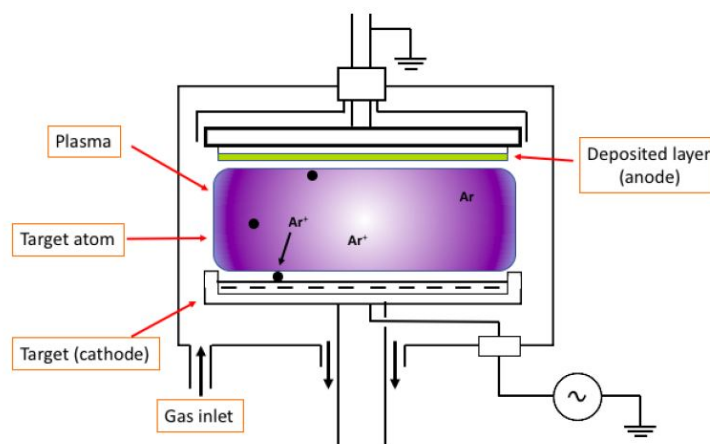


**Figure 2.2:** Representation of RF magnetron sputtering chamber, image courtesy: Dr.Rene van Swaaij.

### 2.2.3. Metal evaporation

In this work, front metal contact and back metal contact for the solar cells and metal contacts on the individual thin film layers were deposited through evaporation. Evaporation can be carried out by either thermal evaporation or electron beam evaporation. In thermal evaporation, the target material placed in a crucible is heated through passage of a high current [2]. In electron beam evaporation, the target material is placed in a crucible and an intense electron beam is channelised on the target material which heats up the target [2]. In both the process, the target source starts to evaporate as its melting point is reached.

Figure 2.3 represents the metal evaporation unit (Provac) used in this work. The process chamber is maintained at vacuum to reduce oxide formation in metallic film and also to have a control over deposition [38]. The sample stages is rotated at a speed of 10 RPM to improve the homogeneity of the metal layer [38]. The deposition rate of the process is monitored through a quartz crystal rate monitor. Chromium and aluminium depositions were evaporated using an e-beam evaporation technique and silver depositions were carried out using thermal evaporation.

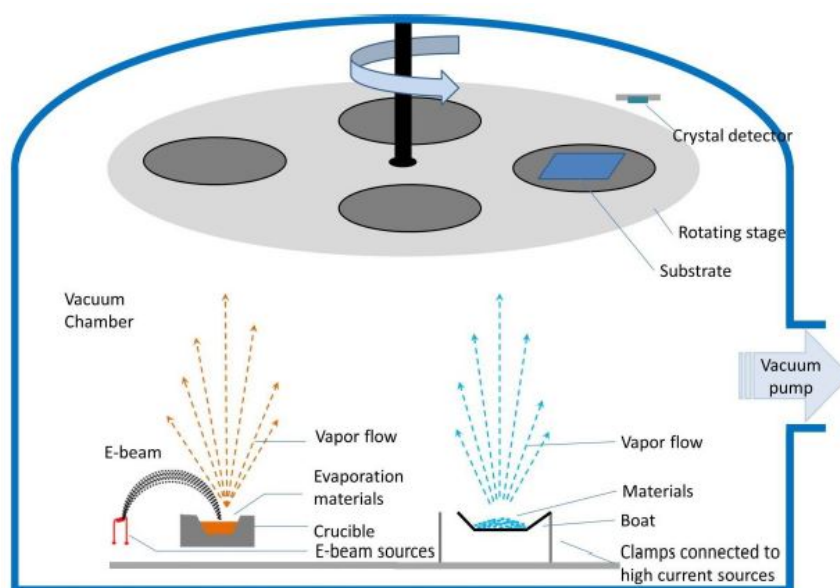


Figure 2.3: Representation of a metal evaporation system [6].

## 2.3. Thin-film characterisation

A thin-film solar cell consists of several individual thin-film layers with different material, optical and electrical properties. Depending on the thin-film layers deposited, the performance of the solar cell gets altered. Hence, each and every layer deposited needs to be characterised optically and electrically to optimise the solar cell. In this section, the optical and electrical characterisation technique used in this work are explained.

### 2.3.1. Activation energy Measurements

Activation energy measurements are carried out to evaluate the extent of doping in a semiconductor layer. For an n-doped layer, the activation energy  $E_a$  is the difference between the energy level in the conduction band ( $E_C$ ) and the fermi energy level ( $E_F$ ). For a p-doped layer, the activation energy  $E_a$  is the difference between the energy level in the valence band ( $E_V$ ) and the fermi energy level ( $E_F$ ). At a particular temperature ( $T$ ), the dark conductivity ( $\sigma_D(T)$ ) of a material can be correlated to  $E_a$  with the help of Arrhenius equation.

$$\sigma_D(T) = \sigma_0 \cdot e^{-E_a/kT} \quad (2.1)$$

where  $\sigma_0$  represents conductivity pre-factor,  $T$  is the temperature in Kelvin and  $k$  is the Boltzmann's constant. The  $E_a$  can be obtained from the slope of a plot between  $\ln(\sigma_D)$  and  $1/kT$ .

In this work, the thin film layers were deposited on glass sample and a 300-nm thick Al coplanar contacts were evaporated on the samples and were annealed at 130° C for 30 minutes. The samples were placed in

a temperature controlled stage and were connected to an electrometer. The conductance of the sample was measured in dark for different temperature ranges and activation energy was obtained using Equation 2.1.

### 2.3.2. Spectroscopic ellipsometry

In this work, the thickness, optical bandgap ( $E_{04}$ ), refractive index ( $n$ ) and extinction coefficient ( $k$ ) value of thin film layers were obtained using spectroscopic ellipsometry. Spectroscopic ellipsometry is a non-destructive measuring technique which can also be adopted to characterise surface roughness, composition and grading profile of a material [39]. All the measurements in this work were carried out using M-2000DI spectrometer from J.A. Woolam Co. Inc. The equipment is capable of data acquisition from a wide range of spectra from 193 nm to 1690 nm [40].

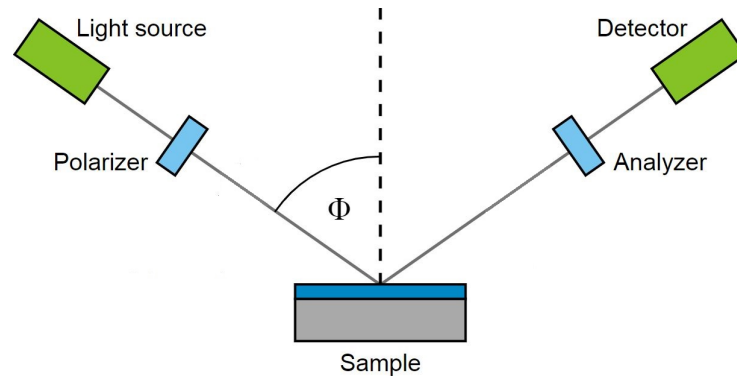


**Figure 2.4:** Schematic representation of an ellipsometry measurement [7].

An ellipsometer measures the change in polarisation which occurs to the incident light source upon contact with the measured sample. Figure 2.4 shows a linearly polarised light source incident on a sample. The specular component of the reflected light is analysed by the detector of an ellipsometer. The change in polarisation between the incident light source and the reflected light source can be measured in terms of amplitude ratio ( $\Psi$ ) and phase difference ( $\Delta$ ).

$$\tan(\Psi) \cdot e^{\Delta} = \rho = \frac{r_p}{r_s} \quad (2.2)$$

where  $\rho$  is the complex reflectance ratio,  $r_p$  is the reflectivity of p-polarized light and  $r_s$  is the reflectivity of s-polarized light. The measurements are carried out at angle closer to Brewster's angle as the ratio of  $r_p$  and  $r_s$  is maximum in that range [41].

The measured ( $\Psi$ ) and ( $\Delta$ ) depends on thickness and material of the sample. Thus, depending on the material, different optical models are used which mimics the optical properties of the sample material. The completeEASE software used in this work, follows an iterative approach which tweaks the oscillator functions, thickness and surface roughness of the sample to fit the measured curve to the chosen model [42]. Finally, the optical data from the model are extracted when the mean square error between the measured curve and model is less than 10.

### 2.3.3. Spectrophotometry

In this work, optical characterisation of individual thin film layers and the solar cell stack are carried out using spectrophotometry. Spectrophotometry measures the reflectance transmittance of a sample over a range of wavelength of incident light. An incident light source is converted into a monochromatic beam through an optical path containing mirrors and diffraction grating. The obtained monochromatic beam passes through the sample and then to an optical detector. The signal from the optical detector is compared with the reference signal. Depending on the positioning of the sample in the spectrophotometer, the transmittance or the reflectance of sample is expressed in relative terms to the reference beam.

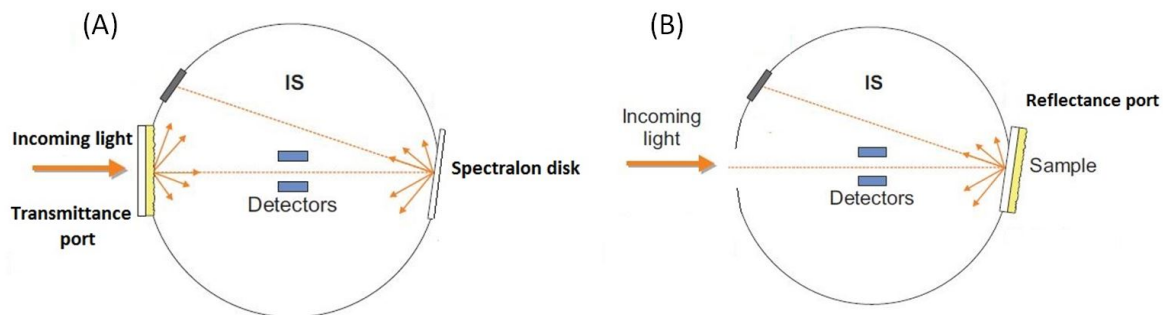


**Figure 2.5:** (A) Schematic representation of a transmittance measurement in an IS; and (B) Schematic representation of a reflectance measurement in an IS [8].

In this work, Lambda 950 by Perkin Elmer with an Integrating Sphere (IS) was used to carry out optical measurements. The IS sphere is coated with spectralon, which is highly reflective material and exhibits Lambertian behaviour [8]. As shown in the Figure 2.5, for transmittance measurements, the samples were placed in the transmittance port of the IS and the back portion of the IS was covered with a spectralon disk. Likewise, for reflectance measurements, the samples were placed in the reflectance port. Finally, the absorbance of the measured sample is calculated using the Equation 2.3.

$$A = 100 - (R + T) \quad (2.3)$$

## 2.4. Solar cell characterisation

### 2.4.1. Illuminated Current density-Voltage (J-V)

A standardised testing condition is required to enable comparison of solar cells manufactured at various companies and research laboratories [2]. These conditions are referred to as standard test conditions (STC), characterised by an irradiance of  $1000 \text{ W/m}^2$ , an A.M 1.5 spectrum and a cell temperature of  $25^\circ \text{ C}$  [2]. The solar simulator used in this work, uses a combination of xenon and halogen light bulbs to mimic the A.M 1.5 spectrum. The measuring stage is equipped with a cooling system to maintain the measurement temperature at a constant value of  $25^\circ \text{ C}$ .

In this work, all the J-V measurements were carried out using Wacom WXS-156-L2 solar simulator [43]. The J-V measurements gives a complete outlook about all the external solar cell parameters such as short-circuit current density ( $J_{SC}$ ), open-circuit voltage ( $V_{OC}$ ), fill factor (FF) and finally the efficiency  $\eta$  (%) of the solar cell. During the measurement, the solar cell is connected to a load and by varying the load applied to the cell, the current produced at different voltages are tabulated and plotted. Figure 2.6 represents a J-V curve of a-SiO<sub>x</sub>:H solar cell. The external parameters of a solar cell can be extracted from the J-V curve of a solar cell.

It is to be noted that, the spectrum of the solar simulator and A.M 1.5 spectrum does not have good coherence in near infrared region, and thus resulting in a slightly exaggerated value of ( $J_{SC}$ ). This issue is overcome by measuring the ( $J_{SC}$ ) with the help of external quantum efficiency (EQE) setup.

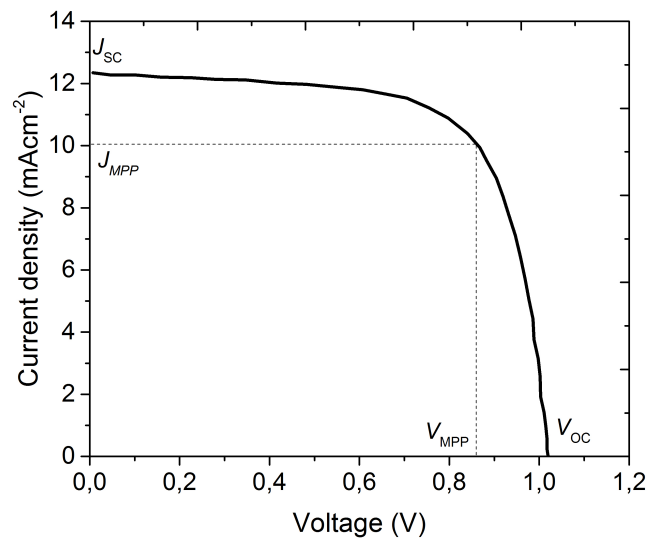


Figure 2.6: J-V curve of a-SiO<sub>x</sub>:H solar cell.

#### 2.4.2. External Quantum Efficiency (EQE)

External quantum efficiency is defined as the ratio of electron-hole pairs collected across a solar cell to that of number of photons incident on a solar cell [[33]]. The EQE of a solar cell at a particular wavelength ( $\lambda_R$ ) can be deduced by measuring the photogenerated current produced by the solar cell when illuminated by a monochromatic source with wavelength ( $\lambda_R$ ). Mathematically, EQE for a wavelength ( $\lambda_R$ ) can be obtained by Equation 2.4.

$$EQE(\lambda_R) = \frac{I_{ph}(\lambda_R)}{q \cdot \Phi_{ph}(\lambda_R)} \quad (2.4)$$

where  $\Phi_{ph}(\lambda_R)$  is the spectral photon flux which can be determined by using a calibrated photodiode and  $q$  is the elemental charge. As represented by Equation 2.5, the integral of  $I_{ph}(\lambda)$  over the entire spectral sensitive range of the solar cell gives a reliable measurement of the  $J_{SC}$  of the solar cell.

$$J_{SC} = \int_{\lambda_{min}}^{\lambda_{bandgap}} I_{ph}(\lambda) \cdot d\lambda \quad (2.5)$$

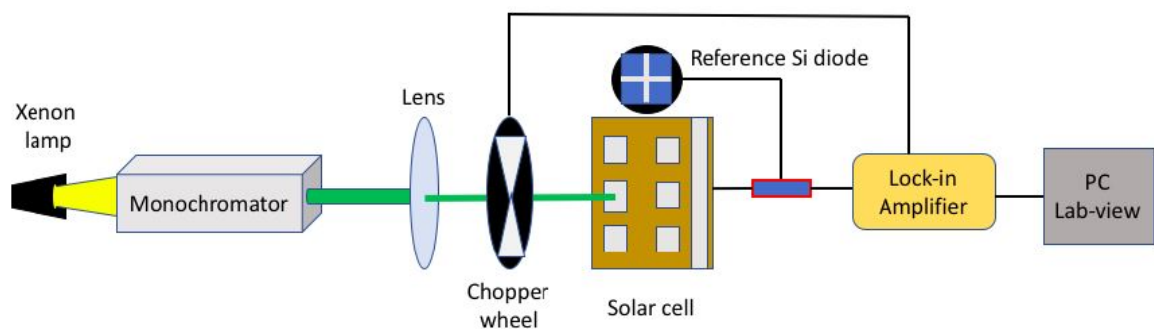
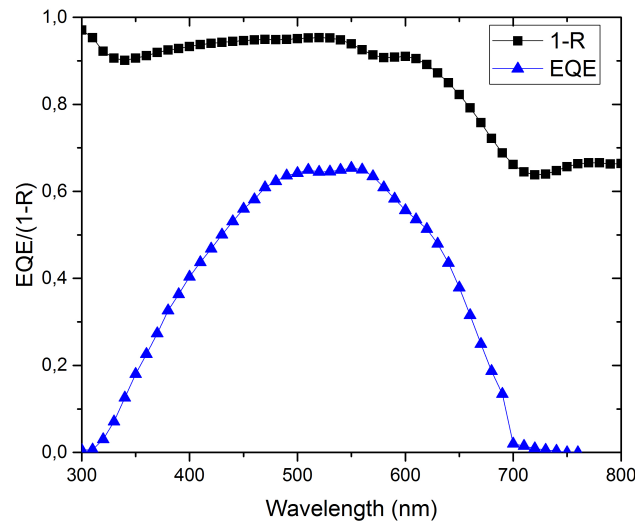


Figure 2.7: Schematic representation of EQE setup [9].

In this work, EQE measurements were carried out on an inbuilt setup represented by Figure 2.7. An incident beam of xenon lamp is converted into a monochromatic beam of light as explained in subsection 2.3.3. The resulting monochromatic light source illuminates the solar cell and the photocurrent generated is measured. In this work, EQE measurements are carried out in steps of 10 nm.

The EQE measurement gives a good idea about how the solar cell responds to the A.M 1.5 spectrum. By plotting  $(1-R)$  and EQE of a measured solar cell with respect to wavelength, a complete overview of optical response of a solar cell can be obtained. As shown in Figure 2.8, the area between the  $1-R$  and EQE curve gets absorbed by the solar cell stack and does not lead to generation of electron-hole pairs. The absorption in the solar cell, which doesn't contribute to generation of electron-hole pair is called as parasitic absorption [8]. Thus, Figure 2.8 gives a complete idea about reflection losses and parasitic losses which opens up a possibility for further optimisation in the solar cell.



**Figure 2.8:** EQE and 1-R plot of a-SiO<sub>x</sub>:H solar cell.

### 2.4.3. Calculation of Efficiency

In this work, solar cells were deposited on a Asahi UV or a AZO substrate of 10 cm × 2.5 cm dimensions. The substrate contains thirty solar cells with each solar cell having a dimension of 4 mm × 4 mm. The average value of  $V_{OC}$  and FF of the best performing 10 solar cells from Wacom measurement and  $J_{SC}$  value EQE measurements were considered for determination of efficiency of solar cells in each substrate. The  $J_{SC}$  of the solar cells were obtained from EQE measurements due to its better accuracy. All the electrical parameters mentioned in this report are displaced with suitable significant figures based on the precision of measurements.



## Theoretical efficiency determination of four terminal devices

The fabrication of a four terminal device (4TD) involves several processing steps. Hence, it is important to determine the efficiency of a 4TD configuration before its fabrication. In this chapter, a methodology to theoretically estimate the efficiency of a 4TD configuration is deduced with the help of a systematic analysis on the top and bottom cell of a 4TD.

In the first section, a brief introduction about the concept of a 4TD configuration is explained. The requirements of the top cell in a 4TD configurations are discussed in the second section. In the third section, the effect of top cell on the bottom cell in a 4TD configuration is analysed in detail and finally, the methodology to estimate the theoretical efficiency of a 4TD is discussed.

### 3.1. Four terminal devices - 4TD

Figure 3.1-(A) represents the losses incurred by a direct bandgap single-junction solar cell. As illustrated, high bandgap solar cells largely suffer from non-absorption losses and thermalisation losses dominates for low bandgap solar cells [2]. To reduce these losses, a high bandgap solar cell (top cell) can be optically coupled to a low bandgap solar cell (bottom cell), such that, high energetic photons in the A.M 1.5 spectrum get absorbed in the top cell and the non-absorbed photons are absorbed in the bottom cell. This explains the concept behind any tandem solar cells. Figure 3.1-(B) represents the typical structure of a 4TD. The top cell and bottom cell are optically interconnected and are separated by an insulator (optical coupler) to have electrical isolation.

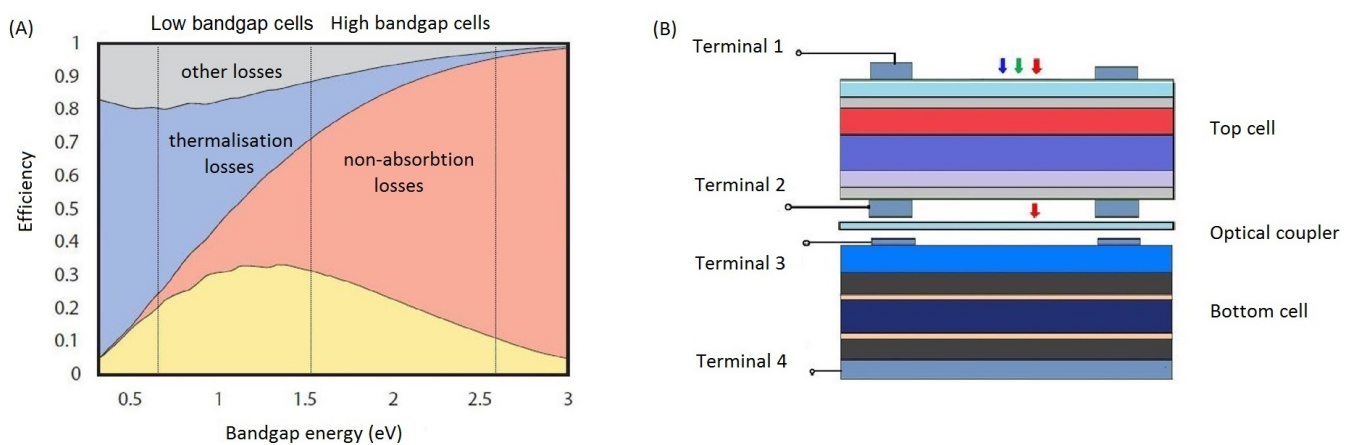


**Figure 3.1:** (A) the loss mechanism in Shockley-Queisser limit [2]; and (B) representation of a four terminal device.

### 3.1.1. Spectral Photovoltaic-output

Each solar cell responds to the AM 1.5 spectrum in a different manner based on its own external electrical and optical parameters. The external parameters which dictate a solar cell response to the solar spectrum are EQE,  $V_{OC}$  and FF of the solar cell. The spectral photovoltaic output ( $S - PV(\lambda)$ ) given by Equation 3.1 helps us to understand the solar cell performance for each wavelength of A.M 1.5 spectrum.

$$S - PV(\lambda) = V_{OC} \times FF \times e \times EQE(\lambda) \times \phi_{ph}(\lambda) \quad (3.1)$$

where  $\phi_{ph}(\lambda)$  represents the photon flux at a particular wavelength. The efficiency of the solar cell can be calculated from the spectral PV output using Equation 3.2.

$$\eta(\%) = \frac{\int_{\lambda_{280}}^{\lambda_{bandgap}} S - PV(\lambda) d(\lambda)}{\int_{\lambda_{280}}^{\lambda_{2500}} \phi_{A.M1.5}(\lambda) E_{ph}(\lambda) d(\lambda)} \times 100(\%) \quad (3.2)$$

A S-PV plot of a solar cell acts as a useful tool to analyse the spectral performance of a solar cell. Figure 3.2 (A) illustrates the S-PV of a single junction CIGS solar cell from Solliance. The electrical parameters of the solar cell are tabulated in Table 3.1. A comparison between S-PV of CIGS and the spectral irradiance of AM 1.5 spectrum is shown in Figure 3.2-(B). The plot clearly suggests that the solar cell does not utilise the A.M 1.5 spectrum efficiently due to thermalisation losses. The extent of thermalisation losses in the CIGS solar cell can be reduced with a help of 4TD configuration by placing a top cell with a higher spectral PV-output in the UV and visible spectral range.

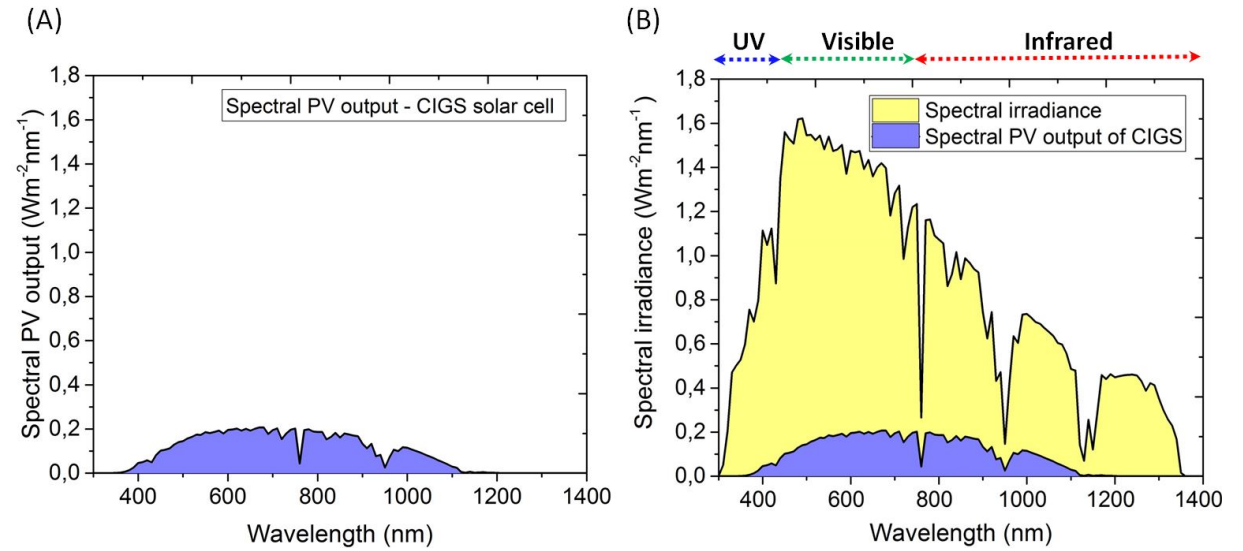


**Figure 3.2:** (A) spectral PV output of a CIGS solar cell; and (B) comparison of spectral PV output of a CIGS solar cell with spectral irradiance.

**Table 3.1:** Electrical parameters of CIGS solar cell from Solliance.

S.No	Cell	$J_{SC}$ (mA/cm <sup>2</sup> )	$V_{OC}$ (V)	Fill factor (FF)	$V_{OC} \times FF$ (V)	Efficiency (%)
1	CIGS	30.02	0.58	0.58	0.34	10.08

The CIGS solar cell mentioned in this section is considered as the bottom cell in a 4TD configuration to further

- analyse the requirements of a top cell.
- analyse the effect of the top cell on the bottom cell.
- evaluate the theoretical efficiency of such a device.

A simple schematics of the CIGS solar used in this work is shown in Figure 3.3.

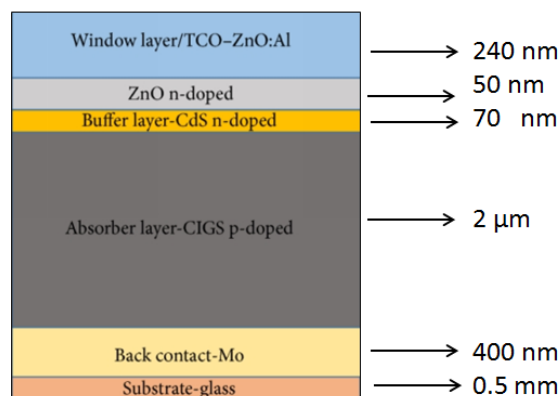


**Figure 3.3:** Schematic representation of CIGS solar cell indicating thickness of each layer in the device stack[10].

## 3.2. Figures of merit - Top cell

A solar cell needs to have certain figures of merit in order to be considered as a top cell in a 4TD configuration. In this section, these characteristic parameters are explained in detail.

### 3.2.1. High $V_{OC} \times FF$ product

The thermalisation losses in the bottom cell can be reduced by placing a top cell with a high  $V_{OC} \times FF$  product. The placement of a top cell results in collection of high energetic photons in the UV and visible part of spectrum at a higher  $V_{OC} \times FF$  product in comparison with the bottom cell, resulting in an increase in spectral PV-output. The extent of increase in S-PV output is decided by the difference in  $V_{OC} \times FF$  product of the top and bottom cell. The Table 3.2 represents electrical parameters of solar cells with high  $V_{OC} \times FF$  product.

**Table 3.2:** Electrical parameters of commonly used top cell in 4TD configuration.

S.No	Solar cell	$J_{SC}$ (mA/cm <sup>2</sup> )	$V_{OC}$ (V)	Fill factor (FF)	$V_{OC} \times FF$ (V)	Efficiency (%)
1	GaInP [31]	14.61	1.44	0.87	1.25	18.54
2	Perovskite [44]	20.90	1.03	0.74	0.76	16.01
3	a-SiO <sub>x</sub> :H (2.03 eV)	10.82	0.98	0.68	0.67	7.20
4	a-SiO <sub>x</sub> :H (1.96 eV)	13.08	0.96	0.69	0.66	8.69
5	a-Si:H	15.23	0.86	0.68	0.58	8.91

The research focus of this thesis is to utilise silicon based thin film solar cell as the top cell for 4TD configuration. Both a-SiO<sub>x</sub>:H and a-Si:H can be utilised as a top cell in 4TD configuration owing to their high  $V_{OC} \times FF$  product. Further analysis on other figures of merit of a top cell is carried out using a-SiO<sub>x</sub>:H due to its higher  $V_{OC} \times FF$  product than a-Si:H solar cell.

### 3.2.2. External Quantum Efficiency (EQE)

In Figure 3.2 (B), the thermalisation losses are more profound in the UV and visible part of the sun's spectrum, where a top cell with better EQE response would result in higher spectral PV-output than the bottom cell. Thus, the EQE of a solar cell is used as a parameter for figure of merit in determination of a suitable top cell in 4TD configuration.

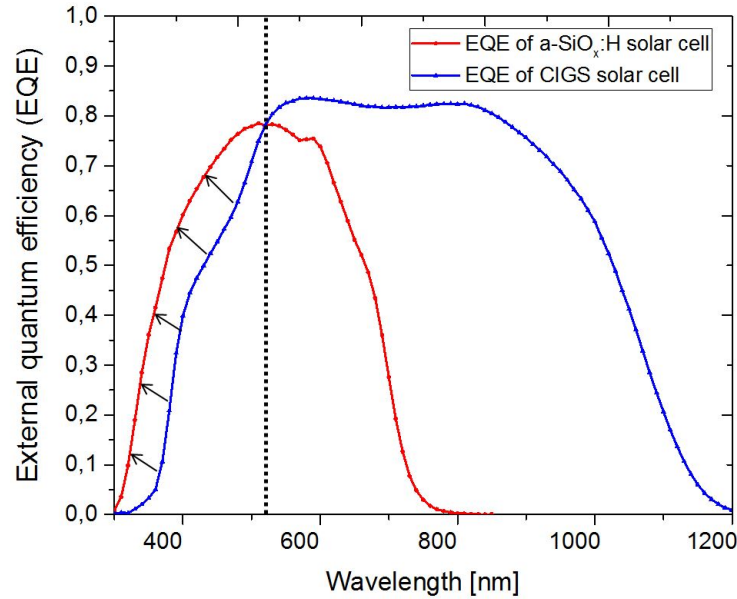


**Figure 3.4:** Comparison of EQE of a-SiO<sub>x</sub>:H with CIGS solar cell.

Figure 3.4 compares the EQE plot of CIGS and a-SiO<sub>x</sub>:H solar cell. As shown in the Figure 3.4, a-SiO<sub>x</sub>:H solar cell shows a better EQE response in the wavelength from 300 nm to 520 nm than the CIGS solar cell. This suggests that, by using the a-SiO<sub>x</sub>:H solar cell as a top cell, a larger fraction of high energetic photons can additionally be absorbed and collected at a higher  $V_{OC} \times FF$  product, resulting in lower thermalisation loss compared to the CIGS solar cell. The EQE of the CIGS solar cell shows a better response from 520 nm in comparison with the a-SiO<sub>x</sub>:H solar cell. However, the fraction of electron-hole pairs collected by the a-SiO<sub>x</sub>:H solar cell in this spectral range happens to be collected at a higher  $V_{OC} \times FF$  product compared to the CIGS solar cell, negating the effect of lower EQE response. Figure 3.5 (A) represents the spectral PV-output of a-SiO<sub>x</sub>:H solar cell in the spectral range of 300 nm to 720 nm. Owing to its higher  $V_{OC} \times FF$  product and its better EQE response in shorter wavelength ranges, the Spectral PV-output of a-SiO<sub>x</sub>:H solar cell is much higher compared to the CIGS solar cell. A comparison between the spectral PV-output of a-SiO<sub>x</sub>:H solar cell and CIGS solar cell is represented by Figure 3.5-(B). The pinkish red area represents the possible spectral gain of a 4TD configuration with an a-SiO<sub>x</sub>:H-CIGS configuration. This illustrates the advantage of using a-SiO<sub>x</sub> as the top cell in this 4TD configuration.

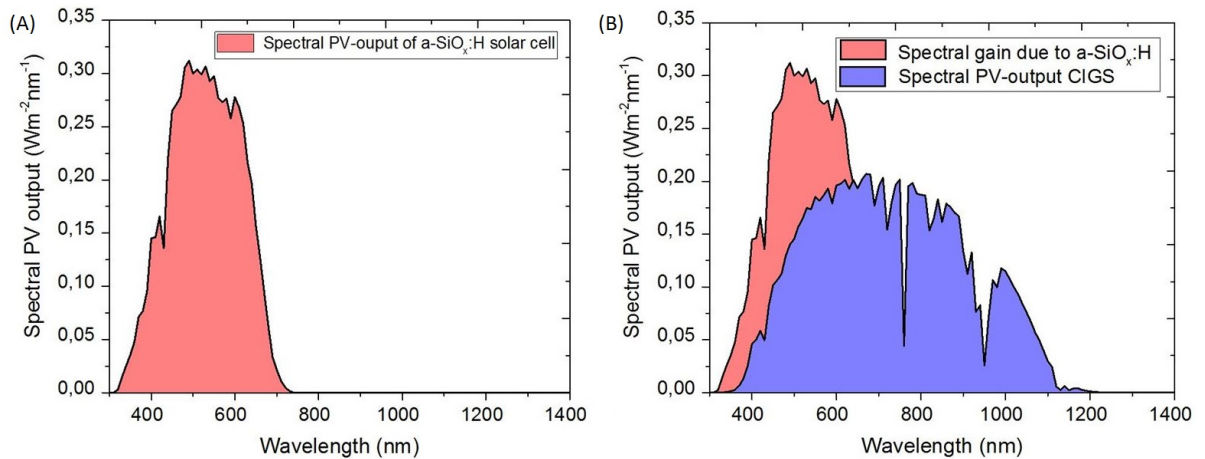


**Figure 3.5:** (A) spectral PV output of a-SiO<sub>x</sub>:H solar cell; and (B) spectral gain in the CIGS solar cell with a-SiO<sub>x</sub>:H solar cell as the top cell.

### 3.2.3. Transparency

In a 4TD configuration, a top cell is optically coupled with a bottom cell. The sun's spectra received by the bottom cell strongly depends on the transmission of the top cell. In simple terms, the top cell acts as optical filter which absorbs most of the sun's spectrum in UV and visible spectral range and transmits the non-absorbed spectrum to the bottom cell. The electrical parameters of any solar cell vary with the intensity of the incident light and as a result the electrical performance of the bottom cell depends on the transparency of the top cell. Thus, transparency is considered as a figure of merit in the choice of a top cell in 4TD configuration.

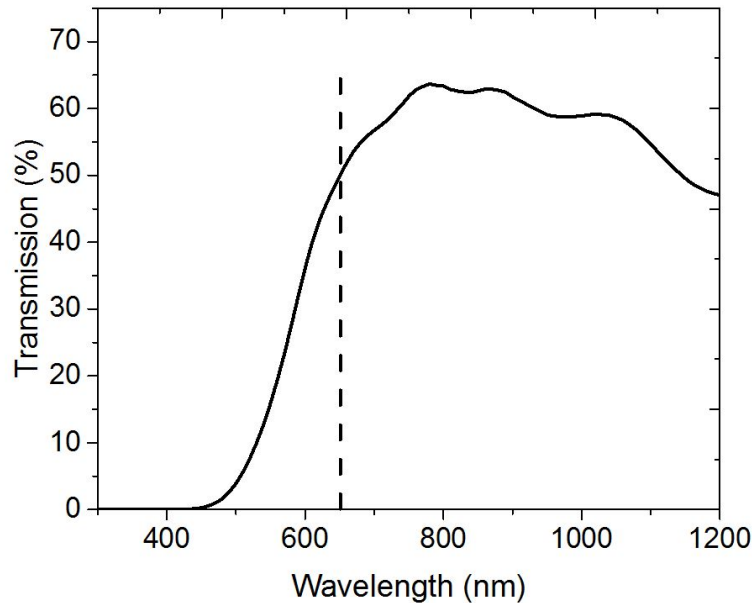


**Figure 3.6:** Transmission of the a-SiO<sub>x</sub>:H solar cell.

Figure 3.6 represents the transmission of the a-SiO<sub>x</sub>:H solar cell used in this work. An a-SiO<sub>x</sub>:H solar cell with (7-200-100) nm's of (p-i-n) layer thickness is used for the transmission measurement. Figure 3.5 (B) shows that, the spectral PV-output of CIGS solar cell exceeds the spectral PV-output of a-SiO<sub>x</sub>:H solar cell beyond a wavelength of 650 nm. The top cell needs to have a complete transmission of the incident light beyond this wavelength to achieve high efficiency 4TD. But in reality, parasitic absorption from the TCO's and other supporting layer limits the transparency of the top cell.

### 3.3. Effect of the top cell on the bottom cell

As mentioned in the previous section, the electrical parameters of the bottom cell is dependent on the transparency of the top cell. Figure 3.7 (A) represents the spectral irradiance incident on the top cell and Figure 3.7 (B) represents the attenuated spectrum incident on the bottom cell in presence of the top cell. The attenuated spectrum illustrates the effect of top cell's transparency on the spectrum incident on the bottom cell. The attenuated spectrum results in a change in the  $V_{OC} \times FF$  product of the bottom cell and also the current generation in the bottom cell. A methodology to determine these changes are explained in detail in the following section.

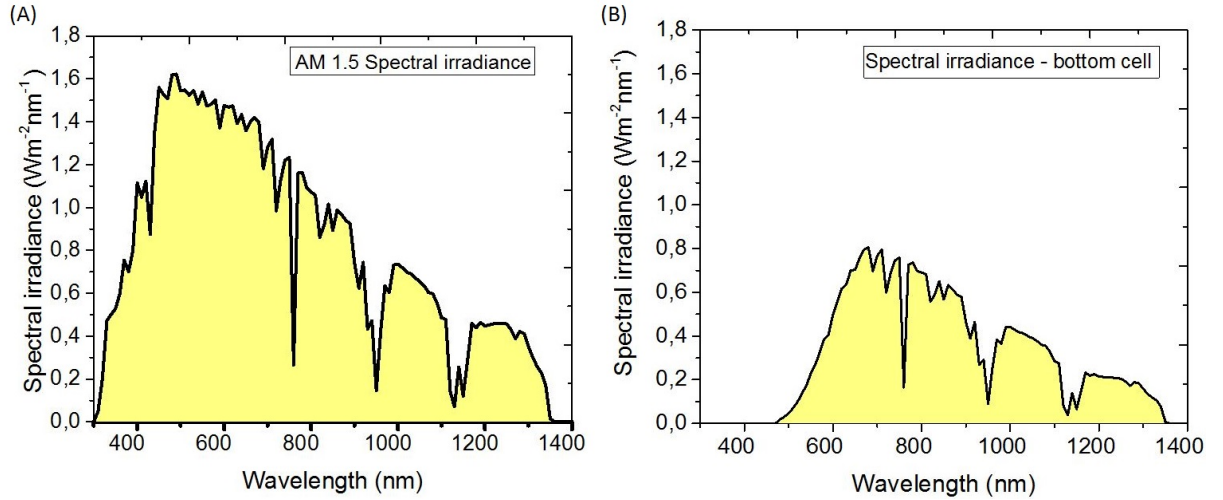


**Figure 3.7:** Spectral irradiance (A) on the top cell; and (B) on the bottom cell.

### 3.3.1. Variation of $J_{SC}$ of the bottom cell

The subsection 2.4.2 explains a way to calculate  $J_{SC}$  from the EQE plot of a solar cell. In this section, two different methods are adopted to determine the EQE of the bottom cell in a 4TD configuration and the obtained EQE curve is used to calculate the  $J_{SC}$  of the bottom cell represented as  $J_{SC,Bot}$ .

The a-SiO<sub>x</sub>:H solar cell mentioned in subsection 3.2.3 is placed on the top of the CIGS solar cell and the EQE of the CIGS solar cell is measured. The measured EQE is considered as a frame of reference to validate the different methodology used in this section.

#### Method 1

In this method, the transmittance of the top cell is multiplied with the EQE of the CIGS solar cell to estimate the EQE of the bottom cell in a 4TD configuration. This can be mathematically expressed by Equation 3.3.

$$EQE^*(\lambda) = T_{TOP}(\lambda) \times EQE_{CIGS}(\lambda) \quad (3.3)$$

where  $EQE^*$  is the calculated EQE of the bottom cell,  $T_{TOP}$  is the transmittance of the top cell and  $EQE_{CIGS}$  is the EQE of the CIGS solar cell. Figure 3.8 (A) compares the measured and calculated EQE of the CIGS solar cell using method 1. The method results in a slight mismatch in the wavelength range from 600 nm to 850 nm. The method assumes that the spectrum transmitted from the top cell is completely absorbed by the CIGS absorber layer in the bottom cell. In reality, the assumption does not hold well. The bottom cell reflects a part of the incident spectrum. The mismatch between the calculated and the measured EQE is due to the inability of the method to incorporate the reflection losses of the bottom cell. Moreover, a thin layer of air would be introduced between the top cell and bottom cell as they are not glued together. The difference in refractive indices of the top cell, air interface and bottom cell would result in reflection losses.

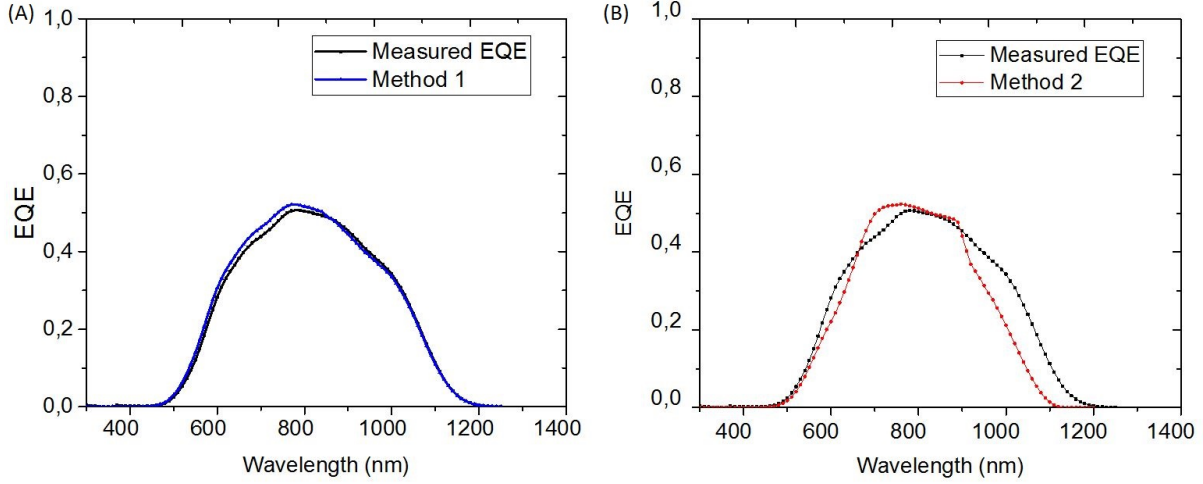


**Figure 3.8:** Comparison between the measured and calculated EQE - (A) method 1; and (B) method 2.

### Method 2

Method 2 simulates the EQE of the bottom solar cell using GenPro4 [45]. GenPro4 is a highly effective tool which simulates the optical behaviour of a solar cell in the A.M 1.5 spectrum. The input parameters for the simulations are the  $n$  and  $k$  values and thickness of all the layers in the optical stack of the 4TD configuration. Figure 3.8 (B) compares the measured and simulated EQE using method 2. The mismatch in the simulated and measured value is due to the inability to input the exact  $n$  and  $k$  data of the CIGS absorber layer leading to a mismatch in the result. As CIGS solar cells were not fabricated in house, the  $n$  and  $k$  measurements of the CIGS device stack was not carried out. Values from literature were adopted to simulate the CIGS device stack. In future projects, simulation using measured  $n$  and  $k$  values of these device stack can give a better coherence with the measured EQE of the bottom cell.

**Method 1** is adopted in this work to simulate the EQE of the bottom cell of a 4TD due to its simplistic approach and its adaptability to apply for any solar cell. The deviation between the measured and simulated EQE is negated with the incorporation of a correction factor while determining the  $J_{SC,Bot}$  as represented by Equation 3.4. A correction factor (CF) of 0.95 is considered which accounts for the deviation between the measured and simulated  $J_{SC,Bot}$ .

$$J_{SC,Bot} = CF \cdot q \int_{\lambda_{min}}^{\lambda_{bandgap}} EQE^*(\lambda) \cdot \Phi_{ph}(\lambda) \cdot d\lambda \quad (3.4)$$

### 3.3.2. $V_{OC} \times FF$ product of the bottom cell

The open circuit voltage of a solar cell shows a logarithmic dependence on incident irradiation [46]. The Equation 3.5 shows the variation of  $V_{OC}$  with incident irradiation.

$$V'_{OC} = V_{OC} + \frac{nkT}{q} \times \ln \frac{I'}{I} \quad (3.5)$$

where  $V'_{OC}$  represents the open circuit voltage at irradiation level  $I'$  and  $V_{OC}$  is the open circuit voltage at STC. In this work, the variation in  $V_{OC} \times FF$  product of the bottom cell is evaluated experimentally. The Wacom WXS-156-L2 solar simulator used for measuring the J-V characteristics of a solar cell is used to measure the  $V_{OC} \times FF$  product of the bottom cell at different illumination intensities. The illumination intensity on the solar cell is altered by placing an optical filter<sup>1</sup> on top of the solar cell.

The measured  $V_{OC} \times FF$  product of the bottom cell at different  $J_{SC}$  is fitted with a 3rd order polynomial function (Equation 3.6) as shown in Figure 3.9. The  $J_{SC}$  of the bottom cell evaluated by subsection 3.3.1 is substituted in Equation 3.6 to obtain  $V_{OC} \times FF$  product of the bottom cell.

<sup>1</sup>The optical filter's used in this experiments are neutral density filter from Thorlabs [47]. Neutral density filters are capable of reducing the transmission of light evenly across the AM 1.5 spectrum. The neutral density filters are characterised based on their optical density (OD). The filter's used in this work are tabulated in Appendix A.

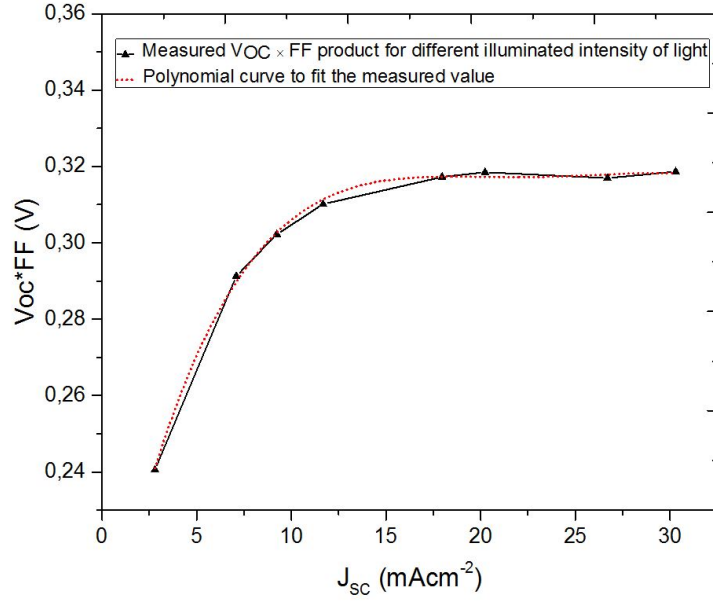


**Figure 3.9:**  $V_{OC} \times FF$  product of the CIGS solar cell at different illuminated light intensity.

$$(V_{OC} \times FF)_{Bot} = 0.1861 + 0.02349 \cdot J_{SC,Bot} - 0.00158 \cdot J_{SC,Bot}^2 + 1.59 \cdot 10^{-5} \cdot J_{SC,Bot}^3 \quad (3.6)$$

Finally, the efficiency of the bottom cell can be calculated by incorporating the change in  $V_{OC} \times FF$  and  $J_{SC}$  of the bottom cell due to the presence of top cell using Equation 3.7.

$$\eta_{Bot}(\%) = (V_{OC} \times FF)_{Bot} \cdot J_{SC,Bot} = (0.1861 + 0.02349 \cdot J_{SC,Bot} - 0.00158 \cdot J_{SC,Bot}^2 + 1.59 \cdot 10^{-5} \cdot J_{SC,Bot}^3) \cdot J_{SC,Bot} \quad (3.7)$$

### 3.4. Theoretical determination of efficiency of a 4TD

The efficiency of a 4TD ( $\eta_{4TD}$ ) can be expressed as the sum of the efficiency of the top cell ( $\eta_{Top}$ ) and the bottom cell ( $\eta_{Bot}$ ) in the device structure. The final efficiency of the device is expressed by Equation 3.8 and the gain in efficiency attained by a single junction solar cell using a 4TD configuration is given by Equation 3.9.

$$\eta_{4TD}(\%) = \eta_{Top}(\%) + \eta_{Bot}(\%) = (V_{OC} \times FF)_{Top} \cdot J_{SC_{Top}} + (V_{OC} \times FF)_{Bot} \cdot J_{SC_{Bot}} \quad (3.8)$$

$$\eta_{gain}(\%) = \eta_{4TD}(\%) - \eta_{SA}(\%) \quad (3.9)$$

where  $\eta_{SA}$  is the efficiency of the stand-alone single junction solar cell. Various bottom cell efficiency with a 4TD configurations were evaluated using a-SiO<sub>x</sub>:H solar cell as the top cell using the methodology explained in section 3.3. The results are tabulated in Table 3.3.

**Table 3.3:** Theoretical 4TD efficiency for different solar cells with a-SiO<sub>x</sub>:H solar cell as the top cell.

S.NO	Bottom cell	$\eta_{SA}(\%)$	$\eta_{Bot}(\%)$	$\eta_{Top}(\%)$	$\eta_{4TD}(\%)$	$\eta_{gain/loss}(\%)$
1	poly-Si	14.2	5.5	7.2	12.6	-1.6
2	CIGS	10.2	5.1	7.2	12.3	2.3
3	CIS	6.4	2.6	7.2	9.8	3.4

The Table 3.3 helps us to understand that the 4TD configuration with a-SiO<sub>x</sub>:H solar cell as the top cell results in an gain in efficiency for low efficiency bottom cell. Thus, the extent of increase in efficiency with a-SiO<sub>x</sub>:H solar cell as top cell depends on the efficiency of the bottom cell. To make the top cell more effective in a 4TD configuration, in the next chapter, an attempt to increase the  $V_{OC} \times FF$  of the top cell is carried out to increase the efficiency gain of the bottom cell.

### 3.5. Conclusion

Based on the results shown in this chapter, the following conclusions are derived:

- The three figures of merit which determine the effectiveness of a top cell in a 4TD configuration are external quantum efficiency (EQE),  $V_{OC} \times FF$  product and their transmission.
- The placement of a top cell affects both EQE and  $V_{OC} \times FF$  of the bottom cell. The transmission of the top cell determines the performance of the bottom cell. In this chapter, the EQE of the bottom cell was evaluated using two different methodologies. Method 1 is utilised in further part of this work to simulate the EQE of the bottom cell due to its simplistic approach and its adaptability to apply for any solar cell. The variation of  $V_{OC} \times FF$  the bottom cell at different irradiance level is determined experimentally. Finally, the efficiency of the bottom cell in a 4TD configuration is determined by combining the effect of top cell on both EQE and  $V_{OC} \times FF$  of the bottom cell.
- The theoretical 4TD efficiency for different bottom cells using a-SiO<sub>x</sub>:H top cell suggests that the gain in efficiency depends on the performance of the bottom cell. A relatively low performing bottom cells shows higher efficiency gain and for a poly-Si solar cell with a stand-alone efficiency of 14.2% a loss of 1.6% is obtained in a 4TD configuration. This suggest the need for optimisation of top cell to make it more robust in 4TD configuration.



# 4

## Fabrication of a-SiO<sub>x</sub>:H solar cell with high $V_{OC} \times FF$ product

As seen in the previous chapter, a top cell with high  $V_{OC} \times FF$  product is required to enhance the spectral gain in a four terminal device (4TD) configuration. Previously, in the PVMD group Kim et al.. [34] fabricated an a-SiO<sub>x</sub>:H solar cell with high  $V_{OC} \times FF$  product of 0.76 on ZnO:Al substrate. In this chapter, the growth rate of [34] is adopted to try and replicate the fabrication of a-SiO<sub>x</sub>:H solar cell with high  $V_{OC} \times FF$  product in an Asahi UV substrate. In the first section, a brief outlook on the effect of growth rate on thin film material property is discussed. The p-layer and n-layer are optimised according to the growth rate of [34] and their effect on the solar cell characteristics are discussed in the subsequent sections.

### 4.1. Thin film material properties as a function of growth rate

Material properties of a thin hydrogenated amorphous silicon (a-Si:H) based layers deposited using a plasma enhanced chemical vapour deposition system (PECVD) depend on various parameters as represented in Figure 4.1. The arrow points towards the direction of dependency. At specific substrate conditions (substrate temperature, substrate-electrode distance, process pressure etc.), the material properties of the thin film are dictated by the reactions at the growth surface [48]. The surface reactions facilitates the thin film growth and also consequently defines the surface composition of the deposited material. At a specific temperature, the surface reactions are governed by the plasma composition [49], which can be altered using the plasma settings (radio-frequency (RF) power, deposition pressure, gas composition and total gas flow) of a PECVD system.

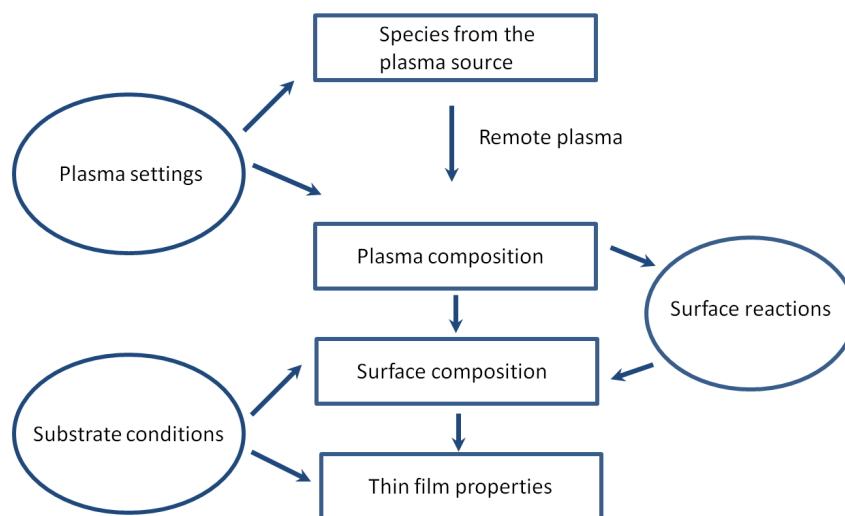


**Figure 4.1:** Simplistic representation of the deposition process of thin films by a plasma source [11].

To summarise, the particle flux and its chemical composition at a particular temperature decides the surface reactions on the substrate, defines the growth rate and dictates the material properties of a thin film material. The growth rate of the thin film material is considered as a measure for the plasma properties and in this work, the growth rate of layers fabricated by Kim et al. [34] is considered as a frame of reference for the fabrication of a-SiO<sub>x</sub>:H solar cell with high  $V_{OC} \times FF$  product. In this chapter, the growth rate, electrical and optical properties obtained from [34] is referred as Do Yun Kim (DYK).

## 4.2. Optimisation of a-SiO<sub>x</sub>:H solar cell based on growth rate of DYK

Table 4.1 compares the growth rate of thin film layer(s) at the beginning of experimental work with the growth rate of DYK. The p-layer (p-a-SiO<sub>x</sub>:H) and n-layer (n-nc-SiO<sub>x</sub>:H) shows a substantial deviation from the growth rate of DYK's depositions. The growth rate of these layers needs to be matched with that of DYK's (optimised) for fabrication of a-SiO<sub>x</sub>:H solar cell with high  $V_{OC} \times FF$  product.

**Table 4.1:** Growth rate of layer's in a-SiO<sub>x</sub>:H solar cell stack.

Layer	RF power (W)	Growth rate (nm/min)	Growth rate - DYK (nm/min)	$\Delta$ (%)
p-nc-Si	50	9.3	9	3.34
p-a-SiO <sub>x</sub> :H	5	12.1	6	101.6
i-a-SiO <sub>x</sub> :H	6	3.4	3.3	3.03
i-a-SiO <sub>x</sub> :H	3	4.8	4.5	6.67
n-nc-Si:H	10	1	1	0.0
n-nc-SiO <sub>x</sub> :H	10	1.2	1.7	-31.76

### 4.2.1. Reference a-SiO<sub>x</sub>:H solar cell

A solar cell with the deposition parameters mentioned in Table 4.2 is used as a reference cell in this analysis. The solar cell is fabricated in a p-i-n structure. Guijt [12] used the same device stack as that of the reference cell, but using the growth rate of DYK's cell mentioned in Table 4.1. The solar cell fabricated by Erwin Guijt is referred as Cell A. A comparison of the electrical parameters of the reference solar cell and Cell A is shown in Table 4.3. The difference in  $V_{OC}$  and  $J_{SC}$  between two cells are significant suggesting that the device stack used in this work needs optimisation. Figure 4.2 compares the EQE of the reference solar cell with Cell A. Compared to Cell A, a lower EQE response of the reference solar cell in the wavelength range 450 nm to 720 nm results in a lower  $J_{SC}$ .

**Table 4.2:** Deposition parameters of the reference a-SiO<sub>x</sub>:H solar cell [9].

Layer	Thickness (nm)	SiH <sub>4</sub> (sccm)	CO <sub>2</sub> (sccm)	H <sub>2</sub> (sccm)	B <sub>2</sub> H <sub>6</sub> (sccm)	PH <sub>3</sub> (sccm)	RF power (W)	Pressure (mbar)	Temperature (° C)
p-nc-Si	5	1.5	-	200	30	-	50	2.5	300
p-a-SiO <sub>x</sub> :H	7	20	45	20	2	-	5	0.7	300
i-a-SiO <sub>x</sub> :H	10	2.5	2.5	200	-	-	6	2.6	200
i-a-SiO <sub>x</sub> :H	200	8	2	200	-	-	3	2	200
n-nc-Si:H	5	1	-	100	-	1.2	10	1.5	300
n-nc-SiO <sub>x</sub> :H	100	1	2	100	-	1.2	10	1.5	300

**Table 4.3:** Comparison of electrical parameters of the reference solar cell with cell A [12].

Solar cell	$J_{SC}$ (mA/cm <sup>2</sup> )	$V_{OC}$ (V)	Fill factor (FF)	$V_{OC} \times FF$ (V)	Efficiency (%)
Reference solar cell	10.84	0.98	0.68	0.67	7.22
Cell A	12.67	1.01	0.67	0.68	8.61

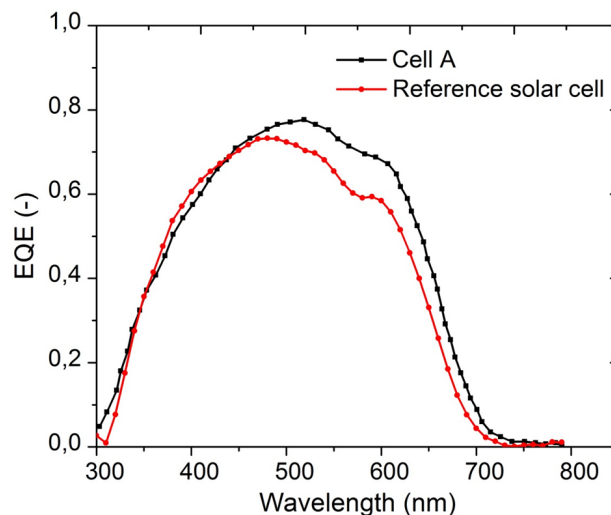


Figure 4.2: Comparison of EQE of Reference solar cell and Cell A.

The variation in  $V_{OC}$  and FF of the reference solar cell to that of Cell A could possibly be due to the mismatch in the growth rate(s). In the subsequent sections, an approach to match the growth rate of reference cell and Cell A is explained.

#### 4.2.2. Optimisation of p-layer

Table 4.1 suggests that the growth rate of p-layer is much higher in comparison to DYK's growth rate. RF power supplied to the PECVD processing chamber defines the flux of the reactive species in the plasma. A higher growth rate in the current scenario suggests that a higher flux of reactive species participates in the thin film growth. Thus, the growth rate of thin film can be reduced by minimising the flux of the reactive species by decreasing the RF power while maintaining other substrate and process parameters at a constant value.

In this section, the RF power supplied to the processing chamber is reduced in steps of 1 W and the optical and electrical properties of the fabricated thin film are compared with that of DYK. The comparison acts as a tool to analyse the optimisation procedure and finally gives an insight on the effect of growth rate on the material properties of the thin film. The effect of RF power on the growth rate of p-a-SiO<sub>x</sub>:H is shown in Figure 4.3.

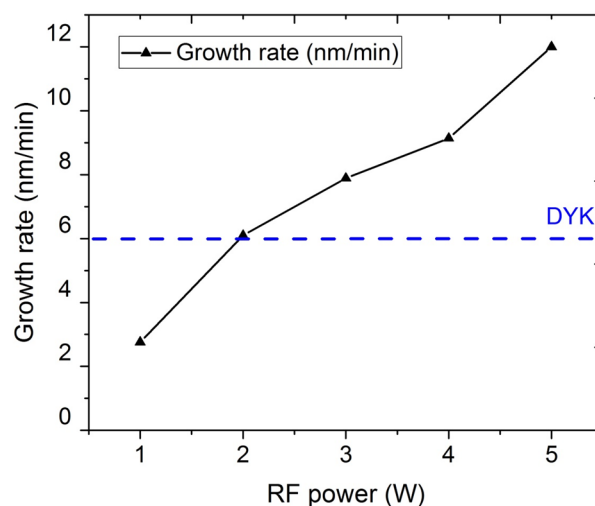
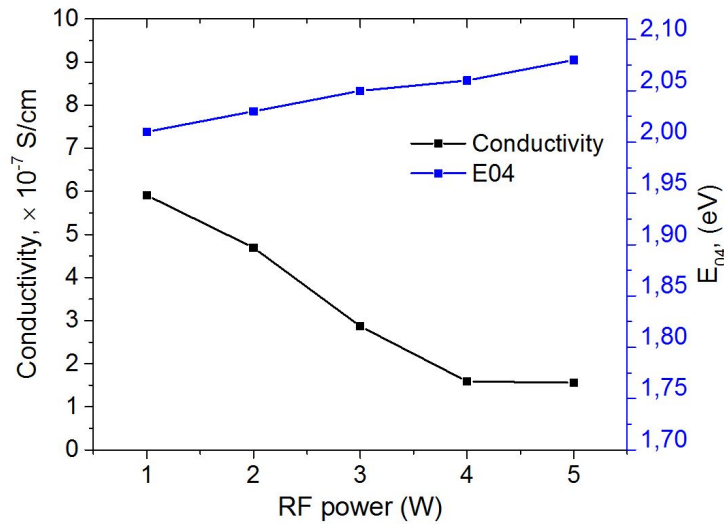


Figure 4.3: Effect of RF power on the growth rate of p-a-SiO<sub>x</sub>:H layer (the dotted line represents the growth rate of DYK).

The growth rate increases with increasing, implying a higher flux of reactive species in the plasma partici-

pating in the growth surface. The obtained thin film is compared with DYK's layer in terms of optical bandgap ( $E_{04}$ ), dark conductivity ( $\sigma_D$ ) and activation energy ( $E_a$ ). The compared results are tabulated in Appendix B.

Figure 4.4 represents the effect of RF power on the optical bandgap and conductivity of p-a-SiO<sub>x</sub>:H layer. The optical bandgap increases with increase in RF power, whereas, conductivity decreases with increase in RF power.



**Figure 4.4:** Effect of RF power on  $E_{04}$  and  $\sigma(D)$  of p-a-SiO<sub>x</sub>:H layer.

The variations in optical bandgap and conductivity can be explained with the help of microstructure of p-a-SiO<sub>x</sub>:H layer. The p-a-SiO<sub>x</sub>:H layer has a heterogeneous microstructure consisting of a silicon rich phase which is confined by an oxygen rich phase [50]. An increase in oxygen content in the p-a-SiO<sub>x</sub>:H layer results in an increase in its optical bandgap, whereas, the silicon rich phase is mainly responsible for its electrical conductivity.

In p-a-SiO<sub>x</sub>:H microstructure, SiH<sub>4</sub> and CO<sub>2</sub> molecules are responsible for incorporation of silicon and oxygen respectively. The dissociation rate of SiH<sub>4</sub> molecule is greater than CO<sub>2</sub> [51]. As we have reduced the RF power to match the optimum growth rate, it is possible to advocate that at a lower power the relative influx of silicon based radical would be higher than the oxygen based radical. The trend in optical bandgap and conductivity in p-a-SiO<sub>x</sub>:H layer due to the reduction of RF power could possibly be due to a lower fraction of oxygen rich phase and relatively higher fraction of silicon rich phase in the thin film material.

The optical and electrical parameters of the p-layer at the optimised growth rate do not match with the values obtained by DYK as displayed in Table B.1. However, at 2W RF power, when the growth rate matches with DYK, we see a low activation energy and high conductivity compared to layer deposited at 5W. This drives us forward to further investigate on p-layer deposited at 2W RF power by incorporating it in the solar cell stack.

#### Optimised p-layer in a-SiO<sub>x</sub>:H solar cell stack

The electrical parameters of the solar cell with the new p-layer (2 W) are tabulated in Table 4.4. As seen from the table, the change of p-layer results in an increase in  $V_{OC}$  of 20 mV.

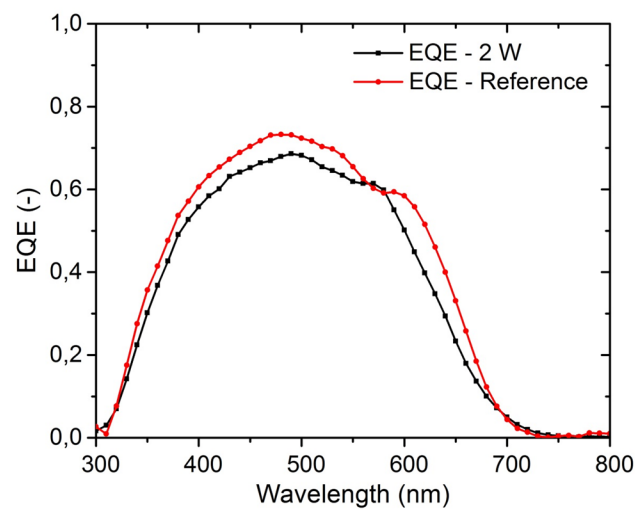
The increase in  $V_{OC}$  can possibly be attributed to one or several of the following factors.

- The reduction in the activation energy of the p-layer deposited at 2 W is 40 meV smaller than for the layer deposited at 5 W. This can possibly result in better band alignment with i-layer and result in increase in  $V_{OC}$ .
- The increase in conductivity could result in better charge separation at the p-i interface resulting in lower recombination of charge carriers.
- Lower recombination at p-i interface due to reduced oxygen concentration in the new p-layer.

**Table 4.4:** External parameters of a-SiO<sub>x</sub>:H solar cell with optimised p-layer.

Solar cell	Layer thickness (p-i-n)	$J_{SC}$ (mA/cm <sup>2</sup> )	$V_{OC}$ (V)	Fill factor (FF)	$V_{OC} \times FF$	Efficiency (%)
Reference solar cell	07-200-100	10.84	0.98	0.68	0.67	7.22
2 W - 7 nm	07-200-100	9.88	1.0	0.67	0.67	6.62

The  $J_{SC}$  shows a substantial decrease in comparison to the reference solar cell. The decrease in  $J_{SC}$  can be explained with the EQE plot in Figure 4.5. From Table B.1, We can infer that the optical bandgap of the new p layer is 0.05 eV lower than the p-layer used for the reference solar cell. The lower bandgap p-layer results in high parasitic absorption which leads to a smaller  $J_{SC}$  in the solar cell.

**Figure 4.5:** EQE comparison of the reference solar cell with optimised p-layer.

As remarked by Kim et al. [34], a slightly thicker p-layer results in a gain in  $V_{OC} \times FF$  product owing to better junction characteristics. Solar cells with 10 nm thick p-layer have been fabricated to study the effect of p-layer thickness on the solar cell characteristics and its external parameters are tabulated in Table 4.5.

**Table 4.5:** External parameters of solar cell with variation of p-layer thickness.

Solar cell	Layer thickness (p-i-n)	$J_{SC}$ (mA/cm <sup>2</sup> )	$V_{OC}$ (V)	Fill factor (FF)	$V_{OC} \times FF$	Efficiency (%)
2 W - 7 nm	07-200-100	9.88	1.00	0.67	0.67	6.62
2 W - 10 nm	10-200-100	9.54	1.01	0.68	0.69	6.55

A thicker p-layer increases the  $V_{OC} \times FF$  product of the solar cell from 0.67 to 0.69. The increase in  $V_{OC} \times FF$  product comes at the expense of  $J_{SC}$ . The decrease in  $J_{SC}$  can be explained with the help of EQE plots of solar cell with 7 nm and 10 nm thick p-layer is shown in Figure 4.6. The plot suggests that the solar cell with 10 nm shows a lower EQE response in shorter wavelength. This can be attributed to the increase in parasitic absorption due to a thicker p-layer.

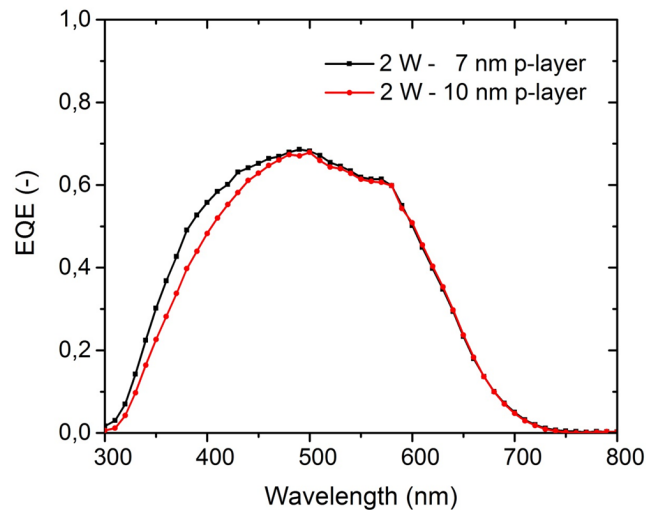


**Figure 4.6:** EQE response of solar cell with 7 nm and 10 nm thick p-layer.

Owing to its high  $V_{OC} \times FF$  product, the layer with 10 nm thick p-layer deposited at 2 W of RF power is considered as the new optimum and used for the fabrication of a-SiO<sub>x</sub>:H solar cell in the subsequent sections.

#### 4.2.3. Optimisation of n-layer

The n-nc-SiO<sub>x</sub>:H layer can be considered as a heterogeneous material consisting of a crystalline phase composed of crystalline silicon (c-Si) grains embedded in an amorphous phase of a-SiO<sub>x</sub>:H [52]. The crystalline silicon grains in the heterogeneous material are responsible for the lateral conductivity in the material [53] and the oxygen incorporation in the amorphous phase is responsible for increase in the optical bandgap of the material [52]. Further, the oxygen incorporation results in lowering the refractive index ( $n$ ) of n-nc-SiO<sub>x</sub>:H material [52].

Table B.2 compares the optical bandgap and conductivity of the deposited n layers for different RF power with that of DYK. As shown in Figure 4.7 and Figure 4.8, the growth rate and optical bandgap increases with the increase in RF power.

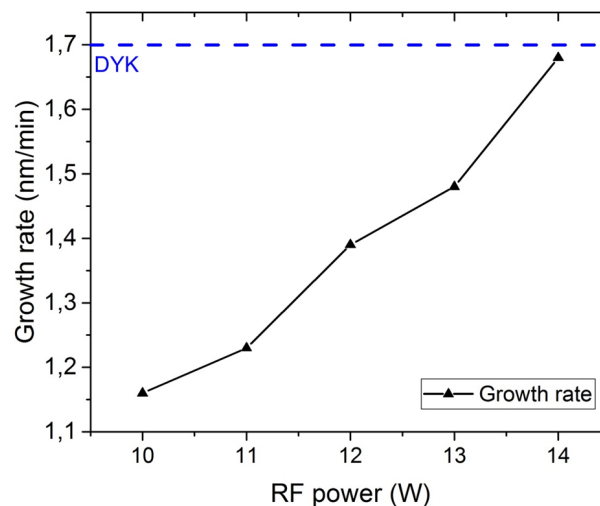


**Figure 4.7:** Effect of RF power on the growth rate of n-nc-SiO<sub>x</sub>:H layer (the dotted line represents the growth rate of DYK).

The increase in RF power likely results in more dissociation of SiH<sub>4</sub> and CO<sub>2</sub> and thus increases the influx of reactive species from the plasma to the growth surface resulting in an increase in growth rate. The incorporation of oxygen phase in a material's microstructure increases with the RF power [54]. The trend in

the increase of the optical bandgap could be advocated to a possible additional incorporation of silicon oxide phase in the material's microstructure. The decreasing trend in the conductivity could possibly be due to an increase in amorphous phase in the material. The amorphous phase leads to a non-uniformity in the crystal growth leading to a poor lateral conductivity [55].

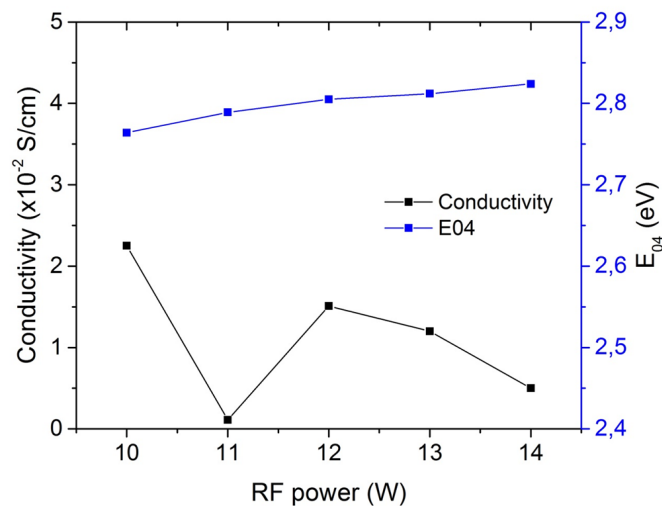


**Figure 4.8:** Effect of RF power on  $E_{04}$  and  $\sigma(D)$  of n-nc-SiO<sub>x</sub>:H layer.

The n-nc-SiO<sub>x</sub>:H layer at 14 W RF power has a higher optical bandgap and lower activation energy compared to the reference layer at 10 W. The layer is chosen and further investigated by applying it as the n-layer in the solar cell stack.

The electrical parameters of the solar cell with 10 W and 14 W n-layer are tabulated in Table 4.6. The solar cell fabricated with the new n-layer shows a significant increase in the  $J_{SC}$  and thus increases the overall efficiency of the solar cell. The increase in  $J_{SC}$  can be explained with the help of comparing the EQE and  $1 - R$  plot of the solar cells. The plot in Figure 4.9 compares the EQE of the solar cell with 14 W n-layer shows a significant increase in red response and also a decrease in  $1 - R$  suggesting a lower parasitic absorption in the solar cell.

**Table 4.6:** External parameters of solar cell with optimised n-layer.

Solar cell	Layer thickness (p-i-n)	$J_{SC}$ (mA/cm <sup>2</sup> )	$V_{OC}$ (V)	Fill factor (FF)	$V_{OC} \times FF$	Efficiency (%)
10 W - n layer	10-200-100	9.54	1.010	0.68	0.69	6.55
14 W - n layer	10-200-100	10.94	1.004	0.67	0.67	7.36

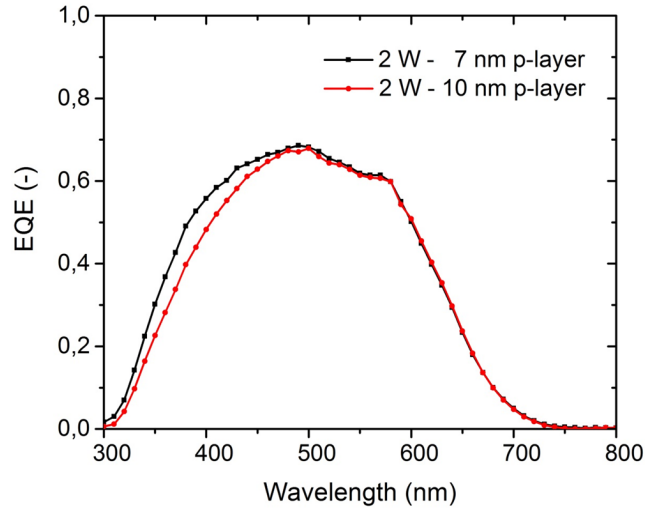


**Figure 4.9:** EQE and 1-R comparison of cell B with solar cell with 14 W n-layer.

The refractive index of intrinsic layer varies from 4.1 to 3.8 in a wavelength range of 400 to 600 nm. A higher difference in refractive index between i and n layer would result in a larger reflection at the i/n interface [56]. The refractive index ( $n$ ) as a function of wavelength for n-nc-SiO<sub>x</sub>:H layers at 10 W and 14 W is shown in the Figure 4.10. The figure shows that the  $n$  at 14 W of power is lower than at 10 W throughout the measured wavelength range. This results in a higher reflection at i/n interface resulting in a higher red response of the solar cell. The lower refractive index of 14 W layer, could also minimise the plasmonic absorption at n/Ag interface of the solar cell resulting in a gain in  $J_{SC}$  [57].

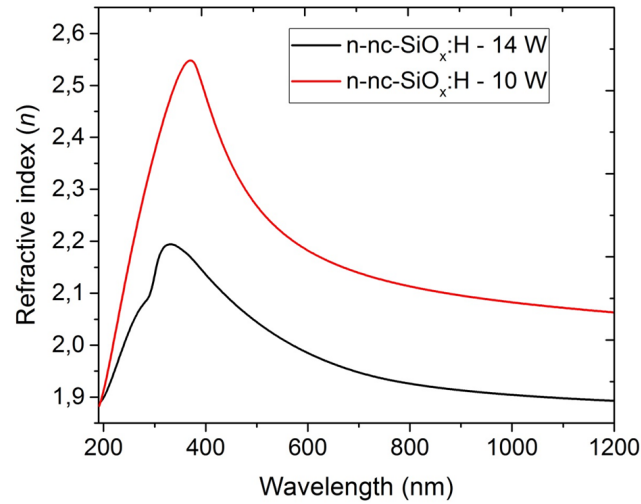


**Figure 4.10:** Refractive index ( $n$ ) as a function of wavelength for n-nc-SiO<sub>x</sub>:H at 10 W and 14 W.

#### 4.2.4. Fabrication of solar cell with high $V_{OC} \times FF$ product

$V_{OC}$  and FF are external electrical parameters which are based on the junction quality of a solar cell. The factors such as band-alignment, magnitude of the internal electric field and interface defects play an important role in defining  $V_{OC}$  and FF. In this section, the i-layer thickness of the solar cell is reduced while keeping the p layer and n layer at its optimum thickness of 10 nm and 100 nm respectively. The electrical characteristics of the solar cell fabricated with different i-layer thickness are tabulated in Table 4.7.

**Table 4.7:** External parameters of solar cell with varying i-layer thickness.

Solar cell	Layer thickness (p-i-n)	$J_{SC}$ (mA/cm <sup>2</sup> )	$V_{OC}$ (V)	Fill factor (FF)	$V_{OC} \times FF$	Efficiency (%)
130 nm	10-130-100	9.52	1.012	0.71	0.72	6.86
150 nm	10-150-100	9.76	1.007	0.70	0.70	6.95
175 nm	10-175-100	10.25	1.004	0.69	0.69	7.10
200 nm	10-200-100	10.64	1.002	0.68	0.68	7.34

Figure 4.11 shows the trend of all the external parameters with the varying i layer thickness. The  $V_{OC}$  and FF decreases with increase in i-layer thickness. The high  $V_{OC}$  in a thin i-layer can be attributed to the following reasoning. As the i-layer thickness reduces, the defect density in the absorber layer decreases. Leading to a decrease in recombination centers and a higher drift velocity (owing to increase in electric field due to a thinner i-layer) the recombination probability of the charge carrier decreases resulting in an increase in  $V_{OC}$ .

By reducing the thickness of i-layer, a  $V_{OC} \times FF$  product of 0.72 is obtained at 130 nm. Solar cells fabricated with i-layer thickness less than 130 nm were prone to shunting due to very thin i-layers.

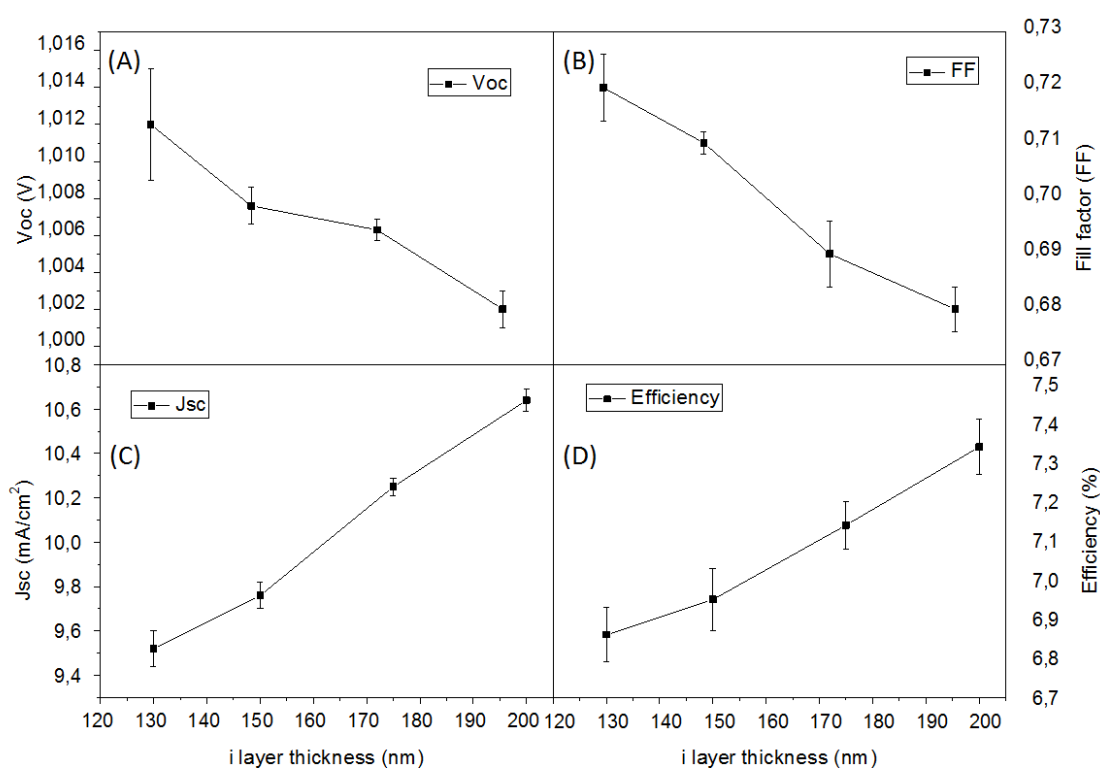


**Figure 4.11:** External parameters of a-SiO<sub>x</sub>:H with varying i-layer thickness (A) open circuit voltage; and (B) fill factor; and (C) short circuit current; and (D) efficiency.

Figure 4.11 (C) and (D) shows the increase in  $J_{SC}$  and efficiency with increase in i-layer thickness. A thinner layer absorbs less than a thicker layer, resulting in lower  $J_{SC}$ . The drop in efficiency with adoption of thinner i layer is due to fact that the gain in  $V_{OC} \times FF$  is not as significant compared to loss in  $J_{SC}$ .

#### 4.2.5. Comparison with Cell A

Subsection 4.2.2 and 4.2.3 give a conclusive evidence of the effect of p-layer and n-layer on the performance of the a-SiO<sub>x</sub>:H solar cell. In this section, a-SiO<sub>x</sub>:H solar cell with the optimised p and n-layer(s) with p-i-n thickness (7-200-100) are compared with Cell A to give an insight on the scopes of improvement and the provide a path way for subsequent future work. The solar cell is named as Cell D for descriptive purpose.

The electrical parameters of Cell A and Cell D are tabulated in Table 4.8. It is very evident that the efficiency of the Cell D is limited due to its  $J_{SC}$ . Figure 4.12 compares the EQE of Cell D with Cell A. The current

solar cell has a reduced EQE response throughout its spectral range. The reduced response is mainly due to the parasitic absorption of the current p-layer due to its lower optical bandgap (2.03 eV) in comparison to the p-layer used in Cell A (2.17 eV).

**Table 4.8:** External parameters of solar cell with optimised p and n-layer.

Solar cell	Layer thickness (p-i-n)	$J_{SC}$ (mA/cm <sup>2</sup> )	$V_{OC}$ (V)	Fill factor (FF)	$V_{OC} \times FF$	Efficiency (%)
Cell A	07-200-100	12.67	1.01	0.67	0.68	8.61
Cell D	07-200-100	11.62	1.00	0.67	0.67	7.78

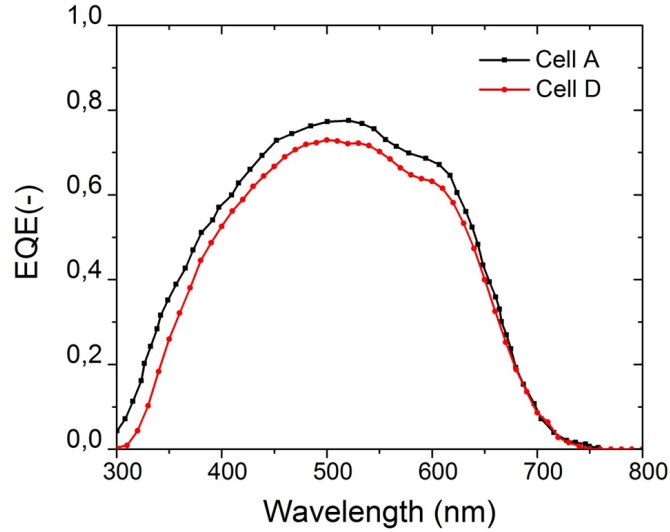


**Figure 4.12:** Comparison of the Cell D with Cell A.

The parasitic absorption in the solar cell can be reduced by adopting a p-nc-SiO<sub>x</sub>:H as a p-type layer, owing to its higher bandgap and better conductivity in comparison to p-a-SiO<sub>x</sub>:H layer [58].

### 4.3. Conclusion

Based on the results shown in this chapter we come to the following conclusions:

- Matching the deposition rate of the p-layer with the findings of Kim et al. [34] resulted in an increase in  $V_{OC}$  from 0.98 to 1 V. The increase in the  $V_{OC}$  can be attributed to the decrease in activation energy of the doped p-layer.
- Matching the deposition rate of n-layer resulted in an increase in  $J_{SC}$  from 9.54 mAcm<sup>-2</sup> to 10.94 mA cm<sup>-2</sup>. The increase can be attributed to the higher difference in refractive index between i-layer and the optimised n-layer. As a result, a higher reflection at the i/n interface led to an increase in short-circuit current density.
- As shown from the comparison of Cell A and Cell D, the current solar cell suffers from a high parasitic absorption in the p-layer and limits the  $J_{SC}$  in the current device. Fabrication of p-nc-SiO<sub>x</sub>:H can be considered to minimise the parasitic losses.
- Finally, through optimisation process a high  $V_{OC} \times FF$  product of 0.72 is obtained.

# 5

## Analysis of various a-SiO<sub>x</sub>:H solar cell stacks

In the previous chapter, top cells with a high  $V_{OC} \times FF$  product were fabricated. Now, it is important to analyse the bottlenecks of the current top cell and explore possible solutions. In this chapter, other figures of merit of a top cell such as external quantum efficiency (EQE) and transparency are discussed in detail. In the first section, the transmission spectrum of the current top cell is analysed. In the next section, different solar cell stacks are fabricated in an attempt to improve the transmission of the top cell and study their effect on the bottom cell performance. Finally, solar cells with different absorber layers are fabricated in an attempt to improve their spectral response.

### 5.1. Motivation

In an ideal design of a four terminal device (4TD) configuration, the top cell absorbs the high energetic photons at a high  $V_{OC} \times FF$  product and transmits the non-absorbed photons completely to the bottom cell. But in reality, not all the non-absorbed photons which leave the top cell absorber layer, reach the bottom cell. The reflection and parasitic absorption losses in the top cell limit the transmission of the top cell and subsequently affect the extent of efficiency gain in the bottom cell. To analyse the transmission of our top cell, a solar with schematics shown in Figure 5.1 is fabricated. Figure 5.2 shows the measured reflectance and transmittance of this top cell. The area between the curves represents the absorption in the solar cell stack. The dotted line in the curve symbolises the absorption edge of the top cell absorber layer. Ideally, beyond this point, the transmission needs to be as high as possible to maximise the absorption in bottom cell. But, as seen in the Figure 5.2, the transmission in our top cell is affected by reflection losses and largely hindered by parasitic absorption in the Asahi substrate (FTO and glass). The textured substrate facilitates scattering of light and results in an increase of absorption of photons in the absorber layer. However, it also aids the free carrier absorption in the FTO layer. This affects the transmission of the current top cell.

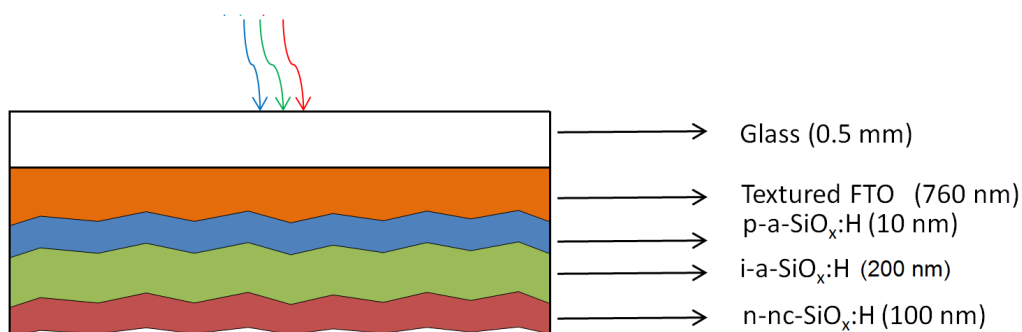


**Figure 5.1:** Schematic representation of a-SiO<sub>x</sub>:H solar cell stack. A back contact is deposited at the bottom of the stack after carrying out reflectance and transmittance measurements.

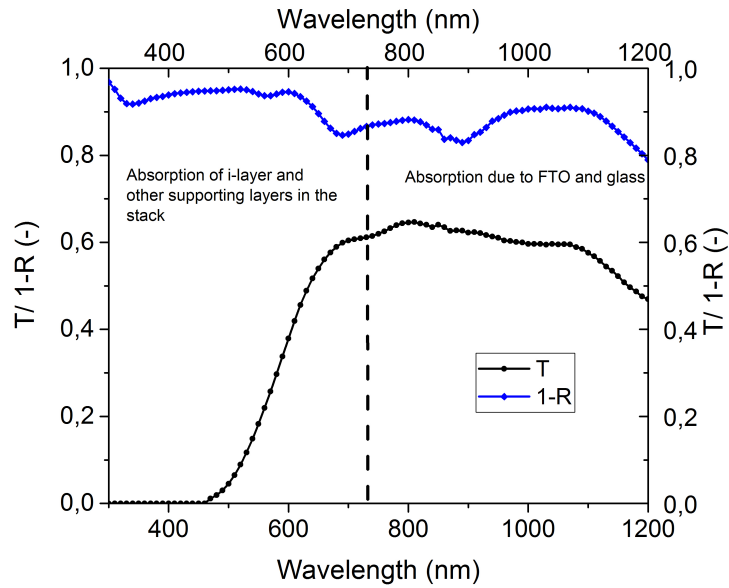


**Figure 5.2:** Reflectance and transmittance measurement of a-SiO<sub>x</sub>:H solar cell stacks.

In this chapter, as an attempt to improve the transmission of the top cell and also to study its effect in a 4TD configuration, solar cell stacks with two different i-layer thickness on Asahi and on a flat aluminium doped zinc oxide (AZO) <sup>1</sup> substrate were fabricated. The fabricated solar cells are compared based on the figure of merits discussed in Chapter 3 and finally, the theoretical efficiency of these solar cells in combination with the CIGS bottom cell (used in Chapter 3) are calculated. The different solar cells fabricated are referred with their substrate name and their corresponding i-layer thickness for descriptive purposes.

## 5.2. Analysis based on figures of merit

### 5.2.1. $V_{OC} \times FF$ product

The purpose of the top cell is to collect the high energetic photons with a high  $V_{OC} \times FF$  product. Figure 5.3 shows the comparison of  $V_{OC} \times FF$  product of the fabricated solar cells. The solar cells on flat AZO substrate have a better  $V_{OC} \times FF$  product for the same i-layer thickness in comparison to the Asahi substrate.

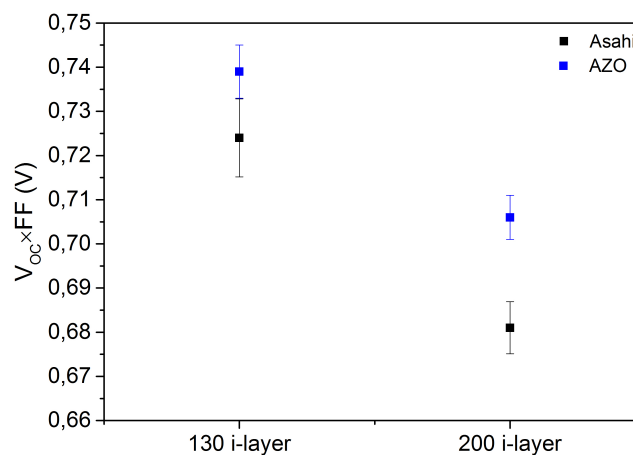


**Figure 5.3:** Comparison of the solar cells based on their  $V_{OC} \times FF$  product.

<sup>1</sup>An 820 nm thick AZO layer was deposited on Corning glass substrate. The substrate was dipped in 0.5% solution of HCl to etch away any spikes like textures in the AZO substrate.

Due to the steep features on the Asahi substrate the thin film growth is affected, inducing micro-crack defects in the valleys of the textured substrate and thus affecting the  $V_{OC}$  and FF of the solar cell [59–61]. On the other hand, the AZO substrate has a flat surface that facilitates more homogeneous growth surface for the thin film material and thus results in solar cells with a high  $V_{OC}$  and FF. Moreover, the sheet resistance of the AZO films is lower than that of Asahi FTO, which results in better TCO-p layer contact and result in a better fill factor [62, 63]. It is worth mentioning that the shunt resistance of the solar cells fabricated on AZO substrate were 50% larger for cells on Asahi substrate thus reducing the shunt leakage current and aiding the increase in fill factor.

The  $V_{OC} \times FF$  product reduces with increasing i-layer thickness due to an increase in bulk recombination in a thicker i-layer. The solar cell AZO (130 nm) has the highest  $V_{OC} \times FF$  product of 0.74 V among all the solar cells fabricated in this work.

### 5.2.2. External Quantum Efficiency (EQE)

An EQE curve is an indication of photocurrent generation in a solar cell with respect to the wavelength of incident light. As shown in Figure 5.4, the solar cells on Asahi substrate show better EQE response throughout their spectral range. The light scattering in the textured Asahi increases the mean path length of the incident photons and aids in increase of absorption in the solar cell [60]. As a consequence, the photocurrent generation in the Asahi substrates is higher compared to the solar cells on a flat substrate.

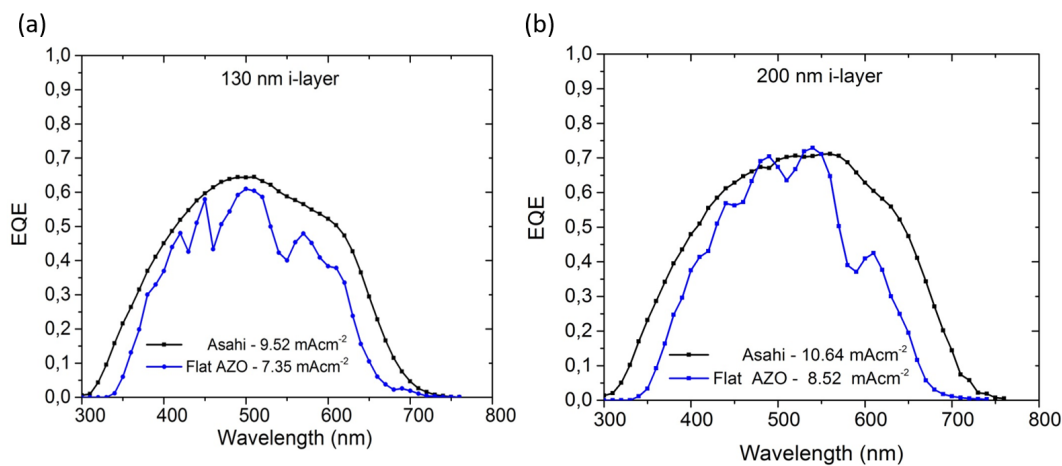


**Figure 5.4:** Comparison of EQE of solar cells on different substrates: (a) 130 nm i-layer; and (b) 200 nm i-layer.

The solar cells on AZO show no EQE response in region from 300 to 350 nm due to their strong UV absorption [64, 65]. The interference pattern in the EQE curve of solar cells on AZO is due to the effect of thin film interference on an optically flat surface. From Figure 5.4 we can see that the EQE curves of solar cells with a thinner i-layer are lower than solar cells with a thicker i-layer. Based on Beer-Lambert's law, absorption of photons increases with absorber layer thickness. As a consequence, a thicker i-layer absorbs more photons and eventually results in higher electron-hole generation leading to a higher  $J_{SC}$ . To conclude the Asahi (200 nm) solar cell has the highest  $J_{SC}$  in comparison to the other solar cells.

### 5.2.3. Transmission of the top cell

The top cell needs to be transparent to maximise the utilisation of non-absorbed photons in the bottom cell. Figure 5.5 compares the transmission of solar cells on different substrates. In general, the transmission of solar cells on flat AZO is higher than that of solar cells on textured Asahi substrate. In a flat AZO substrate, the incoming light takes one single pass through the solar cell stack and the non-absorbed light is transmitted to the bottom cell. But when using a textured substrate, the light is trapped in the top cell and results in more absorption in the top cell leading to a lower transparency compared to a flat substrate. Moreover, due to texturing, the parasitic absorption in the TCO layer in Asahi substrate is higher than that of the flat substrate due to light trapping.

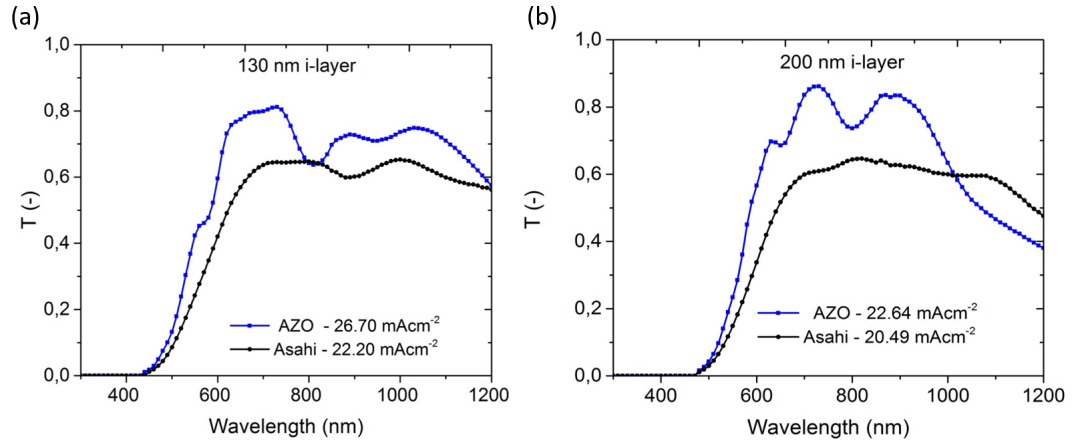


**Figure 5.5:** Comparison of transmission of solar cells on different substrates: (a) 130 nm i-layer; and (b) 200 nm i-layer.

In Figure 5.5, the transmittance of solar cells on both AZO and Asahi are plotted with their equivalent transmitted photocurrent. The photocurrent mentioned here is calculated using the Equation 5.1 where  $T(\lambda)$  is the transmission spectrum of the top cell. The specified spectral range is considered to account for the spectral range of our bottom cell [66]. As implied from the transmitted photocurrent of the solar cells, on both the substrates a 130 nm i-layer shows a higher transmittance. A thinner layer absorbs less photons in comparison with a thicker layer and therefore transmits more amount of light to the bottom cell.

$$J_{ph} = q \int_{300}^{1200} T(\lambda) \cdot \Phi(\lambda) \cdot d\lambda, \quad (5.1)$$

The solar cells are ranked from 1 to 4 in order of their superiority as shown in Table 5.1. The sample AZO (130 nm) shows superior transmission and  $V_{OC} \times FF$  product but a low  $J_{SC}$  value. On the other hand, Asahi (200nm) has the highest  $J_{SC}$  at the cost of their  $V_{OC} \times FF$  and transmission. In the next section, the theoretical efficiency of these solar cells is calculated using the method described in Chapter 3 to know the effects of different figures of merit on a 4TD configuration.

**Table 5.1:** Ranking based on the figures of merit.

Parameters	Asahi (130 nm)	AZO (130 nm)	Asahi (200 nm)	AZO (200 nm)
$V_{OC} \times FF$	2	1	4	3
Transmission	3	1	4	2
$J_{SC}$	2	4	1	3

#### 5.2.4. Theoretical efficiency determination of 4TD using different top cell stacks

The CIGS solar cell mentioned in Table 5.2 is considered as the bottom cell for analysing the performance of above mentioned various top cell device stack in a 4TD configuration. The structure and performance of the CIGS solar cell used in this analysis is discussed in Subsection 3.1.1. The EQE of the bottom cell in the 4TD configuration is predicted with the help of Subsection 3.3.1. Figure 5.6 shows the simulated EQE curve of the bottom cell with different top cell and their corresponding photocurrent ( $J_{SC, Bot}$ ) is used in Equation 5.2 and Equation 5.3 to obtain the  $V_{OC} \times FF$  product and efficiency of bottom cell in the 4TD configuration:

**Table 5.2:** Electrical parameters of the CIGS solar cell - Solliance.

S.No	Cell	$J_{SC}$ (mA/cm <sup>2</sup> )	$V_{OC}$ (V)	Fill factor (FF)	$V_{OC} \times FF$ (V)	Efficiency (%)
1	CIGS	30.02	0.58	0.58	0.34	10.08

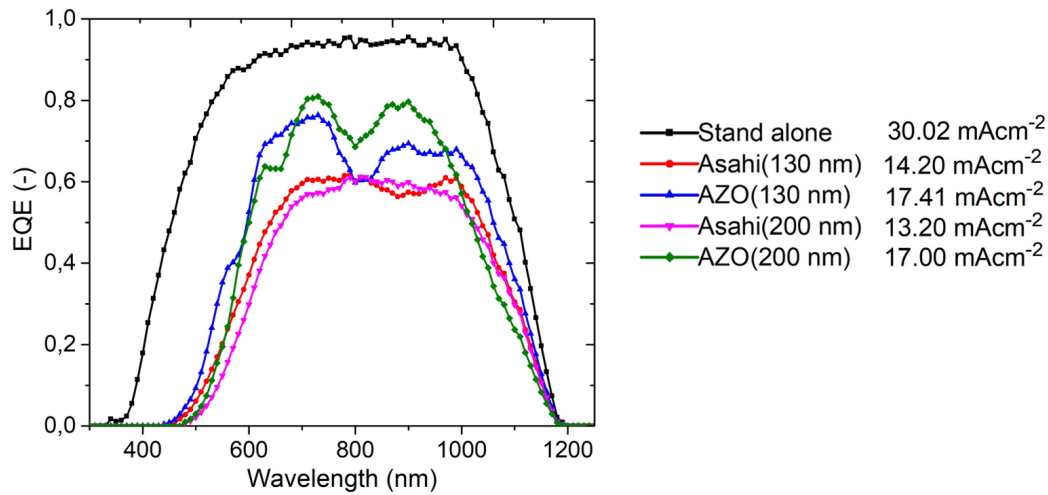


Figure 5.6: EQE of the CIGS solar cell in different 4TD configuration.

As seen in Figure 5.6, the EQE of bottom cell in a combination with AZO top cell is better in comparison to Asahi substrate. Better transmission of AZO substrate helps in higher current generation in bottom cell. The EQE of bottom cell on Asahi (130 nm) is slightly better than that of Asahi (200 nm) resulting in a 1 mAcm<sup>-2</sup> higher current generation in the bottom cell in this configuration.

$$(V_{OC} \times FF)_{Bot} = 0.1861 + 0.02349 \cdot J_{SC,Bot} - 0.00158 \cdot J_{SC,Bot}^2 + 1.59 \cdot 10^{-5} \cdot J_{SC,Bot}^3 \quad (5.2)$$

$$\eta_{Bot}(\%) = (V_{OC} \times FF)_{Bot} \cdot J_{SC,Bot} = (0.1861 + 0.02349 \cdot J_{SC,Bot} - 0.00158 \cdot J_{SC,Bot}^2 + 1.59 \cdot 10^{-5} \cdot J_{SC,Bot}^3) \cdot J_{SC,Bot} \quad (5.3)$$

Equation 5.2 and Equation 5.3 are derived in Chapter 3 and is referred here to carry out the efficiency calculation. Figure 5.7 shows the efficiency of a standalone CIGS solar cell in comparison with various 4TD configuration. All the 4TD configurations result in an increase in efficiency compared to the standalone CIGS solar cell. The combination of Asahi (200) with CIGS solar cell yields maximum efficiency gain of 1.4% and AZO (130) gives minimum efficiency gain of 0.72%. It is noteworthy to mention that, the AZO (130) has the best transmission and highest  $V_{OC} \times FF$  product among all the top cell stack. To conclude, the bottom cells perform better with solar cells on AZO substrate in top owing to better transmission of top cell. However, the overall efficiency gain of the bottom cells in these devices are limited due to the performance of top cell on AZO substrate.

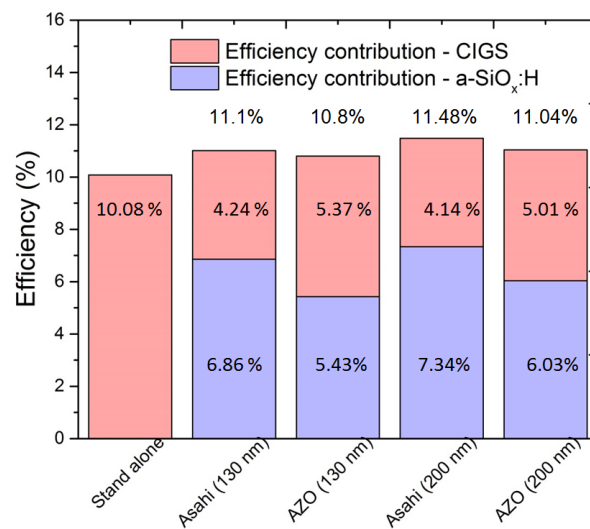


Figure 5.7: Efficiency contribution of the top and bottom cell in a 4TD configuration.

In the 4TD configuration listed above, the combination of Asahi substrate top cells with the bottom cell yields better efficiency gain than AZO substrate cells. In Asahi substrate top cell, due to texturing of the substrate, more photons are absorbed in the top cell and consequently collected at a high  $V_{OC} \times FF$  product of 0.68 V. The efficiency of bottom cell with this configuration is limited due to their transmission. From Figure 5.6 it is clear that the bottom cell generates a  $J_{SC, Bot}$  in the range of 13 to 17.5 mAcm<sup>-2</sup> depending on transmission of the top cell. As the Figure 5.8 suggests, the  $V_{OC} \times FF$  product of the bottom cell for all the combinations listed above is around 0.31 V. Thus, making the top cell transparent at a cost of their current generation would not possibly enhance the 4TD efficiency as the non-absorbed transmitted photons from the top cell are collected at a relatively low  $V_{OC} \times FF$  product.

This shows the importance of photocurrent generation in the top cell. The absorber layer of the top cell needs to as thick as possible and should have the ability to generate more electron-hole pairs at a high  $V_{OC} \times FF$  product. But, the absorber layer thickness of our top cell is limited due to their drop in  $V_{OC} \times FF$  product beyond a i-layer thickness of 200 nm [67]. In next section, top solar cells with lower bandgap absorber layers are fabricated in an attempt to increase the photocurrent generation in the top cell.

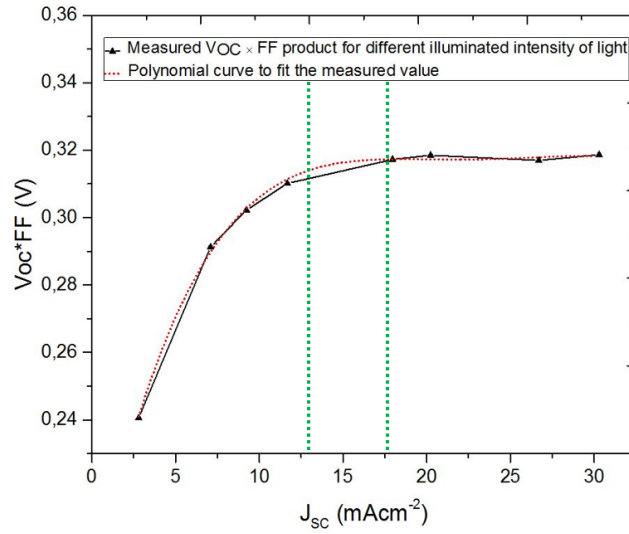


Figure 5.8:  $V_{OC} \times FF$  product of CIGS solar cell at various  $J_{SC}$ .

### 5.3. Top cell characterisation

The top cell needs to be a bifacial solar cell in order to be utilised in a 4TD configuration. A 200-nm thick ITO layer is deposited as back contact for all the solar cells fabricated in this section. To maximise the current generation in the top cell, solar cells with lower bandgap absorber layer compared to one discussed in the previous section were fabricated. All the solar cells were fabricated on Asahi substrate to maximise the current gain in the top cell. The absorber layer thickness of all the solar cells were fixed at 200 nm for sake of comparison. The electrical parameters of the fabricated solar cells are listed in Table 5.3. The cells fabricated are compared with one of the best performing top cell [68] from literature to give more insight on requirement of a top cell in 4TD configuration.

Table 5.3: Electrical parameters of high bandgap solar cells fabricated in comparison with perovskite solar cell.

S.No	Solar cell	$J_{SC}$ (mA/cm <sup>2</sup> )	$V_{OC}$ (V)	Fill factor (FF)	$V_{OC} \times FF$ (V)	Efficiency (%)
1	a-SiO <sub>x</sub> :H (2.03 eV)	9.46	0.98	0.66	0.65	6.12
2	a-SiO <sub>x</sub> :H (1.96 eV)	11.41	0.93	0.67	0.62	7.10
3	a-Si:H	13.30	0.85	0.66	0.56	7.28
4	Perovskite [68]	19.40	1.07	0.78	0.84	16.19

#### 5.3.1. External quantum efficiency (EQE)

Figure 5.9 shows the comparison of EQE of our top cells with perovskite solar cell. As seen from Figure 5.9, reducing the bandgap of the absorber layer helps in widening the spectral response of the solar cell. This

enables the top cell to absorb more photons and collect it at a higher  $V_{OC} \times FF$  product in comparison to  $V_{OC} \times FF$  product of the bottom cell. By extending the top cell's spectral range, the extent of thermalisation losses incurred by the bottom cell also decreases further leading to higher efficiency gain.

The a-Si:H solar cell has the best spectral response among the fabricated solar cells. This can further be enhanced by increasing the absorber layer thickness and employing light management techniques. It is interesting to note that it has a higher spectral response in the visible region of spectrum in comparison to perovskite solar cell. The perovskite solar cell has a wider response in IR region owing to its lower bandgap [68] in comparison to our fabricated solar cell.

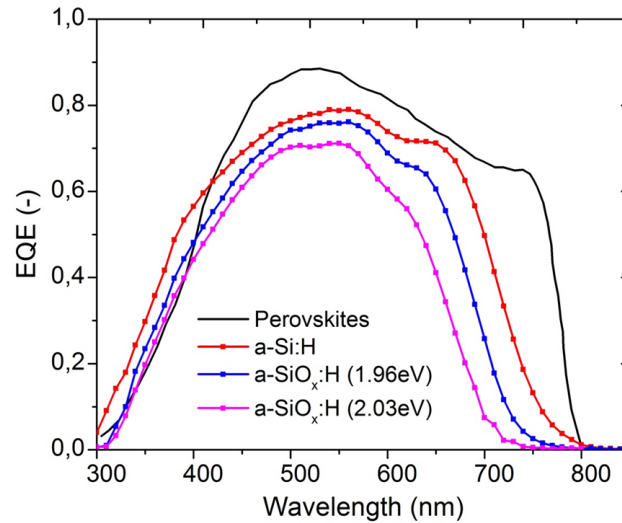


Figure 5.9: Comparison of EQE of various high bandgap solar cells in PVMD group with perovskite solar cell.

### 5.3.2. Transmission of the top cell

Figure 5.10 shows the comparison of transmission spectra of our top cell with perovskite solar cell. Beyond the absorption edge of perovskite solar cell, it shows maximum transmission. The transmission of our top cells are limited in the IR region due reflection and parasitic absorption in the Asahi substrate. As expected, the transmission of a-Si:H and a-SiO<sub>x</sub>:H (1.96 eV) are lower than a-SiO<sub>x</sub>:H (2.03 eV) due to their spectral absorption range.

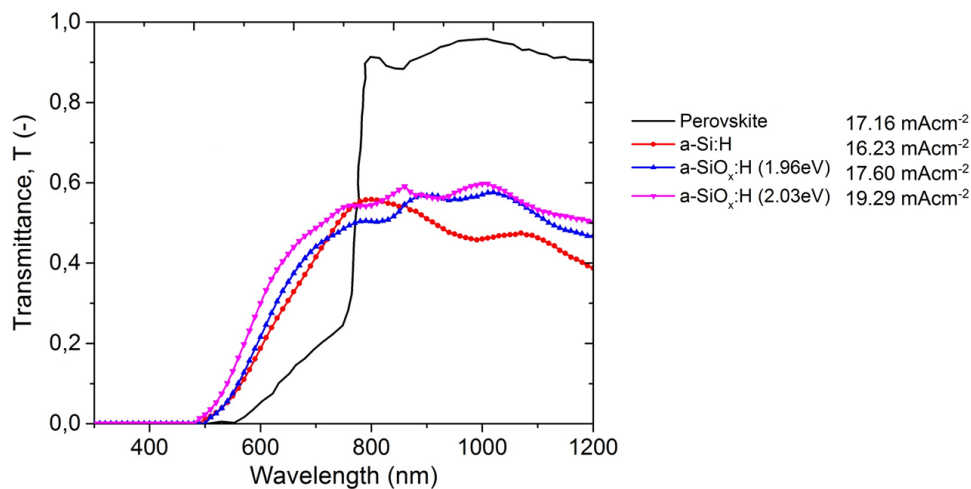


Figure 5.10: Comparison of transmission of various high bandgap solar cells in PVMD group with perovskite solar cell.

### 5.3.3. $V_{OC} \times FF$ product

As seen from Table 5.3, the  $V_{OC} \times FF$  product of the solar cells on ITO are lower when compared to cells on metal back contact (Table 3.2). The low fill factor in these solar cells can be attributed to a lower shunt resistance ( $R_{SH}$ ).  $R_{SH}$  of the solar cells on ITO were 50% lower compared to the solar cells on metal back contact. The tin in the ITO layer acts as an acceptor type defect state and results in a higher recombination rate at then/ITO interface leading to a lower  $V_{OC}$  [69]. The solar cell with a-Si:H shows the lowest  $V_{OC} \times FF$  product of all the cells fabricated. The usage of a low bandgap absorber layer potentially reduces the built in voltage and results in a lower  $V_{OC}$ . The a-SiO<sub>x</sub>:H (1.96 eV) solar cell has a slightly lesser  $V_{OC} \times FF$  product in comparison with a-SiO<sub>x</sub>:H (2.03 eV) solar cell. Due to their wider spectral range and decent  $V_{OC} \times FF$  product, these solar cells are utilised in fabrication of 4TD along with a-SiO<sub>x</sub>:H (2.03 eV) solar cell.

In this work, the a-Si:H solar cell is not utilised in fabrication of 4TD due to their lower  $V_{OC} \times FF$  product and transmission in comparison to our other fabricated devices. The difference in  $V_{OC} \times FF$  product of the top and bottom cell determines the extent of reduction in thermalisation losses of the bottom cell. This difference is least in case of a-Si:H-(CIGS/CIS) combination. The lower transmission of a-Si:H solar cell further reduces the performance of the bottom cell making the combination less effective.

A dedicated study on a-Si:H solar cell for 4TD applications needs to be carried out due to its wide spectral range of absorption. Research on a-Si:H with high  $V_{OC} \times FF$  product have been demonstrated [70] and it would be interesting to investigate further on such devices.

## 5.4. Conclusion

Based on the results shown in this chapter we come to the following conclusions:

- The fabrication of solar cells on AZO substrate resulted in an increase in transmission of the solar cell stack. As a result, bottom cell performed much better with this configuration showcasing the effect of transparency of the top cell. The efficiency gain in these solar cells were still lower in comparison to solar cells on Asahi.
- On both AZO and Asahi substrate, solar cells with thicker i-layer resulted in a higher increase in efficiency gain.
- In spite of having the lowest transmission out of all the fabricated solar cells, Asahi (200) showed the maximum gain in efficiency portraying the importance of current generation in the top cell. This motivated us to go for lower bandgap absorber layer to increase current generation in the top cell.
- Ideally, a combination of higher current generation at the top and good transmission in IR region can result in higher efficiency gain in the bottom cell. It is of paramount importance to develop a new substrate which maximises the current generation at the top and is also transparent in IR region.

Owing to their good  $V_{OC} \times FF$  product and spectral response, the a-SiO<sub>x</sub>:H (1.96 eV) and a-SiO<sub>x</sub>:H (2.03 eV) are further utilised in fabrication of 4TD devices. Due to processing issues with absorber layer deposition in the PECVD system (Amigo) and RF magnetron sputtering system (Zorro), the electrical parameters of a-SiO<sub>x</sub>:H (1.96 eV) and a-SiO<sub>x</sub>:H (2.03 eV) are used in the next chapter to characterise the performance of the top cell.

## Fabrication and characterisation of four terminal devices

In the previous chapter, various top cells were extensively analysed based on figures of merit such as external quantum efficiency (EQE),  $V_{OC} \times FF$  product and their transmission. In this chapter, owing to their good  $V_{OC} \times FF$  product and spectral response, the a-SiO<sub>x</sub>:H (1.96 eV) and a-SiO<sub>x</sub>:H (2.03 eV) are utilised in fabrication of 4TD devices. Due to processing issues with absorber layer deposition in the PECVD system (Amigo) and RF magnetron sputtering system (Zorro), the electrical parameters of a-SiO<sub>x</sub>:H (1.96 eV) and a-SiO<sub>x</sub>:H (2.03 eV) in the previous chapter are used to characterise the performance of the top cell. Thus, the top cell just acts as an optical filter and their effect on bottom cell is characterised. In the first section, steps involved in the fabrication of four terminal devices (4TD) are explained in detail. In the next section, the characterisation of various combination of 4TD devices are carried out. Finally, limitations of the current 4TD configurations are explained with the help of a simple photocurrent balance.

### 6.1. Fabrication of 4TD

#### 6.1.1. Top cell fabrication

Figure 6.1-(a) shows the layout of the top cell. An Asahi substrate with dimension of 5 cm × 5 cm was used for deposition of the p-i-n layers of the solar cell. The transparent conductive oxide (TCO) layer was deposited on the p-i-n solar cell stack using a mask, and the mask layout is shown in Figure 6.1-(b). In this work, different pattern of metal grids were deposited to analyse their effect on fill factor. Due to processing issues in the final stage of the work, this was not accomplished.

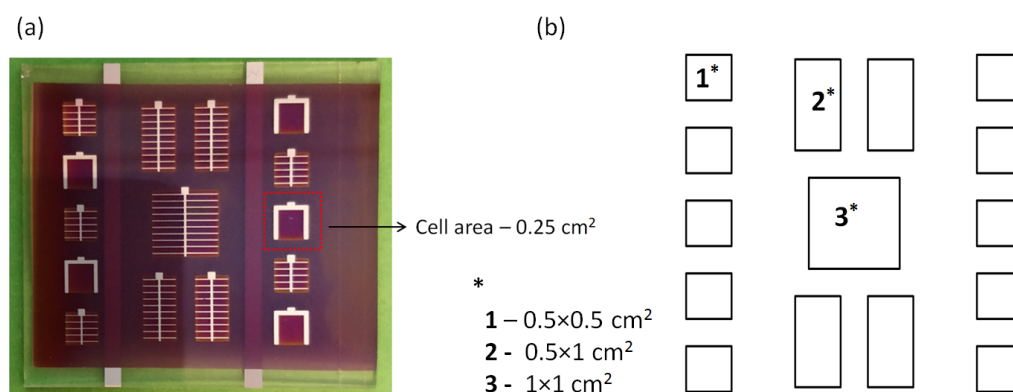
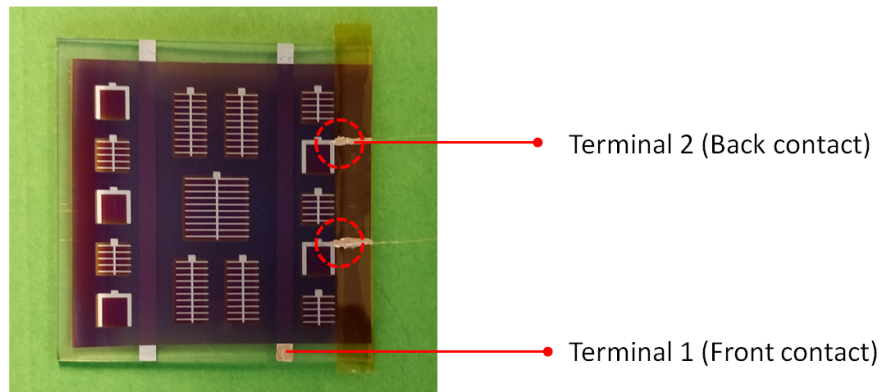


Figure 6.1: Top cell design layout.

In a 4TD configuration, the top cell is placed above the bottom cell and are mechanically stacked together to have the same optical path. The front and back metal contacts of the top cell need to be easily accessible to

characterise the electrical performance in the 4TD configuration. Figure 6.2 shows the methodology adopted to take out contact wiring from the top cell. First, an insulating adhesive tape is stuck near the active area of the solar cell. Next, a silver paste is applied over the metal contact-adhesive tape region as shown by the red circle in Figure 6.2. Finally, a conductive wire was connected with the silver paste and the solar cell was annealed to cure the silver paste. In this way, the external wiring for both front and back metal contacts were obtained.



**Figure 6.2:** Methodology for taking out external wiring from the solar cell.

### 6.1.2. Bottom cell fabrication

Both copper indium gallium selenide (CIGS) and copper indium selenide (CIS) bottom cells used in this work were obtained from Solliance Solar Research. The CIGS/CIS solar cells were fabricated on a 10 cm × 10 cm soda lime glass substrate. The deposited CIGS/CIS solar cell device stack is later scribed into 162 small solar cells, with each cell having a dimension of 1 cm × 0.5 cm. The solar cell obtained from Solliance is cut into a size of 5.5 cm × 5.5 cm to utilise it in the 4TD configuration. The bottom cell layout adopted in this work is shown in Figure 6.3.

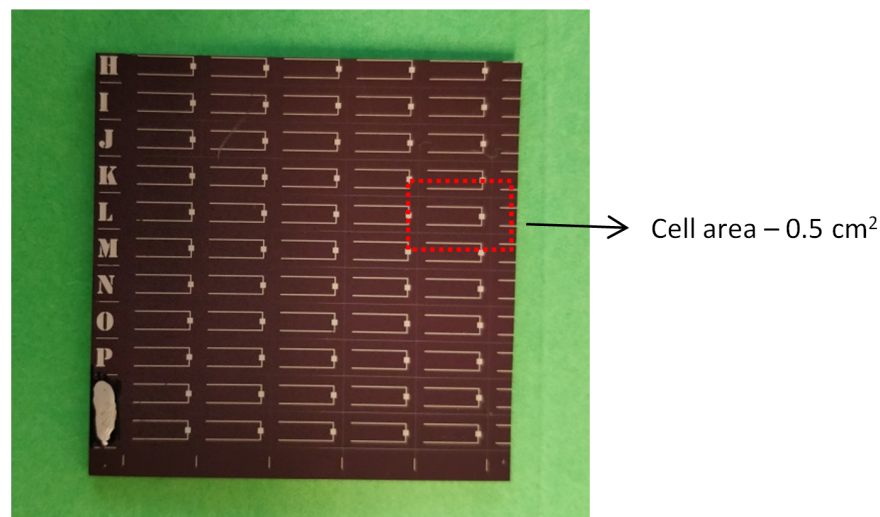


**Figure 6.3:** CIGS/CIS solar cell layout utilised in this work.

The bottom cell is cut into a larger size compared to the top cell to have an easy access to their metal back contact. For accessing their front metal contact, the procedure adopted for the top cell is repeated and an

illustration is shown in Figure 6.4. Due a time consuming process of extraction of the external wiring only few sample spots were analysed for each configuration. A better design can be adopted in the future works.

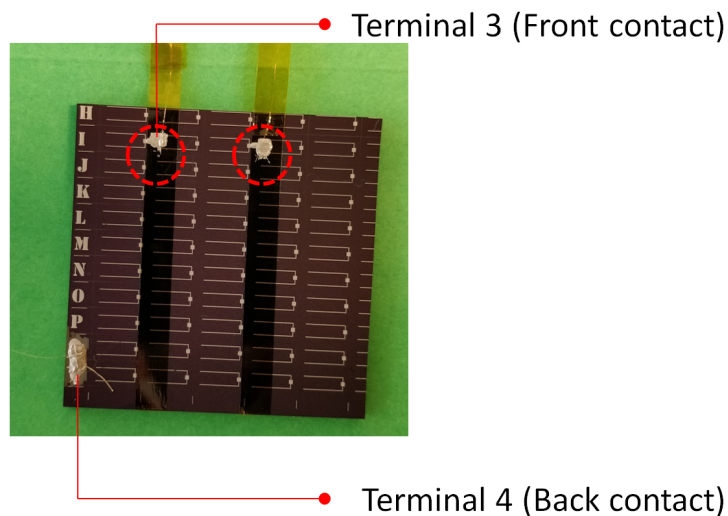


**Figure 6.4:** Methodology for taking out external wiring from the front contact of the bottom cell.

### 6.1.3. 4TD fabrication

In this work, the top cell and bottom cell are coupled together by a process of lamination. The top cell is placed above the bottom cell and a thin layer of ethylene vinyl acetate (EVA) is placed between them. The EVA layer acts as a glue and couple the top and bottom cell together. The solar cell device stack is placed in a laminator and the lamination process occurs in three steps.

- A vacuum is created in the laminator chamber. This ensures that no bubbles or voids are formed between the top and bottom cell.
- Next, the device stack is heated upto 150°C to facilitate polymerisation of EVA.
- Pressure is applied on top of the device stack to enhance the distribution of polymerised EVA. This ensures good adhesion between the top and bottom cell.

The lamination process provides the necessary mechanical stability to the device stack. A prototype of the 4TD device fabricated in this work is shown in Figure 6.5.

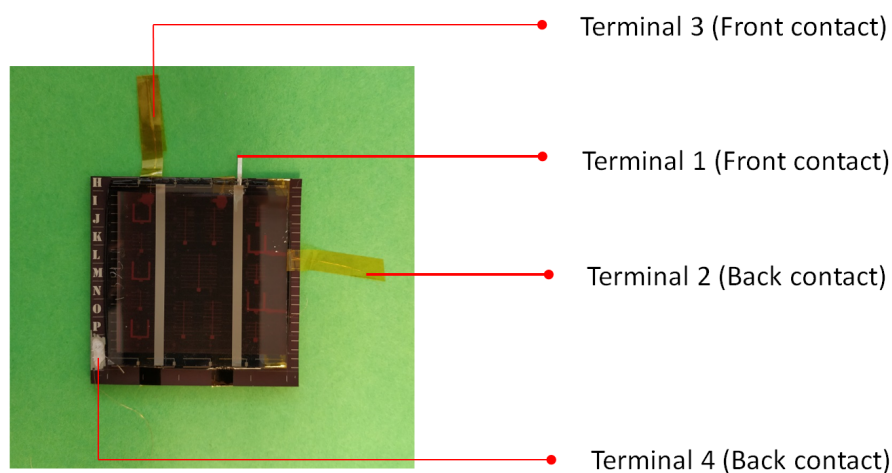


**Figure 6.5:** Image of 4TD with a-SiO<sub>x</sub>:H top cell and CIS bottom cell.

## 6.2. Characterisation of 4TD

### 6.2.1. a-SiO<sub>x</sub>:H (2.03 eV)-CIGS configuration

In this section, 4TD devices with a combination of a-SiO<sub>x</sub>:H (2.03 eV) top cell and CIGS bottom cell are analysed. The a-SiO<sub>x</sub>:H (2.03 eV) with a  $V_{OC} \times FF$  of 0.65 V is utilised as the top cell in this section. Assuming that the bottom cell's reflection does not contribute to current generation in the top cell, the top cell efficiency is assumed at a constant value of 6.12% to simplify the characterisation of 4TD devices. CIGS solar cells namely A1, A2 and A3 are utilised as the bottom cells in the 4TD configuration and their initial efficiency ( $\eta$ ) can be referred from Table 6.1.

The top cell acts as a filter and attenuates the spectrum received by the bottom cell. Left side of Figure 6.6-6.10 show the effect of the a-SiO<sub>x</sub>:H (2.03 eV) top cell on performance of the bottom cell. As shown in the Figure 6.6 and Figure 6.7, the short-circuit current density ( $J_{SC}$ ) decreases to around half of its initial value and the open circuit voltage ( $V_{OC}$ ) decreases as well. The huge drop in  $J_{SC}$  can be attributed to its linear dependency on incident irradiance. The gradual drop in  $V_{OC}$  can be attributed to its logarithmic dependency on the incident irradiance. As shown in Figure 6.8, apart from the solar cell A1, the fill factor (FF) of the bottom cell shows an increasing trend in the 4TD configuration. The increase in FF can be accounted for the increase in shunt resistance ( $R_{Sh}$ ) of the bottom cell (Figure 6.9). At reduced irradiation level, photoactive defective regions in a solar cell tend to become inactive and result in an increase of  $R_{Sh}$  [71]. The series resistance on the other hand increases as the conductivity of the photoactive layer reduces with the drop in irradiance.

As shown in Figure 6.10, the extent of efficiency gain ( $\eta_{gain}$ ) of the bottom cell is higher for a low performing bottom cell. A1 shows the highest  $\eta_{gain}$  of 1.58%. A1 has the lowest  $V_{OC} \times FF$  of 0.23 V in comparison to other samples in the analysis. Thus, the extent of reduction of thermalisation loss in the bottom cell is higher and consequently leading to a higher  $\eta_{gain}$ . Whereas, A3 has the highest  $V_{OC} \times FF$  of 0.39 V and the reduction in thermalisation loss in A3 would be comparatively less. This shows that, the  $\eta_{gain}$  is limited for a better performing bottom cell. To enhance the performance of the bottom cell and thereby provide a better  $\eta_{gain}$  in the 4TD configuration, the top cell needs to have better transmission in IR region.

**Table 6.1:** 4TD efficiency for CIGS solar cells with a-SiO<sub>x</sub>:H (2.03 eV) solar cell as the top cell.

S.NO	Bottom cell	$V_{OC} \times FF$ (V)	$\eta$ (%)	$\eta_{Bot}$ (%)	$\eta_{Top}$ (%)	$\eta_{4TD}$ (%)	$\eta_{gain}$ (%)
1	A1	0.23	8.60	4.06	6.12	10.18	1.58
2	A2	0.34	10.78	5.58	6.12	12.30	0.92
3	A3	0.39	12.71	6.63	6.12	12.75	0.04

### 6.2.2. a-SiO<sub>x</sub>:H (1.96 eV)-CIGS configuration

In this section, To study the effect of top cell with a lower bandgap absorber layer, 4TD devices with a combination of a-SiO<sub>x</sub>:H (1.96 eV) top cell and CIGS bottom cell are fabricated and analysed. The a-SiO<sub>x</sub>:H (1.96 eV) with a  $V_{OC} \times FF$  of 0.62 V is utilised as the top cell in this section. Again, assuming that the top cell's efficiency is not affected by the bottom cell's reflection, their efficiency is assumed at a constant value of 7.10% to simplify the characterisation of 4TD devices. The motivation to shift to a lower bandgap absorber is to facilitate a higher absorption of high energetic photons in the top cell. As a result, the transmission of the a-SiO<sub>x</sub>:H (1.96 eV) is lower in comparison to a-SiO<sub>x</sub>:H (2.03 eV). CIGS solar cells namely B1, B2 and B3 are utilised as the bottom cells in the 4TD configuration. The initial efficiency ( $\eta$ ) of the bottom cells can be referred from Table 6.2.

Right side of Figure 6.6-6.10 show the effect of the a-SiO<sub>x</sub>:H (1.96 eV) top cell on performance of the bottom cell. Due to increase in absorption at the top, the transmission of the current top cell is less compared to the previous configuration. As a result, the  $J_{SC}$  and  $V_{OC}$  show a further reduction and results in a drop in efficiency of the bottom cells ( $\eta_{Bot}$ ) in comparison to the previous section.

As shown in Table 6.2, similar to previous section, the increase in  $\eta_{gain}$  of the bottom cell is higher for a low performing bottom cell. It is interesting to see that the extent of  $\eta_{gain}$  of the bottom cell is slightly better with this configuration. For example, in the previous section, the solar cell A3 performs at an efficiency of 12.71% in a stand alone system and with an efficiency of 12.75% in a 4TD configuration. The  $\eta_{gain}$  of such a device is 0.04%. Solar cell B2, which has a similar efficiency range similar to A3, performs at an efficiency of 12.97% in the 4TD configuration, with a higher efficiency gain of 0.25%. It is worthy to note that the bottom cell efficiency of A3 is higher in comparison to B2 ( $\eta_{Bot,A3} > \eta_{Bot,B2}$ ). In this case, the performance of the top

cell negates for their low transmission and results in a higher efficiency gain. A similar trend can be inferred by comparing sample (A1,B1) and (A2,B3). This shows that, higher absorption at the top cell consequently translates into a higher efficiency gain in a 4TD configuration.

**Table 6.2:** 4TD efficiency for CIGS solar cells with a-SiO<sub>x</sub>:H (1.96 eV) solar cell as the top cell.

S.NO	Bottom cell	$V_{OC} \times FF$ (V)	$\eta$ (%)	$\eta_{Bot}$ (%)	$\eta_{Top}$ (%)	$\eta_{4TD}$ (%)	$\eta_{gain}$ (%)
1	B1	0.27	8.92	4.78	7.10	11.88	2.96
2	B2	0.39	12.72	5.87	7.10	12.97	0.25
3	B3	0.36	11.81	5.70	7.10	12.80	0.99

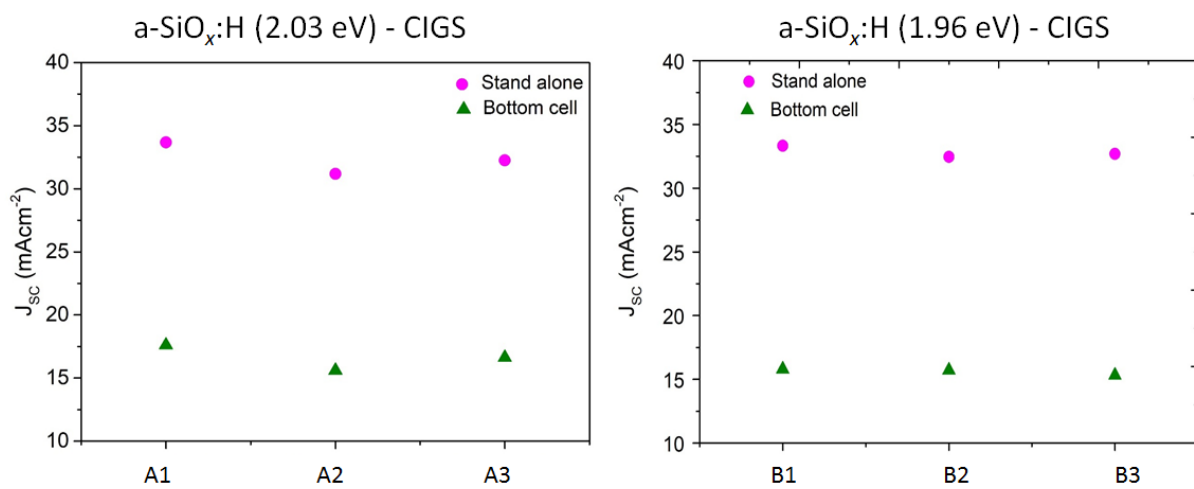


**Figure 6.6:** Variation in short-circuit current of CIGS in stand alone configuration and as a bottom cell with 2.03 eV(left) and 1.96 eV(right) a-SiO<sub>x</sub>:H top cell.

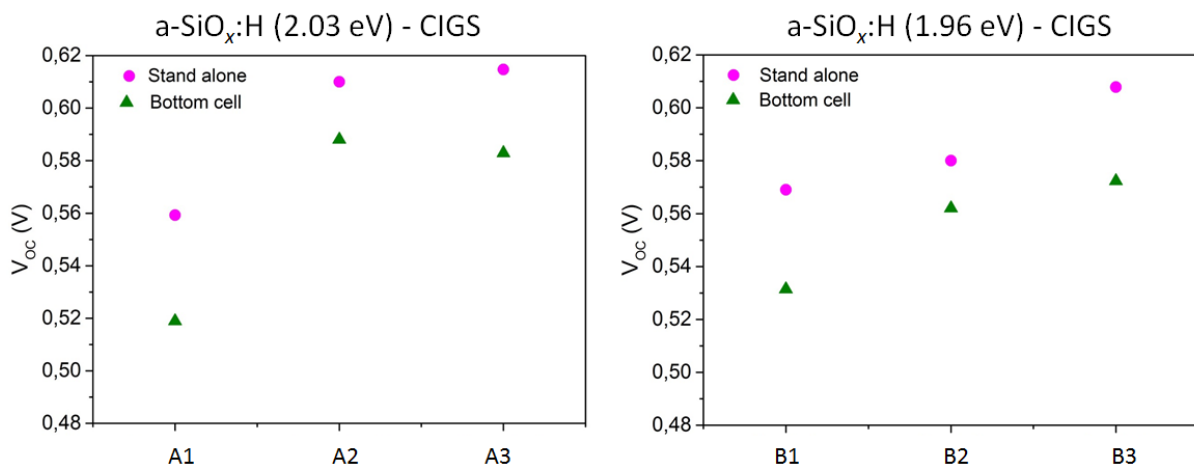


**Figure 6.7:** Variation in open-circuit voltage of CIGS in stand alone configuration and as a bottom cell with 2.03 eV(left) and 1.96 eV(right) a-SiO<sub>x</sub>:H top cell.

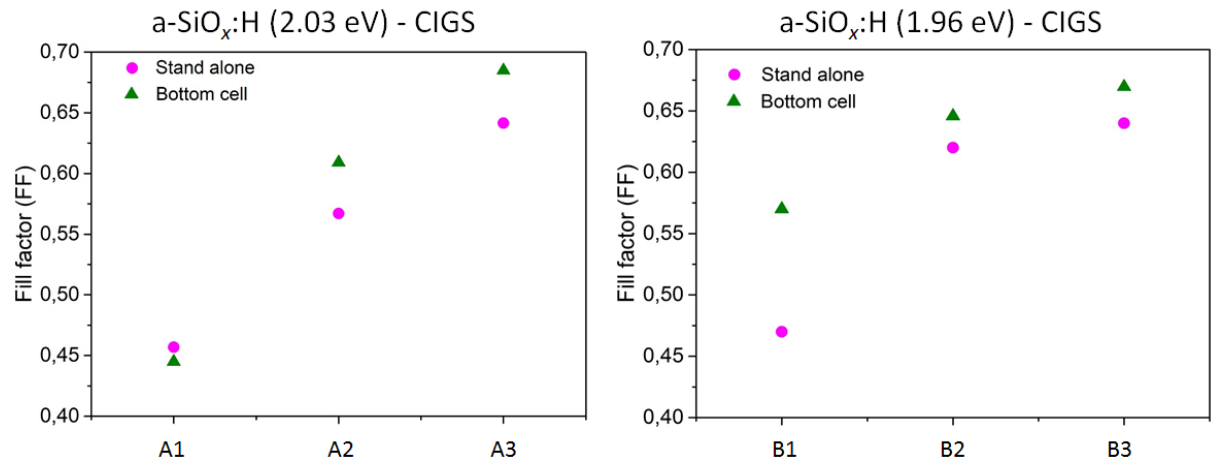


**Figure 6.8:** Variation in fill factor of CIGS in stand alone configuration and as a bottom cell with 2.03 eV(left) and 1.96 eV(right) a-SiO<sub>x</sub>:H top cell.

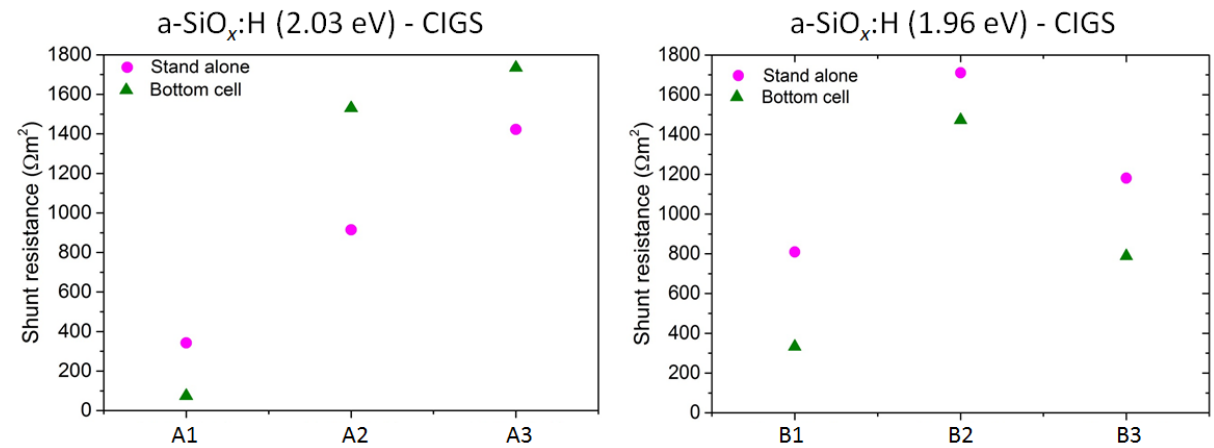


**Figure 6.9:** Variation in shunt resistance of CIGS in stand alone configuration and as a bottom cell with 2.03 eV(left) and 1.96 eV(right) a-SiO<sub>x</sub>:H top cell.

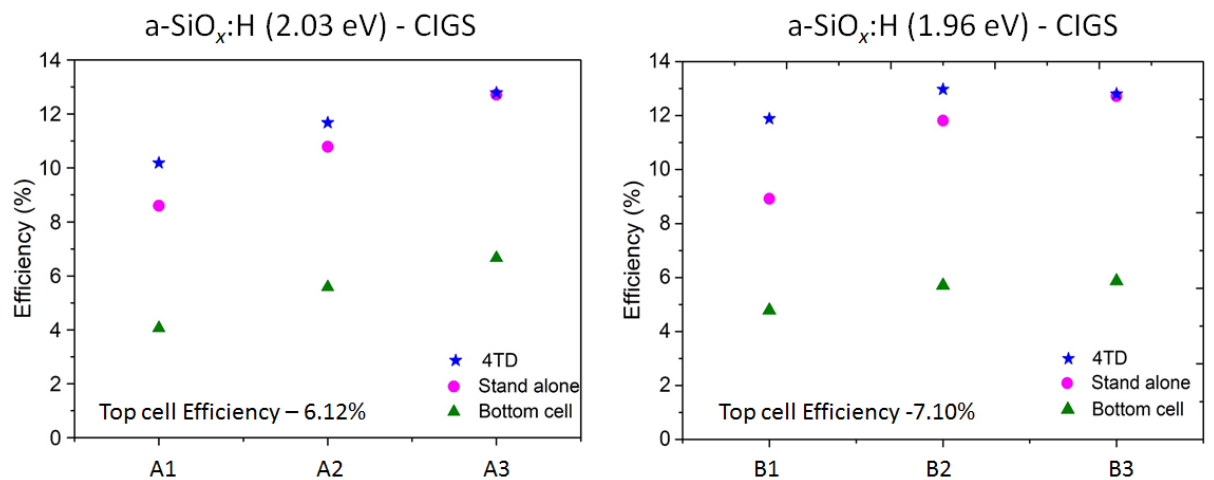


**Figure 6.10:** Efficiency comparison of CIGS in stand alone configuration and as a bottom cell with 2.03 eV(left) and 1.96 eV(right) a-SiO<sub>x</sub>:H top cell.

The effectiveness of a 4TD configuration can further be enhanced by using a lower bandgap bottom cell which results in

- a solar cell with a lower  $V_{OC} \times FF$  product bottom cell. As a result, a higher difference in the  $V_{OC} \times FF$  product between the top and bottom cell could translate into efficiency gain of the bottom cell.
- A lower bandgap bottom cell results in a wider absorption range and a better utilisation of the AM 1.5 spectrum.

This motivates us to use a lower bandgap bottom cell. The bandgap of CIGS solar cell varies as a function of Ga/(Ga+In) ratio in the CIGS material stoichiometry [72]. By removing Ga completely from the material structure, CIS solar cell with a bandgap of 0.95 eV [73] can be fabricated. Figure 6.11 compares the EQE of CIGS and CIS solar cell from Solliance. The CIS solar cell has a wider spectral response in IR region due to their lower bandgap. This motivates us to use CIS solar cell as the bottom cell in 4TD configuration. In the next section, the CIGS solar cell (1.05-1.11 eV) is replaced with CIS solar cell (0.95 eV) as the bottom cell and their performance is characterised.

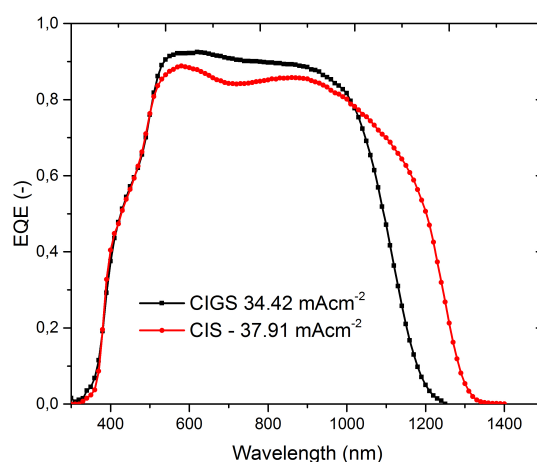


**Figure 6.11:** EQE comparison of CIGS and CIS solar cell.

### 6.2.3. a-SiO<sub>x</sub>:H (2.03 eV)-CIS configuration

In an attempt to study the effect of a low bandgap bottom cell in 4TD configuration, 4TD devices with a combination of a-SiO<sub>x</sub>:H (2.03 eV) top cell and CIS bottom cell are fabricated and analysed in this section. The top cell efficiency is assumed at a constant value of 6.12%. CIS solar cells namely C1, C2 and C3 are utilised as bottom cells in the 4TD configuration. The initial efficiency ( $\eta$ ) of the bottom cells can be referred from Table 6.3.

As seen from Figure 6.12, the  $J_{SC}$  of the standalone CIS solar cells are higher than CIGS solar cell due to their wider range of absorption. The effect of top cell on the bottom cell's electrical parameters are represented from Figure 6.12-6.16. The variation of electrical parameters of the bottom cell with the top cell follow a similar trend as shown in the previous sections. As shown in Table 6.3, the  $\eta_{gain}$  in the CIS solar cell is higher than the CIGS solar cell. The gain in efficiency with this configuration is around 3% but the stand alone cell efficiency of the bottom cells are relatively lower and thus aids in the extent of increase in efficiency. In the next section, the same bottom cell is utilised with a lower bandgap top cell to investigate further on the effect of a low bandgap bottom cell.

**Table 6.3:** 4TD efficiency for CIS solar cells with a-SiO<sub>x</sub>:H (2.03 eV) solar cell as the top cell.

S.NO	Bottom cell	$V_{OC} \times FF$ (V)	$\eta$ (%)	$\eta_{Bot}$ (%)	$\eta_{Top}$ (%)	$\eta_{4TD}$ (%)	$\eta_{gain}$ (%)
1	C1	0.16	5.82	2.96	6.12	9.08	3.26
2	C2	0.17	6.02	3.42	6.12	9.54	3.52
3	C3	0.18	7.20	3.94	6.12	10.06	2.86

### 6.2.4. a-SiO<sub>x</sub>:H (1.96 eV)-CIS configuration

Finally, 4TD devices with a combination of a-SiO<sub>x</sub>:H (1.96 eV) top cell and CIS bottom cell are analysed. In this section, the top cell efficiency is assumed at a constant value of 7.10%. CIS solar cells namely D1, D2 and D3 are utilised as the bottom cells in the 4TD configuration. The initial efficiency ( $\eta$ ) of the bottom cells can be referred from Table 6.4.

The effect of a-SiO<sub>x</sub>:H (1.96 eV) top cell on the bottom cell's electrical parameters are represented in the right side of Figure 6.12-6.16. Due to increase in absorption at the top, the transmission of the current top cell is less compared to the previous configuration. As a result, the  $J_{SC}$  and  $V_{OC}$  show a further reduction and results in drop in efficiency of the bottom cells ( $\eta_{Bot}$ ) in comparison to the previous section.

But, the extent of  $\eta_{gain}$  in the current configuration is highest in comparison to all the previous configuration. For example cell D3 and cell A1 have the same initial efficiency of 8.60%. But the  $\eta_{gain}$  is 0.80% more compared to  $\eta_{gain}$  of A1. Moreover, it is noteworthy to mention that a highest gain in efficiency of 4.40% is achieved with this configuration.

This supports our motivation to use a lower bandgap top and bottom cell. The next section analyses the bottlenecks of our 4TD configuration.

**Table 6.4:** 4TD efficiency for CIS solar cells with a-SiO<sub>x</sub>:H (1.96 eV) solar cell as the top cell.

S.NO	Bottom cell	$V_{OC} \times FF$ (V)	$\eta$ (%)	$\eta_{Bot}$ (%)	$\eta_{Top}$ (%)	$\eta_{4TD}$ (%)	$\eta_{gain}$ (%)
1	D1	0.15	5.42	2.72	7.10	9.82	4.40
2	D2	0.19	7.74	4.25	7.10	11.35	3.61
3	D3	0.23	8.62	3.90	7.10	11.00	2.38

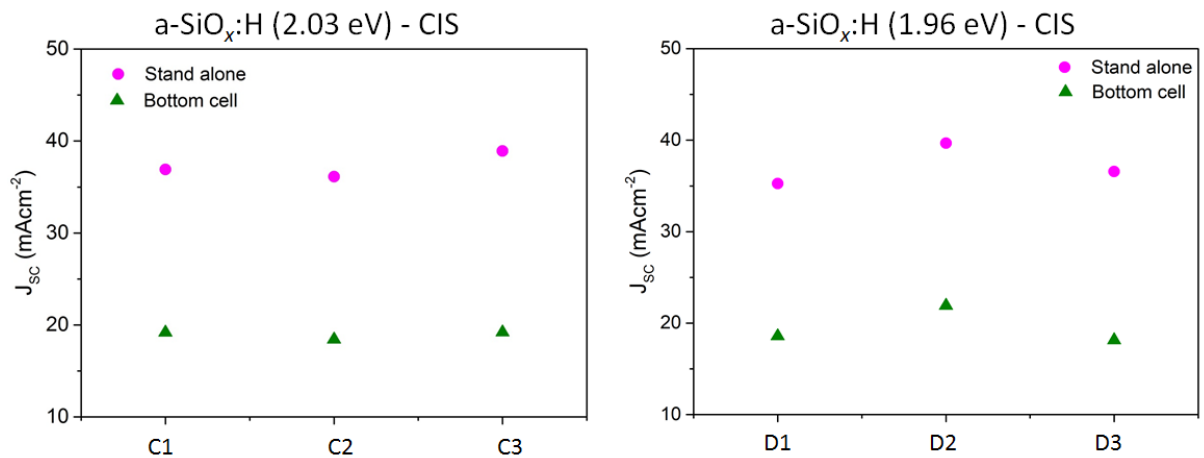


**Figure 6.12:** Variation in short-circuit current of CIS in stand alone configuration and as a bottom cell with 2.03 eV(left) and 1.96 eV(right) a-SiO<sub>x</sub>:H top cell.

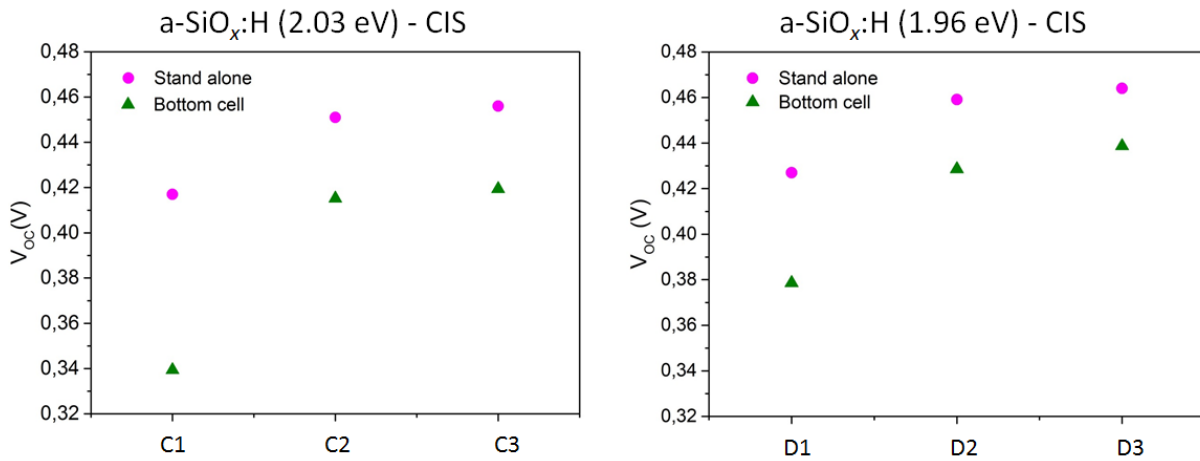


**Figure 6.13:** Variation in open-circuit voltage of CIS in stand alone configuration and as a bottom cell with 2.03 eV(left) and 1.96 eV(right) a-SiO<sub>x</sub>:H top cell.

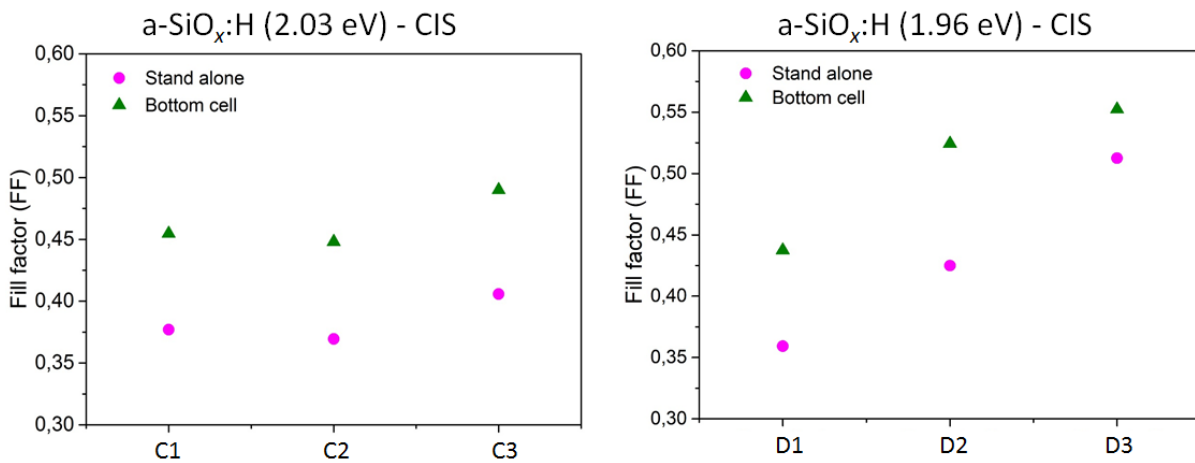


**Figure 6.14:** Variation in fill factor of CIS in stand alone configuration and as a bottom cell with 2.03 eV(left) and 1.96 eV(right) a-SiO<sub>x</sub>:H top cell.

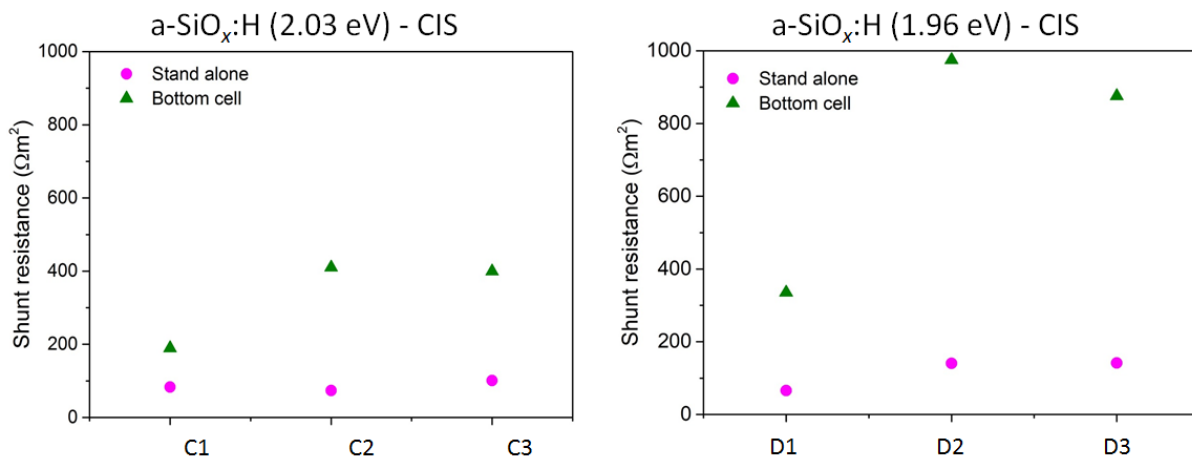


**Figure 6.15:** Variation in shunt resistance of CIS in stand alone configuration and as a bottom cell with 2.03 eV(left) and 1.96 eV(right) a-SiO<sub>x</sub>:H top cell.

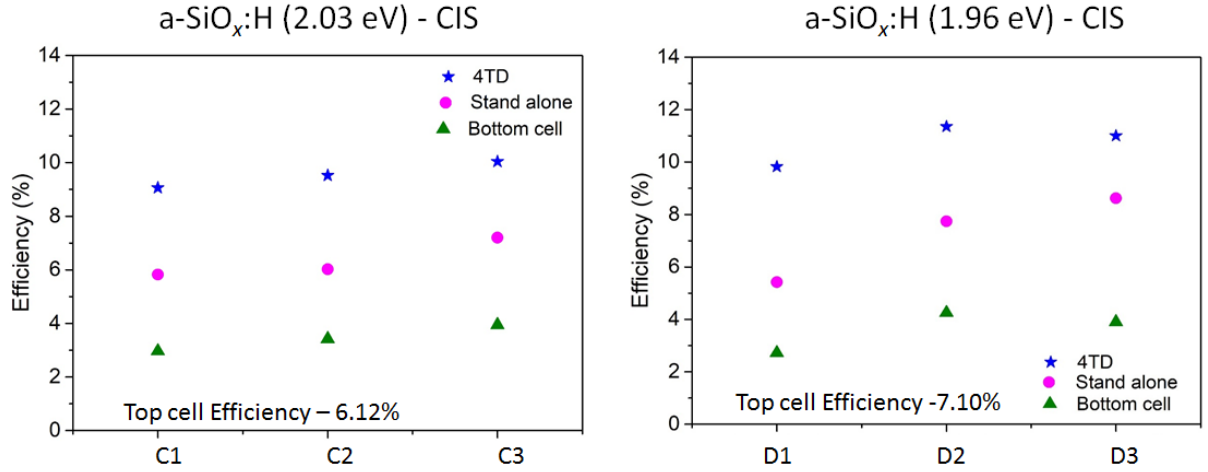


**Figure 6.16:** Efficiency comparison of CIS in stand alone configuration and as a bottom cell with 2.03 eV(left) and 1.96 eV(right) a-SiO<sub>x</sub>:H top cell.

### 6.3. Limitation of the current 4TD configuration

Figure 6.17 shows the EQE and the reflectance of an a-SiO<sub>x</sub>:H (1.96 eV)-CIGS based 4TD configuration in the spectral range from 300 to 1250 nm, as well as the transmission of the top cell. The EQE of the top and bottom cells are combined to show the total spectral response of the 4TD. The area between the reflectance and EQE curves of the system represents the absorption in the supporting layers in the solar cell stack. The optical system of this 4TD configuration can be quantitatively analysed by carrying out a photocurrent balance. The incident photons from the AM 1.5 spectrum are either absorbed in the solar cell stack or reflected/transmitted into air. The absorbed photocurrent in the solar cell stack can be accounted to absorption in the photoactive layer ( $J_{EQE}$ ) and absorption in the supportive layers ( $J_{SL}$ ). In our case, the transmission of the current optical system is zero as the metal contact of the bottom cell reflects all the non-absorbed photons back to the solar cell stack.

The total available photocurrent ( $J_A$ ) in the AM 1.5 spectrum in the spectral range of 300 to 1250 nm is calculated using the Equation 6.1. The equivalent photocurrent due to absorption ( $J_{EQE}$ ) and reflectance ( $J_R$ ) in the 4TD stack is calculated using Equation 6.2, where  $M(\lambda)$  denotes  $R(\lambda)$  or  $EQE(\lambda)$ .

$$J_A = q \int_{300}^{1250} \Phi(\lambda) \cdot d\lambda \quad (6.1)$$

$$J_{EQE/R} = q \int_{300}^{1250} M(\lambda) \cdot \Phi(\lambda) \cdot d\lambda \quad (6.2)$$

From Equation 6.1, the total available photons in the specified spectral range is calculated to be 48.52 mA cm<sup>-2</sup>. The calculated photocurrent absorption in the photoactive layer ( $J_{EQE}$ ) and photocurrent reflectance ( $J_R$ ) is calculated to be 27.13 and 5.20 mA cm<sup>-2</sup> respectively.

The available photocurrent gets redistributed over several current components as represented in Equation 6.3.

$$J_A = J_{EQE} + J_R + J_{SL}. \quad (6.3)$$

By substituting the values of  $J_A$ ,  $J_{EQE}$  and  $J_R$  in Equation 6.3, absorption in the supporting layers is calculated to be 16.19 mA cm<sup>-2</sup>. The absorption in the supporting layers is not converted into useful energy. From Figure 6.17, it is evident that the spectral response of the 4TD stack from 800 to 1250 nm is affected due to parasitic absorption in the top cell. In the next chapter, ways to minimise these absorption losses are elaborately explained.

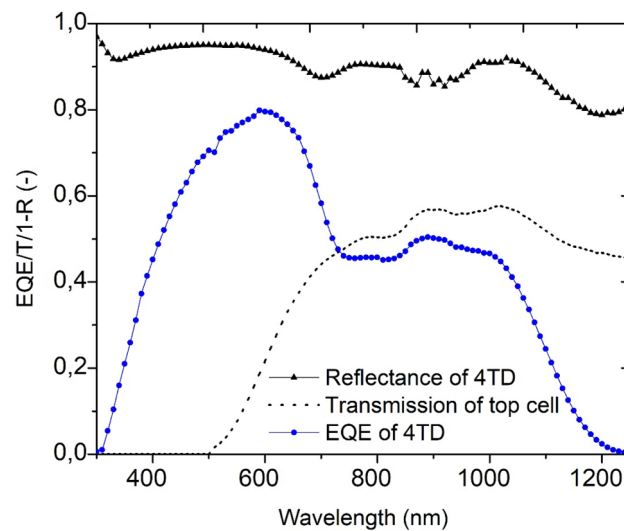


**Figure 6.17:** Optical response of the a-SiO<sub>x</sub>:H (1.96 eV)-CIGS 4TD configuration.

## 6.4. Conclusion

Based on the results shown in this chapter, we can come to the following conclusions:

- In general, the a-SiO<sub>x</sub>:H solar cell as a top cell in a 4TD configuration, results in an increase in efficiency of both CIGS and CIS bottom cell. The extent of increase in efficiency depends on the performance of the bottom cell. The a-SiO<sub>x</sub>:H (1.96 eV)-CIS configuration showcased the highest efficiency gain of 4.40% among the tested samples. In general, the extent of efficiency gain is higher for a low performing bottom cell. A bottom cell with 12.71% efficiency showed a minimal efficiency gain of 0.04%. This shows that the top cell needs further optimisation in order to replicate its success for high performing bottom cells.
- Improving the absorption at the top and the bottom cell results in higher efficiency gain in the bottom cell in a 4TD configuration. The extent of efficiency gain in solar cell D3 (CIS) and A1(CIGS) supports the following conclusion. With the same initial bottom cell efficiency, D3 showed a higher efficiency gain due to a lower bandgap absorber layer at the top.
- Currently, the extent of efficiency gain in the bottom cell using the a-SiO<sub>x</sub>:H based top cell is affected by both reflection and parasitic absorption losses. The photocurrent balance suggests that around 33% of the available photocurrent is absorbed in the supporting layers and does not contribute to any energy conversion. This suggests that the optical system of the top cell needs to be optimised, in order to obtain a high efficiency gain in the bottom cell.



## Optical analysis of a-SiO<sub>x</sub>:H solar cell using GenPro4 simulations

As seen from the previous chapter, the efficiency gain by adopting the current a-SiO<sub>x</sub>:H solar cell as the top cell in a four terminal device (4TD) configuration is limited due to its low transmittance. A proper optical analysis is required to identify the bottlenecks and explore possible solutions. In this chapter, a detailed analysis on the top cell is performed and ways to maximise its i-layer absorption and transmittance are discussed. In first section, a brief introduction about the current absorption spectra of the top cell is discussed. In the next section, the optical simulation software used in this work is introduced and a comparison between the measured and simulated absorption spectra of the top cell is carried out. Finally, ways to enhance the utilisation of available photo current in the current solar cell stack is discussed.

### 7.1. Motivation

The available photocurrent ( $J_A$ ) in the AM 1.5 spectrum can be calculated using Equation 7.1, where  $\Phi(\lambda)$  represents the photon flux at wavelength ( $\lambda$ ). The integral range in the equation is based on spectral response range of our CIGS bottom cell and the corresponding  $J_A$  is calculated to be 46.46 mA/cm<sup>2</sup>. To realise high efficiency gain in a four terminal device (4TD) configuration, it is essential to maximise the utilisation of ( $J_A$ ).

$$J_A = q \int_{300}^{1200} \Phi(\lambda) \cdot d\lambda \quad (7.1)$$

Figure 7.1-(A) shows how the current a-SiO<sub>x</sub>:H solar cell responds to A.M 1.5 spectrum and Figure 7.1-(B) shows the relative distribution of  $J_A$  in the a-SiO<sub>x</sub>:H solar cell. The measured EQE, transmittance and reflectance of the top cell are plotted as a function of the wavelength. The equivalent photocurrent ( $J_L$ ) due to reflectance, transmittance and EQE mentioned in the plot are calculated using Equation 7.2, where  $M(\lambda)$  denotes  $R(\lambda)/T(\lambda)/EQE(\lambda)$ .

$$J_L = q \int_{300}^{1200} M(\lambda) \cdot \Phi(\lambda) \cdot d\lambda \quad (7.2)$$

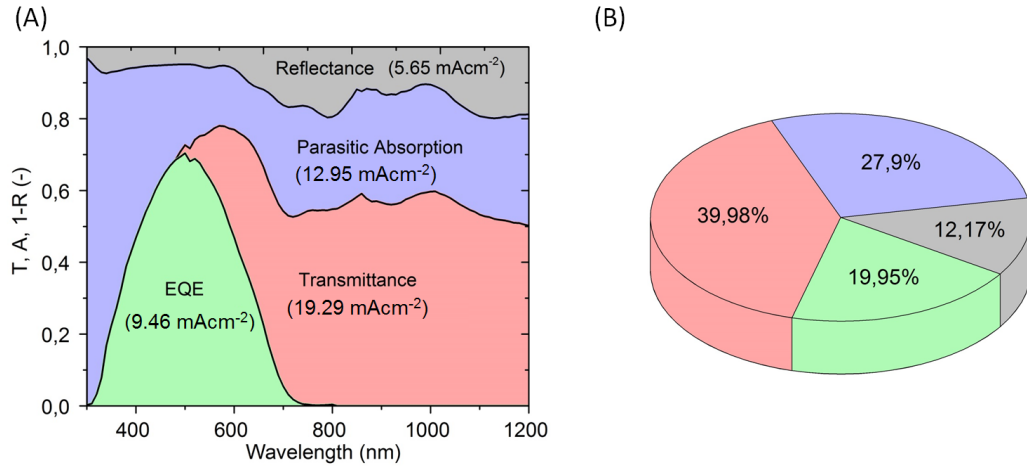


**Figure 7.1:** (A) optical response of the current top cell; and (B) relative distribution of  $J_A$  in the current top cell.

The current top cell utilises nearly 20% of the available  $J_A$  and transmits almost 40% to the bottom cell. Depending on the EQE of the bottom cell, a part of the transmitted light is converted into useful photocurrent. About 40% of  $J_A$  is lost due to reflection losses and parasitic absorption. These losses need to be minimised to realise an efficiency gain in a 4TD configuration with a-SiO<sub>x</sub>:H solar cell as its top cell. In this chapter, an optical analysis is carried out to examine the source of parasitic absorption and reflection, and suitable solutions are proposed and simulated to maximise the utilisation of  $J_A$ . The top cell is considered as an independent entity and the focus of this chapter is to maximise the absorption of light in i-layer and transmittance of the top cell.

## 7.2. Optical simulation of a-SiO<sub>x</sub>:H solar cell

At a certain angle of incidence, the reflection, transmission and absorption of light in a layer of material depends on its refractive index ( $n$ ), extinction coefficient ( $k$ ) and thickness ( $d$ ). In a well defined optical system, the reflectance ( $R$ ) and transmittance ( $T$ ) of a layer can be calculated with the help of the Fresnel equations and Beer-Lambert law. A thin film solar cell can be considered as a stack of different layers with distinct optical properties. Thus, it is possible to predict the optical behaviour of a solar cell to an incident spectrum with the help of  $n$ ,  $k$  and  $d$  values of each and every individual layer and by solving the Fresnel equations and Beer-Lambert law at every interface of the solar cell with the help of well defined boundary conditions. In this chapter, the optical simulation software called GenPro4 [45], which works on the above mentioned approach, is utilised to simulate the optical behaviour of a solar cell.

GenPro4 is a highly effective tool, which utilises both wave and ray-optics to model the behaviour of a solar cell. It is purely an optical model and does not consider any electrical properties of the simulated layer. The simulation provides the absorbance profile of each and every layer and also provides the absorbed photocurrent.

### 7.2.1. Optical simulation of top cell with back contact

In this section, the optical behaviour of an a-SiO<sub>x</sub>:H solar cell with a back contact in a p-i-n (10-175-100) structure is simulated. The simulated results are compared with the measured parameters to check the accuracy of the input parameters fed into the optical model. The input parameters for the optical simulations are  $n$ ,  $k$  and  $d$  values of each and every individual layer and its surface morphology. AFM scan of the Asahi substrate is fed into the optical model and the model invokes a scalar scattering model which uses the morphology of the substrate to predict their angular intensity distribution (AID) [74]. The simulation is carried out based on the assumption that all the layers deposited on the substrate adopts to the surface morphology of the substrate [45]. The absorbance spectra of a-SiO<sub>x</sub>:H solar cell obtained from the simulation is shown in Figure 7.2.

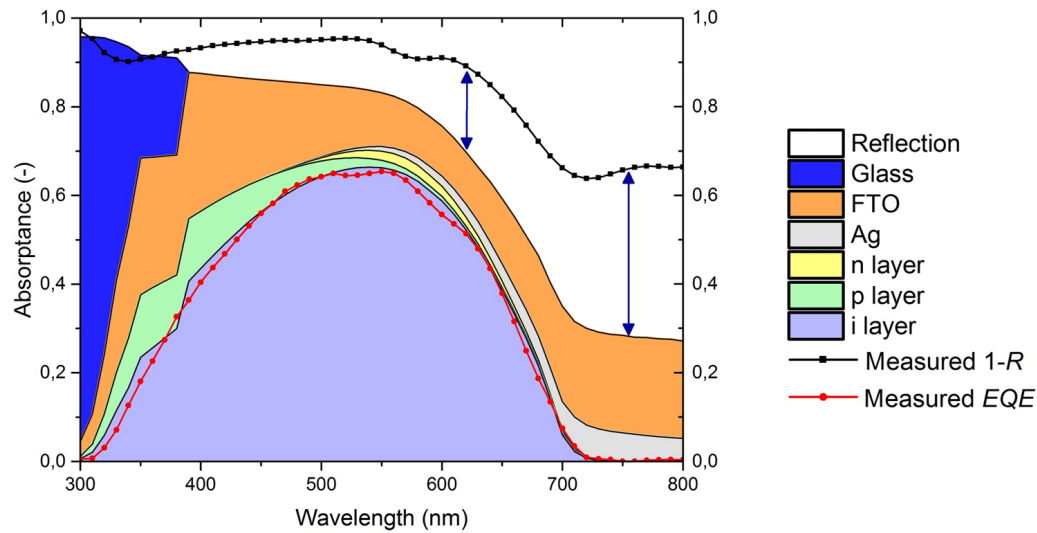


**Figure 7.2:** Absorption spectra of a-SiO<sub>x</sub>:H solar cell from GenPro4 simulations in comparison with the measured parameters. A 190-nm thick i-layer is used as input thickness to match the measured EQE of the solar cell.

The measured EQE and the simulated absorbance of the i-layer shows a good agreement. As represented by the double arrow, the simulation overestimates the reflectance and does not match with the measured reflectance. To troubleshoot this issue, all the layer's reflectance and transmittance were measured and the calculated absorbance of each layer was compared with the simulated absorption spectra. The Asahi substrate showed considerable mismatch as shown in Figure 7.3. The mismatch is mainly accounted for incorporation of a lower  $k$  value of FTO layer while simulating Asahi substrate. Various optical models were used to acquire  $n$  and  $k$  data of FTO layer, but the attempts were not successful. As a way forward, the solar cell stack is deposited on a flat Corning glass substrate with aluminium doped zinc oxide (AZO) as its front TCO and tin doped indium oxide (ITO) as its back TCO. The obtained solar cell stack is utilised for optical analysis.

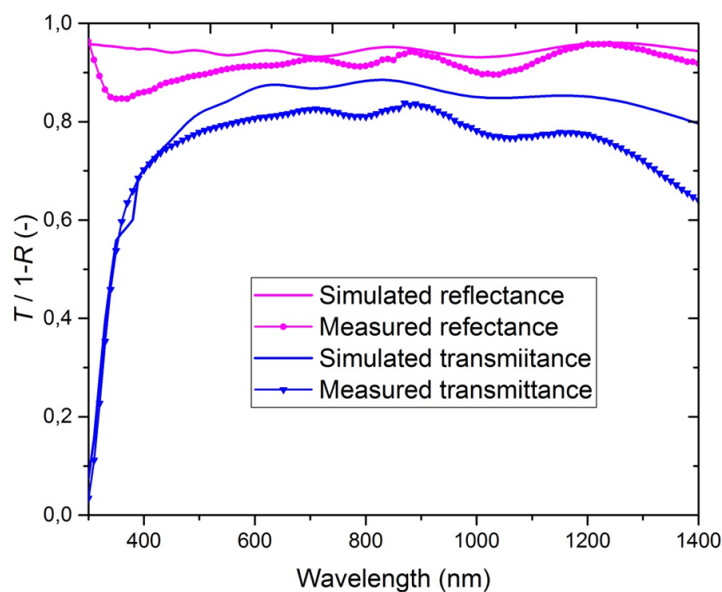


**Figure 7.3:** Comparison between simulated and measured reflectance and transmittance of Asahi substrate.

### 7.2.2. Optical simulation of top cell on a flat substrate

The solar cell stack as schematically shown in Figure 7.4 is simulated using GenPro4 and its optical behaviour is studied in this section. The solar cell is referred as Cell A.

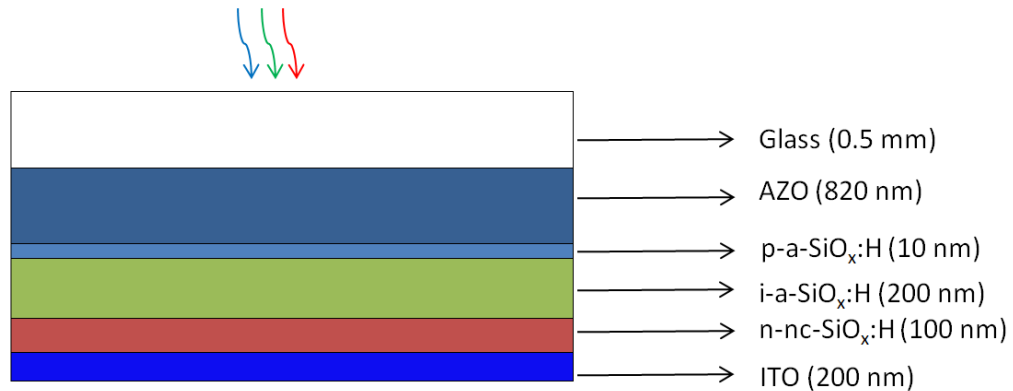


**Figure 7.4:** Schematic representation of Cell A on a flat glass substrate.

Figure 7.5 compares the measured and simulated reflectance and transmittance profile of Cell A. The simulated curve shows a decent agreement with the measured reflectance and transmittance. As mentioned earlier, the accuracy of the optical simulation depends on its input parameters. The shape and size of the interference fringes observed, depends on thickness of each and every layer in the solar cell stack. Even a slight deviation in the input thickness of the thin film layers, could possibly result in a shift in the interference fringes and can also alter its shape. The simulated curve also shows a lower reflectance than the measured value. This can be attributed to mismatch in the refractive index of any of the simulated layer to the actual layer in the solar cell stack. Nevertheless, the simulated and measured curve follow a similar pattern throughout the measured wavelength range. Hence, the simulation results of Cell A is considered as the frame of reference for carrying out optical analysis.

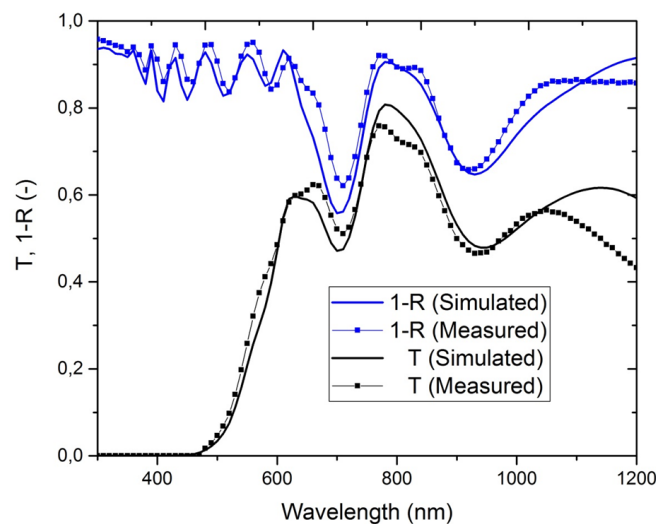


**Figure 7.5:** Comparison of simulated and measured reflectance and transmittance of a-SiO<sub>x</sub>:H solar cell on a flat glass substrate.

The main aim of this section is to maximise the sum of absorption in the i-layer and the transmittance through Cell A. These are the two deciding parameters which determine the photocurrent generation in the top and bottom cell of any 4TD configuration. The absorption spectra and relative distribution of  $J_A$  of Cell A is shown in Figure 7.6. Cell A absorbs 16%  $J_A$  in the i-layer and transmits 46%  $J_A$  of and thus utilises around 60% of  $J_A$  and the rest is lost in parasitic absorption and reflection losses.

The parasitic absorption losses can be classified into two parts. Firstly, the absorption in the glass carrier, p and n-layers of the solar cell stack resulting in a photocurrent absorption close to 6% of  $J_A$ . These layers are integral part of the current solar cell design and are not modified. Secondly, parasitic absorption in the transparent conductive oxide (TCO) layers account for absorption of 13% of  $J_A$ . AZO (Front TCO) absorbs around  $6 \text{ mA cm}^{-2}$  of  $J_A$  and contributes to most of the parasitic absorption in Cell A. As seen from the Figure 7.6- (A), the parasitic absorption in the TCOs, hinders the absorption in the i-layer in visible part of the spectrum and affects the transmittance of the solar cell in the infrared part of the spectrum. As the research objective of this section is to maximise the absorption in the i-layer and transmittance of the top cell, the TCO layer is considered for modification. It is noteworthy to mention that the current simulation is performed for a device with flat interfaces and that parasitic absorption due to the TCO would be further higher when using a textured substrate due to enhancement of light trapping in the solar cell stack [75].

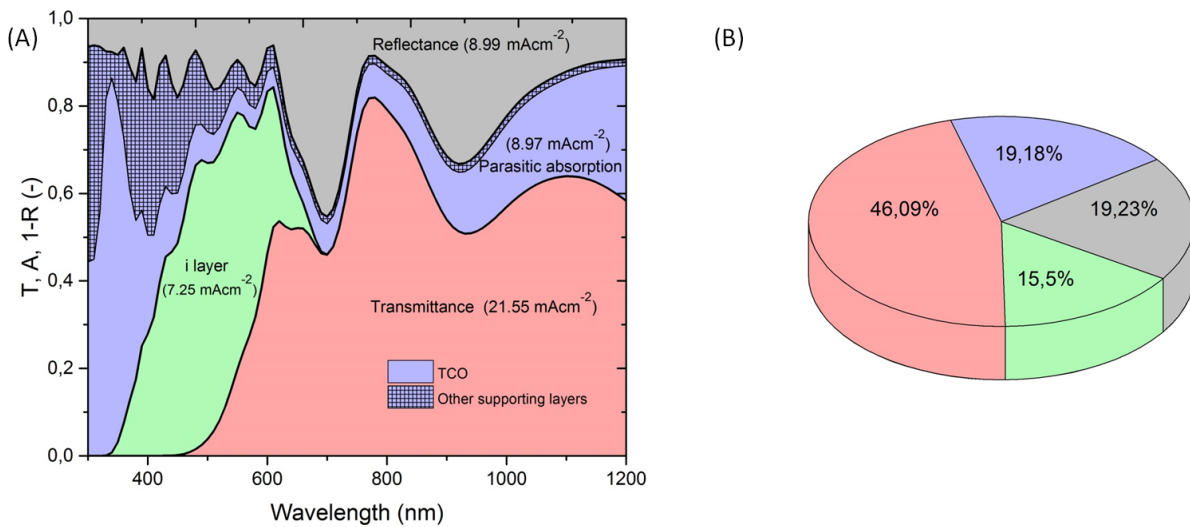


**Figure 7.6:** (A) optical response of cell A; and (B) relative distribution of  $J_A$  in Cell A.

In Cell A, the reflection loss accounts for 19% of  $J_A$ . The thin film solar cell is composed of layers with different refractive indices. Thus, leading to interfaces with contrasting refractive indices [76] and results in higher reflection. Moreover, the Cell A is simulated with a flat glass surface resulting in higher specular reflection. To reduce the reflection losses incurred in Cell A, several light management techniques are applied and examined in the subsequent section.

### 7.3. Reduction of parasitic absorption in the top cell

In a solar cell, the photo active semiconductor layers are placed between a TCO layer (front electrode) and the electric back contact [2]. The electric back contact is typically a metal surface with high reflection which helps in coupling of the non-absorbed photons back into the solar cell stack. The front TCO on the other hand, needs to be transparent so that most of the photons are passed to the active solar cell layers to facilitate photo generation. In a 4TD configuration, the top cell needs to have transparent electrode on both sides of the active semiconductor layers in order to facilitate absorption of photons in the bottom cell. Thus, it is of foremost importance that the TCOs used in a 4TD configurations are highly transparent in the spectral range of 4TD and does not contribute to parasitic absorption.

The electrical conductivity of a TCO can be mathematically defined by Equation 7.3 where  $N$  represents the free carrier concentration and  $\mu$  represents the carrier mobility. To have the required electrical conductivity, the TCOs need to have either high free carrier concentration or a high mobility or both. AZO and ITO are oxide layers doped with metal impurities [77]. The aluminium dopig in AZO and tin doping in ITO increase the free carrier density of these layers [64] resulting in higher electrical conductivity of these layers.

$$\sigma = e \cdot N \cdot \mu \quad (7.3)$$

The increase in free carrier density also increases the free carrier absorption and affects the transmission

of the TCO layer in infrared region [78]. Thus, a trade-off is established between the electrical and optical properties of these TCOs. To overcome this issue, TCOs with higher mobility can be considered. Hydrogenated indium oxide (IO:H) is one such TCO which has mobility in the range of 100 cm<sup>2</sup>/V s [79] and a good transparency in IR region. Figure 7.7 shows the comparison of  $k$  of AZO and IO:H. The lower  $k$  of IO:H in the infrared region is due to a lower free carrier absorption in the IO:H as compared to AZO.

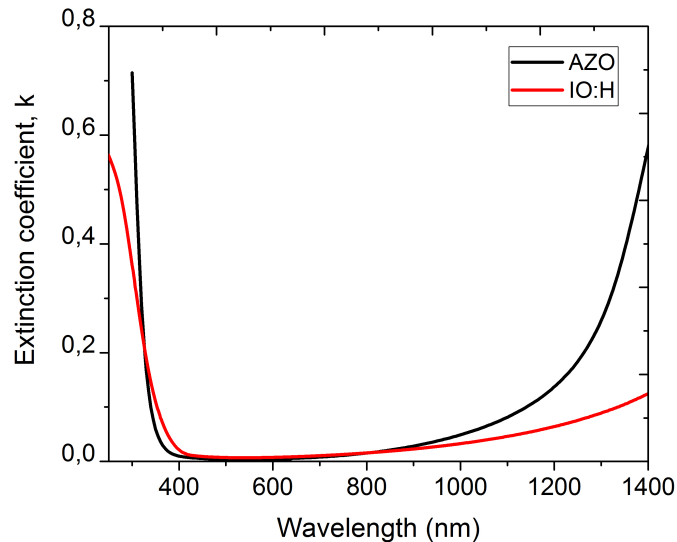


**Figure 7.7:** Extinction coefficient of AZO and IO:H.

Budhi et al. [80] of PVMD group fabricated IO:H layers with mobility of 150 cm<sup>2</sup>/V s at IO:H thickness of 200 nm. The optical constant of the layers fabricated by [80] are used in the simulations to predict the optical performance of Cell A using IO:H as its TCO.

The AZO and ITO layers of Cell A are replaced with 200 nm IO:H layers and are simulated in GenPro4. The schematic representation of the simulated solar cell is shown in Figure 7.8. The solar cell is referred as Cell B.

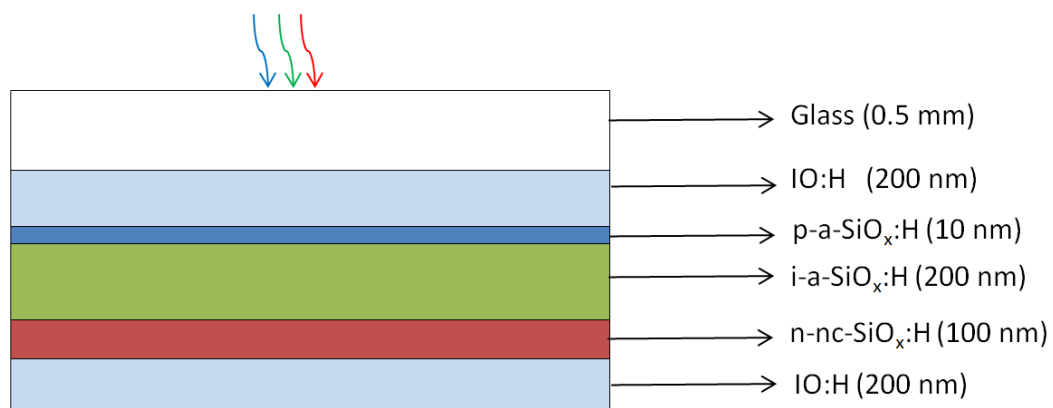


**Figure 7.8:** Schematic representation of Cell B.

Figure 7.9 shows the absorption spectra and relative distribution of  $J_A$  in Cell B. It is clear from Figure 7.9-(B) that the replacement of IO:H as TCO of the solar cell stack reduces the parasitic absorption from 19% to about 8%. As a result, the transmittance of the top cell is increased in IR region and the absorption of i-layer is increased in blue region. Cell B now has the possibility to utilise around 70% of the incident photons. But, the current solar cell stack's photon utilisation is limited due to the reflection losses.

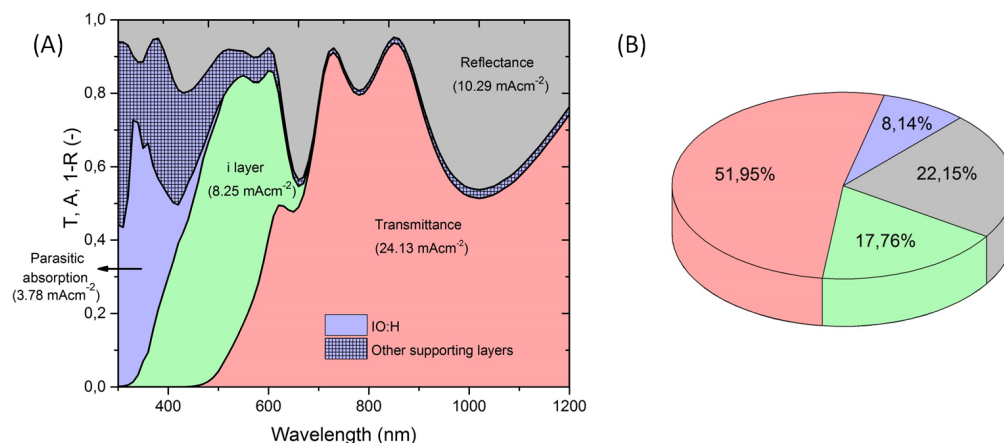


Figure 7.9: (A) optical response of Cell B; and (B) relative distribution of  $J_A$  in Cell B.

## 7.4. Reduction of reflection losses

An effective in-coupling of light at the air-glass interface of Cell A and Cell B can substantially reduce the reflection losses. In this section, two light trapping strategies are implemented and the simulated results are discussed.

### Implementation of surface texture on air-glass interface

Implementation of surface textures in the front side of the glass reduces the specular reflection at the flat glass interface and hence reduces the reflection losses [81]. The introduction of front texture implements an anti-reflection effect over a broader wavelength range and also facilitates light scattering [8]. A pyramidal surface texture with a feature size of micrometer is implemented on front side of the glass. These type of textures can be easily implemented in the glass substrate with the use of imprint lithography [82].

Effectiveness of light trapping depends on size, shape and periodicity of the surface texture adopted [83]. Further research can be carried out in this front to find a better surface texture for Cell A and Cell B. In this work, we limit our scope and simulate the front surface with the pyramidal texture.

### Implementation of surface texture on IO:H-p layer interface

Interfaces with contrasting refractive indices result in reflection. The internal interface of IO:H and p-layer interface is textured to reduce the extent of reflection by promoting a gradual change in the refractive indices [8]. Moreover, the introduction of surface texture in IO:H and p-layer interface aids scattering and increases the optical path of light resulting in enhanced light trapping in the absorber layer. Unlike the previous texture, a random texturing similar to one adopted in Asahi substrate is adopted in this simulation. A steep sharp surface texture on growth side of a thin film solar cell affects its  $V_{OC} \times FF$  product. Generally, the thin p and i-layer do not tend to grow well on the sharp interfaces of the textured substrate resulting in poor shunt resistance and increase in defects [84].

### Implementation of anti-reflection coating at the top and bottom of the solar cell stack

The reflection losses at the front side of the air-glass interface can be further reduced by the introduction of a anti-reflection coating (ARC). A film which has refractive index between air ( $n_a$ ) and glass ( $n_g$ ) when introduced in between the interface would reduce the extent of the reflection losses. The optimum value of refractive index of the film is calculated using Equation 7.4.

$$n_{opt} = \sqrt{n_a \cdot n_g} \quad (7.4)$$

The extend of reflection at a particular wavelength  $\lambda_0$  can be reduced by tweaking the thickness of ARC so as to facilitate destructive interference. The optimum thickness of ARC can be calculated using Equation 7.5.

$$d_{opt} = \frac{\lambda_0}{4n_{opt}} \quad (7.5)$$

MgF<sub>2</sub> with a refractive index of 1.38 is used as ARC in this simulation. Further, the thickness of i-layer and the ARC coatings are varied to maximise the sum of photocurrent absorption in i layer and in the transmitted spectrum to the bottom cell. The schematics of the simulated top cell is shown in Figure 7.10 and is referred as Cell C.

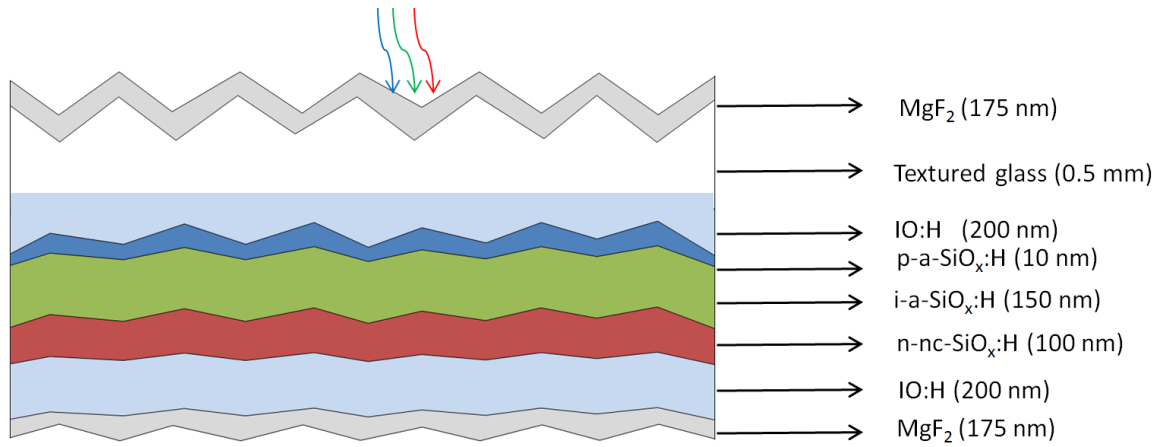


**Figure 7.10:** Schematic representation of Cell C.

Figure 7.11 shows the absorption spectra and relative distribution of  $J_A$  in Cell C. The Cell C stack shows about 80% utilisation of  $J_A$ . The parasitic absorption is slightly higher in Cell C than in Cell B due to the surface texture of the solar cell. The trapped light inside the solar cell stack gets absorbed in the supporting layers and contributes to a small increase in parasitic absorption. The reflection loss is reduced from 22% to about 11%. It is possible to reduce the reflection losses further by refractive index grading at top and bottom interface of the solar cell and also by introduction of distributed bragg reflector.

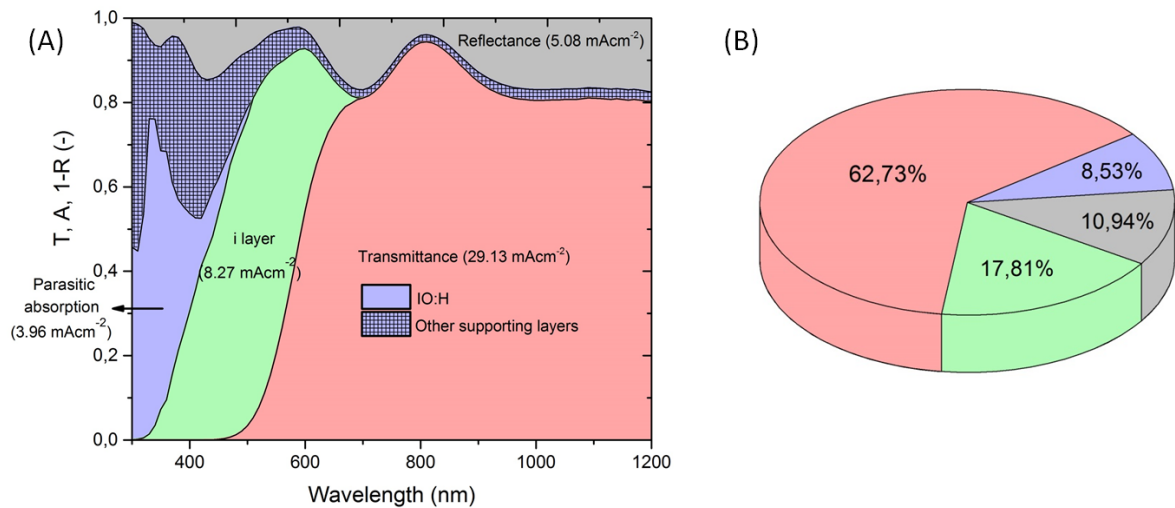


**Figure 7.11:** (A) optical response of Cell C; and (B) relative distribution of  $J_A$  in Cell C.

The solar cell stack with design specification of Cell C can be considered as the top cell structure to maximise the utilisation of  $J_A$  so as to maximise the efficiency gain in a 4TD configuration using a-SiO<sub>x</sub>:H solar cell as top cell.

## 7.5. Efficiency potential of a-SiO<sub>x</sub>:H solar cell as top cell

The simulated wavelength dependent transmittance and i-layer absorption of Cell C are utilised in this section to determine the efficiency gain of the optimised top cell. The electrical parameters of best performing CIGS solar cell from Solliance and  $V_{OC}$  and FF of a-SiO<sub>x</sub>:H solar cell fabricated by Kim et. al.[34] are used in this section and are tabulated in Table 7.1. The EQE of the bottom cell is determined using the method explained in Section 3.3 of Chapter 3. Figure 7.12 shows the simulated EQE and reflectance of the 4TD along with the transmittance of the top cell. The higher transmittance of the top cell enhances the EQE of the bottom cell and results in an efficiency gain of 0.75%, as shown in Table 7.2. It is interesting to note that parasitic absorption in the bottom cell (area between the transmittance of the top cell and EQE of 4TD) now limits the efficiency gain in the 4TD configuration. Nevertheless, Cell C possesses a combination of excellent spectral response in the shorter wavelength region and a good transparency in the IR region, thus making it more suitable for high efficiency 4TD configuration.

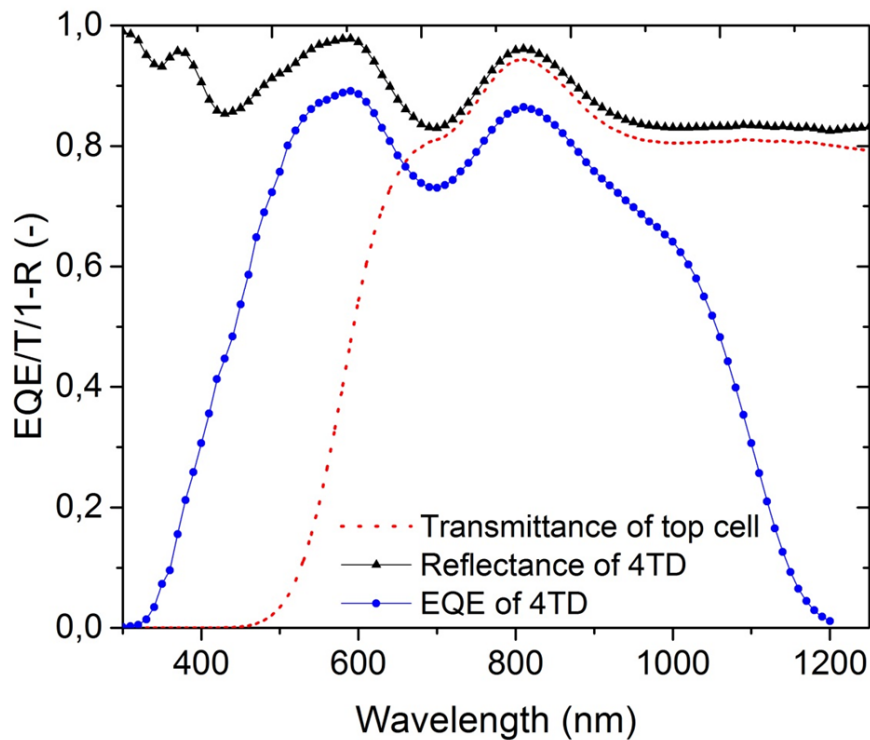


**Figure 7.12:** Simulated EQE of the 4TD using Cell C as the top cell.

**Table 7.1:** Electrical parameters of cells used in the efficiency estimation.

S.No	Solar cell	$J_{SC}$ (mA/cm <sup>2</sup> )	$V_{OC}$ (V)	Fill factor (FF)	$V_{OC} \times FF$ (V)	Efficiency (%)
1	a-SiO <sub>x</sub> :H [34]	08.27	1.04	0.73	0.76	6.29
2	CIGS-Solliance	34.50	0.64	0.71	0.46	15.80

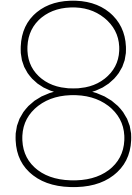
**Table 7.2:** Theoretical 4TD efficiency for Cell C and CIGS configuration.

S.NO	Bottom cell	$\eta$ (%)	$\eta_{Bot}$ (%)	$\eta_{Top}$ (%)	$\eta_{4TD}$ (%)	$\eta_{gain}$ (%)
1	CIGS-Solliance	15.80	10.26	6.29	16.55	0.75

## 7.6. Conclusion

Based on the results shown in this chapter, we can come to the following conclusions:

- The transmittance of the current top cell limits the efficiency gain in the 4TD. Only 60% of the available photocurrent is utilised by the 4TD. The optical analysis revealed that the TCO contributes to major parasitic absorption losses owing to their free carrier absorption.
- from simulation work it is concluded that, by adopting a double textured IO:H substrate coated with ARC an increase in photocurrent utilisation of the 4TD from 60% to 80% can be obtained.
- Excellent spectral response in the shorter wavelength and a good transparency in the IR region makes Cell C an interesting candidate as a top cell for high efficiency 4TD's.



# Conclusions and Recommendations

## 8.1. Conclusions

The main goal of this work was to investigate the potential of a-SiO<sub>x</sub>:H as the top cell in a four terminal device (4TD) configuration. To accomplish this goal, a theoretical model (TM) for estimating the efficiency of a 4TD configuration was derived. Using the TM, the efficiency of the 4TD with an a-SiO<sub>x</sub>:H top cell resulted in a gain in efficiency of 2.3% and 3.4% for CIGS ( $\eta_{SA} = 10.08\%$ ) and CIS ( $\eta_{SA} = 06.40\%$ ) solar cells respectively. This motivated us to fabricate the 4TD devices with an a-SiO<sub>x</sub>:H top cell and CIGS/CIS bottom cell.

To obtain the most suitable top cell for this 4TD application, the a-SiO<sub>x</sub>:H ( $E_g$ -2.03 eV) solar cells with varying i-layer thicknesses were fabricated on a textured Asahi and a flat AZO substrate and were analysed based on several figures of merit such as EQE,  $V_{OC} \times FF$  product and transmission. The solar cells on the Asahi substrate had a high  $J_{SC}$  at the cost of their  $V_{OC} \times FF$  product and transmission. On the other hand, the solar cells on AZO had the highest  $V_{OC} \times FF$  product and transmission but a low current generation. The TM analysis with these solar cells revealed that the extent of efficiency gain in the bottom cell was mainly dictated by the  $J_{SC}$  of the top cell. Given the fact that the bandgap of the absorber layer affects  $J_{SC}$ , a-SiO<sub>x</sub>:H cells having a bandgap of 1.96 eV were fabricated. As a result, the a-SiO<sub>x</sub>:H ( $E_g$ -1.96 eV) solar cell resulted in a current gain of  $2 \text{ mA cm}^{-2}$ . Subsequently, a-SiO<sub>x</sub>:H top cells with two different bandgaps (2.03 eV and 1.96 eV) were fabricated in a combination with CIGS and CIS bottom cells to estimate their effect of on a real 4TD device.

Four different 4TD configurations were fabricated in this work. All the 4TD devices resulted in a gain in efficiency with respect to the stand-alone efficiency of the bottom cell.. The performance analysis of different combinations of 4TD's revealed that the extent of efficiency gain in the bottom cell is higher for a low performing bottom cell. The combination of a-SiO<sub>x</sub>:H ( $E_g$ -1.96 eV) with CIS solar cell resulted in a maximum gain of 4.40%. The higher magnitude of efficiency gain in these devices can be attributed to a higher difference in  $V_{OC} \times FF$  product between the top and bottom cell.

Currently, the low transmission of the top cell affects the performance of the bottom cell which further limits the efficiency gain of the bottom cell in the 4TD. The parasitic absorption in the TCO layers and the reflection losses affect the transmission of the top cell. To investigate such optical losses in the 4TD, an analysis was carried out using the optical simulation tool GenPro4. From simulations, the parasitic and reflection losses in the optical system were reduced by replacing the Asahi substrate with the incorporation of a double textured IO:H substrate with an ARC. As a result, the optimised 4TD configuration now achieves a photocurrent utilisation of 80%, which explains the true potential of the a-SiO<sub>x</sub>:H based 4TD configuration.

## 8.2. Recommendations

The following recommendations can be applied for future works on the 4TD configuration.

- Textured IO:H substrate for the top cells needs to be fabricated, which can enhance the light trapping at the top and as well as have a high transparency in the IR region. A pyramidal front texture with ARC coating can later be implemented on the IO:H cells to further enhance the light trapping in the top cell.
- Fabrication of a double mirror distributed Bragg reflector (DBR) which can ideally reflect wavelength

ranging between 300 to 750 nm to the top cell and transmit the rest to the bottom cell can be investigated.

- Owing to its wider spectral range, a-Si:H can be an excellent candidate as a top cell in the 4TD configuration. Research work to enhance its  $V_{OC} \times FF$  product needs to be carried out. Moreover, a thicker i-layer can be adopted with a-Si:H as the drop in  $V_{OC} \times FF$  product is limited.
- The a-SiO<sub>x</sub>:H (1.96 eV) and a-SiO<sub>x</sub>:H (2.03 eV) solar cells need to be further investigated with a p-nc-SiO<sub>x</sub>:H layer to reduce their parasitic absorption in the shorter wavelength region.
- The a-SiO<sub>x</sub>:H solar cell with 8.80% efficiency fabricated by Kim. et al. [57] can be utilised as the top cell due to their better spectral response compared to the a-SiO<sub>x</sub>:H solar cell with high the  $V_{OC} \times FF$  product.
- The prediction of  $V_{OC} \times FF$  product of the bottom cell at different light intensities can be solved from their diode equation. The diode parameters of various solar cells need to be archived to have a database on the choice of bottom cells.
- Efficiency determination of the bottom cells using a long-pass optical filter (700 nm wavelength range) can give an idea of the maximum possible bottom cell efficiency in a 4TD configuration. This can help with the choice of the bottom cell in a 4TD configuration.
- Due to the complex methodology adopted in taking out the external contact from the top and bottom cells, the number of sample spot for efficiency analysis is limited. A more sophisticated 4TD device fabrication with a thin layer of printed circuit board (PCB) pasted adjacent to the active area of the solar cell needs to be adopted to take out external wiring from the cells.

# Bibliography

- [1] *World Energy Resources Full Report 2016*, World Energy Council, 2016.
- [2] O. Isabella, A. Smets, K. Jäger, M. Zeman, and R. van Swaaij, "Solar energy: The physics and engineering of photovoltaic conversion, technologies and systems," *UIT Cambridge Limited*, 2016.
- [3] G. E. Eperon, M. T. Hörantner, and H. J. Snaith, "Metal halide perovskite tandem and multiple-junction photovoltaics," *Nature Reviews Chemistry*, vol. 1, no. 12, p. 0095, 2017.
- [4] M. Filipič, P. Löper, B. Niesen, S. De Wolf, J. Krč, C. Ballif, and M. Topič, "Ch<sub>3</sub>NH<sub>3</sub>PbI<sub>3</sub> perovskite/silicon tandem solar cells: characterization based optical simulations," *Optics express*, vol. 23, no. 7, pp. A263–A278, 2015.
- [5] T.C.Loef, "Periodic-random modulated surface textures for efficient light trapping in thin-film 55 solar cells," Master's Thesis, Delft University of Technology, Delft, Netherlands, 2018.
- [6] G. Yang, "High-efficient nip thin-film silicon solar cells," PhD thesis, Delft University of Technology, Delft, Netherlands, 2015.
- [7] Wikipedia. Spectroscopic ellipsometry. [Online]. Available: [https://upload.wikimedia.org/wikipedia/commons/2/27/Ellipsometry\\_setup.svg](https://upload.wikimedia.org/wikipedia/commons/2/27/Ellipsometry_setup.svg), [Accessed:16-Oct-2018]
- [8] O. Isabella, "Light management in thin-film silicon solar cells. phd thesis, delft university of technology," PhD thesis, Delft University of Technology, Delft, Netherlands, 2013.
- [9] V. Raman, "Development of bandgap graded (a-si<sub>x</sub>:h) solar cells for two-terminal and four terminal applications," Master's thesis, Delft University of Technology, 2018.
- [10] A. Parisi, R. Pernice, V. Rocca, L. Curcio, S. Stivala, A. C. Cino, G. Cipriani, V. Di Dio, G. Ricco Galluzzo, R. Miceli *et al.*, "Graded carrier concentration absorber profile for high efficiency cigs solar cells," *International Journal of Photoenergy*, vol. 2015, 2015.
- [11] A. H. M. Smets, *Growth related material properties of hydrogenated amorphous silicon*. Technische Universiteit Eindhoven, 2002.
- [12] E. Guijt, "Application of intrinsic amorphous silicon oxide in multi-junction solar cells," Master's thesis, Delft University of Technology, 2014.
- [13] T. A. Boden, R. J. Andres, and G. Marland, "Global, regional, and national fossil-fuel co<sub>2</sub> emissions (1751-2010)(v. 2013)," Carbon Dioxide Information Analysis Center (CDIAC), Oak Ridge National Laboratory (ORNL), Oak Ridge, TN (United States), Tech. Rep., 2013.
- [14] *World Population Prospects: The 2016 Revision, Key Findings and Advance Tables*, United Nations Department of Economic and Social Affairs/Population Division UN DESA, 2016.
- [15] *International Energy Outlook 2017*, U.S Energy Information Administration, 2018.
- [16] M. Höök and X. Tang, "Depletion of fossil fuels and anthropogenic climate change—a review," *Energy Policy*, vol. 52, pp. 797–809, 2013.
- [17] S. Shafiee and E. Topal, "When will fossil fuel reserves be diminished?" *Energy policy*, vol. 37, no. 1, pp. 181–189, 2009.
- [18] J. F. Kasting, "The carbon cycle, climate, and the long-term effects of fossil fuel burning," *Consequences*, vol. 4, no. 1, pp. 15–27, 1998.

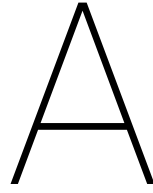
- [19] S. Solomon, D. Qin, M. Manning, Z. Chen, M. Marquis, K. B. Averyt, M. Tignor, H. L. Miller *et al.*, "Contribution of working group i to the fourth assessment report of the intergovernmental panel on climate change, 2007," 2007.
- [20] G. Boyle, "Renewable energy," *Renewable Energy*, by Edited by Godfrey Boyle, pp. 456. Oxford University Press, May 2004. ISBN-10: 0199261784. ISBN-13: 9780199261789, p. 456, 2004.
- [21] K. Branker, M. Pathak, and J. M. Pearce, "A review of solar photovoltaic levelized cost of electricity," *Renewable and sustainable energy reviews*, vol. 15, no. 9, pp. 4470–4482, 2011.
- [22] W. Shockley and H. J. Queisser, "Detailed balance limit of efficiency of p-n junction solar cells," *Journal of applied physics*, vol. 32, no. 3, pp. 510–519, 1961.
- [23] A. Richter, M. Hermle, and S. W. Glunz, "Reassessment of the limiting efficiency for crystalline silicon solar cells," *IEEE journal of photovoltaics*, vol. 3, no. 4, pp. 1184–1191, 2013.
- [24] J. Parrott, "The limiting efficiency of an edge-illuminated multigap solar cell," *Journal of Physics D: Applied Physics*, vol. 12, no. 3, p. 441, 1979.
- [25] S. Bremner, M. Levy, and C. B. Honsberg, "Analysis of tandem solar cell efficiencies under am1.5g spectrum using a rapid flux calculation method," *Progress in photovoltaics: Research and Applications*, vol. 16, no. 3, pp. 225–233, 2008.
- [26] K. A. Bush, A. F. Palmstrom, J. Y. Zhengshan, M. Boccard, R. Cheacharoen, J. P. Mailoa, D. P. McMeekin, R. L. Hoye, C. D. Bailie, T. Leijtens *et al.*, "23.6%-efficient monolithic perovskite/silicon tandem solar cells with improved stability," *Nature Energy*, vol. 2, no. 4, p. 17009, 2017.
- [27] S. De Wolf, J. Holovsky, S.-J. Moon, P. Loper, B. Niesen, M. Ledinsky, F.-J. Haug, J.-H. Yum, and C. Ballif, "Organometallic halide perovskites: sharp optical absorption edge and its relation to photovoltaic performance," *The journal of physical chemistry letters*, vol. 5, no. 6, pp. 1035–1039, 2014.
- [28] M. Jaysankar, W. Qiu, M. van Eerden, T. Aernouts, R. Gehlhaar, M. Debucquoy, U. W. Paetzold, and J. Poortmans, "Four-terminal perovskite/silicon multijunction solar modules," *Advanced Energy Materials*, vol. 7, no. 15, p. 1602807, 2017.
- [29] M. H. Futscher and B. Ehrler, "Efficiency limit of perovskite/si tandem solar cells," *ACS Energy Letters*, vol. 1, no. 4, pp. 863–868, 2016.
- [30] S. Essig, J. F. Geisz, M. A. Steiner, A. Merkle, R. Peibst, J. Schmidt, R. Brendel, S. Ward, D. J. Friedman, P. Stradins *et al.*, "Development of highly-efficient gainp/si tandem solar cells," in *Photovoltaic Specialist Conference (PVSC), 2015 IEEE 42nd*. IEEE, 2015, pp. 1–4.
- [31] S. Essig, S. Ward, M. A. Steiner, D. J. Friedman, J. F. Geisz, P. Stradins, and D. L. Young, "Progress towards a 30% efficient gainp/si tandem solar cell," *Energy Procedia*, vol. 77, pp. 464–469, 2015.
- [32] J. Werner, L. Barraud, A. Walter, M. Brauningner, F. Sahli, D. Sacchetto, N. Tetreault, B. Paviet-Salomon, S.-J. Moon, C. Allebe *et al.*, "Efficient near-infrared-transparent perovskite solar cells enabling direct comparison of 4-terminal and monolithic perovskite/silicon tandem cells," *ACS Energy Letters*, vol. 1, no. 2, pp. 474–480, 2016.
- [33] A. Chaudhary, "Development of four-terminal mechanically-stacked solar cells utilising hydrogenated amorphous silicon oxide (a-sio<sub>x</sub>:h) and crystalline silicon cells," Master's thesis, Delft University of Technology, 2017.
- [34] D. Y. Kim, E. Guijt, R. A. van Swaaij, and M. Zeman, "Development of a-sio<sub>x</sub>: H solar cells with very high voc × ff product," *Progress in Photovoltaics: Research and Applications*, vol. 23, no. 6, pp. 671–684, 2015.
- [35] A. Solar. Vu (tco) - agc solar. [Online]. Available: [http://www.agc-solar.com/glass-products/coated-glass/tco/tco-vu.html#uid\\_11\\_down](http://www.agc-solar.com/glass-products/coated-glass/tco/tco-vu.html#uid_11_down).
- [36] S. Awad and R. Nagarajan, "Ultrasonic cleaning," in *Developments in Surface Contamination and Cleaning: Particle Deposition, Control and Removal*. Elsevier, 2010, pp. 225–280.

- [37] Elettrovava. Pecvd deposition systems - elettrovava. [Online]. Available: <http://www.elettrovava.com/en/pecvd-deposition-systems.html>. [Accessed:16-Oct-2018]
- [38] D. M. Mattox, *Handbook of physical vapor deposition (PVD) processing*. William Andrew, 2010.
- [39] M. Losurdo, M. Giangregorio, P. Capezzuto, G. Bruno, R. De Rosa, F. Roca, C. Summonte, J. Pla, and R. Rizzoli, "Parametrization of optical properties of indium–tin–oxide thin films by spectroscopic ellipsometry: Substrate interfacial reactivity," *Journal of Vacuum Science & Technology A: Vacuum, Surfaces, and Films*, vol. 20, no. 1, pp. 37–42, 2002.
- [40] *M-2000 Specifications*, J.A.Woolam Co., Inc. [Online]. Available: [https://www.moles.washington.edu/wordpress/wp-content/uploads/2015/03/Woolam\\_Ellipsometer\\_Specs.pdf](https://www.moles.washington.edu/wordpress/wp-content/uploads/2015/03/Woolam_Ellipsometer_Specs.pdf). Accessed:16/10/2018.
- [41] T. de Vrijer, "Stability and performance of doped silicon oxide layers for use in thin film silicon solar cells," Master's thesis, Delft University of Technology, 2015.
- [42] R.Vismara, "Optical characterization of photovoltaic materials and structures for thin-film solarcells based on advanced texturization," Master's thesis, Delft University of Technology, 2014.
- [43] *Wacom Electric Co., Ltd.*, Solar simualtor. [Online]. Available: Retrievedfrom:<http://www.wacom-ele.co.jp/en/products/solar/normal/>. Accessed:16/10/2018.
- [44] J.-W. Lee, D.-J. Seol, A.-N. Cho, and N.-G. Park, "High-efficiency perovskite solar cells based on the black polymorph of  $\text{hc}(\text{nh}_2)_2\text{pb}_3\text{i}_3$ ," *Advanced materials*, vol. 26, no. 29, pp. 4991–4998, 2014.
- [45] R. Santbergen, T. Meguro, T. Suezaki, G. Koizumi, K. Yamamoto, and M. Zeman, "Genpro4 optical model for solar cell simulation and its application to multijunction solar cells," *IEEE Journal of Photovoltaics*, vol. 7, no. 3, pp. 919–926, 2017.
- [46] M. Chegaar, A. Hamzaoui, A. Namoda, P. Petit, M. Aillerie, and A. Herguth, "Effect of illumination intensity on solar cells parameters," *Energy Procedia*, vol. 36, pp. 722–729, 2013.
- [47] "Mounted absorptive neutral density filters," [https://www.thorlabs.com/newgrouppage9.cfm?objectgroup\\_id=266](https://www.thorlabs.com/newgrouppage9.cfm?objectgroup_id=266), October 2018, (Accessed on 10/22/2018).
- [48] P. Capezzuto and A. Madan, *Plasma deposition of amorphous silicon-based materials*. Elsevier, 1995.
- [49] W. Kessels, *Remote plasma deposition of hydrogenated amorphous silicon : plasma processes, film growth, and material properties*. Technische Universiteit Eindhoven, 2000.
- [50] M. Zhi-Xun, L. Xian-Bo, K. Guang-Lin, and C. Jun-Hao, "Microstructure of siox: H films prepared by plasma enhanced chemical vapor deposition," *Chinese Physics*, vol. 9, no. 4, p. 309, 2000.
- [51] M. Konagai, "Status of amorphous silicon and related alloys prepared by photochemical vapor deposition," *MRS Online Proceedings Library Archive*, vol. 70, 1986.
- [52] P. Babal, J. Blanker, R. Vasudevan, A. Smets, and M. Zeman, "Microstructure analysis of n-doped  $\mu\text{-sio}_x\text{:H}$  reflector layers and their implementation in stable a-si: H pin junctions," in *Photovoltaic Specialists Conference (PVSC), 2012 38th IEEE*. IEEE, 2012, pp. 000 321–000 326.
- [53] P. Cuony, D. T. Alexander, I. Perez-Wurfl, M. Despeisse, G. Bugnon, M. Boccard, T. Söderström, A. Hessler-Wyser, C. Hébert, and C. Ballif, "Silicon filaments in silicon oxide for next-generation photovoltaics," *Advanced Materials*, vol. 24, no. 9, pp. 1182–1186, 2012.
- [54] S. Iftiqar, "The roles of deposition pressure and rf power in opto-electronic properties of a-sio: H films," *Journal of Physics D: Applied Physics*, vol. 31, no. 14, p. 1630, 1998.
- [55] T.-T. Li, T. Yang, J. Fang, D.-K. Zhang, J. Sun, C.-C. Wei, S.-Z. Xu, G.-C. Wang, C.-C. Liu, Y. Zhao *et al.*, "Microstructure and lateral conductivity control of hydrogenated nanocrystalline silicon oxide and its application in a-si: H/a-sige: H tandem solar cells," *Chinese Physics B*, vol. 25, no. 4, p. 046101, 2016.
- [56] A. Čampa, M. Meier, M. Boccard, L. Mercaldo, M. Ghosh, C. Zhang, T. Merdzhanova, J. Krč, F.-J. Haug, and M. Topič, "Micromorph silicon solar cell optical performance: Influence of intermediate reflector and front electrode surface texture," *Solar Energy Materials and Solar Cells*, vol. 130, pp. 401–409, 2014.

- [57] D. Y. Kim, E. Guijt, R. A. van Swaaij, and M. Zeman, "Hydrogenated amorphous silicon oxide (a-sio<sub>x</sub>:H) single junction solar cell with 8.8% initial efficiency by reducing parasitic absorptions," *Journal of Applied Physics*, vol. 121, no. 13, p. 133103, 2017.
- [58] A. Limmanee, J. Sritharathikhun, T. Krajangsang, K. Sriprapha, A. Hongsingthong, and S. Inthisang, "Wide-gap p- $\mu$  c-si 1-x o x: H films and their application to amorphous silicon solar cells," *International Journal of Photoenergy*, vol. 2013, 2013.
- [59] Y. Naruse, M. Matsumoto, T. Sekimoto, M. Hishida, Y. Aya, W. Shinohara, A. Fukushima, S. Yata, A. Terakawa, M. Iseki *et al.*, "Identification of defective regions in thin-film si solar cells for new-generation energy devices," in *Photovoltaic Specialists Conference (PVSC), 2012 38th IEEE*. IEEE, 2012, pp. 003 118–003 123.
- [60] G. Yang, R. A. van Swaaij, H. Tan, O. Isabella, and M. Zeman, "Modulated surface textured glass as substrate for high efficiency microcrystalline silicon solar cells," *Solar Energy Materials and Solar Cells*, vol. 133, pp. 156–162, 2015.
- [61] L. Meng and S. Miyajima, "Optically-rough and physically-flat tco substrates for superstrate-type thin-film solar cells: sol-gel zn1-xmgxo coating on nanoimprint patterned glass substrates," *Solar Energy Materials and Solar Cells*, vol. 161, pp. 38–45, 2017.
- [62] K. Tabuchi, W. W. Wenas, A. Yamada, M. Konagai, and K. Takahashi, "Optimization of zno films for amorphous silicon solar cells," *Japanese journal of applied physics*, vol. 32, no. 9R, p. 3764, 1993.
- [63] A. Hongsingthong, H. Wada, Y. Moriya, P. Sichanugrist, and M. Konagai, "Development of boron-doped zno films with novel thin zn-rich film and their application to solar cells," *Japanese Journal of Applied Physics*, vol. 51, no. 10S, p. 10NB03, 2012.
- [64] D. Mattox and V. Mattox, "Review of transparent conductive oxides (tco)," in *Society of Vacuum Coaters*, 2007.
- [65] M. Llusçà, J. D. Santos, S. Fernández, J. P. González, J. J. Gandía, J. Cárabe, A. Antony, J. M. Asensi, J. Bertomeu *et al.*, "Textured glass substrates for thin film silicon solar cells," in *28th Eur. Photovolt. Sol. Energy Conf. Exhib*, 2012, pp. 2170–2174.
- [66] P. Jackson, D. Hariskos, E. Lotter, S. Paetel, R. Wuerz, R. Menner, W. Wischmann, and M. Powalla, "New world record efficiency for cu (in, ga) se<sub>2</sub> thin-film solar cells beyond 20%," *Progress in Photovoltaics: Research and Applications*, vol. 19, no. 7, pp. 894–897, 2011.
- [67] D. Y. Kim, E. Guijt, F. T. Si, R. Santbergen, J. Holovský, O. Isabella, R. A. van Swaaij, and M. Zeman, "Fabrication of double-and triple-junction solar cells with hydrogenated amorphous silicon oxide (a-siox: H) top cell," *Solar Energy Materials and Solar Cells*, vol. 141, pp. 148–153, 2015.
- [68] D. Zhang, M. Najafi, V. Zardetto, M. Dörenkämper, X. Zhou, S. Veenstra, L. Geerligs, T. Aernouts, and R. Andriessen, "High efficiency 4-terminal perovskite/c-si tandem cells," *Solar Energy Materials and Solar Cells*, vol. 188, pp. 1–5, 2018.
- [69] T. Minami, H. Nanto, and S. Takata, "Highly conductive and transparent aluminum doped zinc oxide thin films prepared by rf magnetron sputtering," *Japanese Journal of Applied Physics*, vol. 23, no. 5A, p. L280, 1984.
- [70] W. Qarony, M. I. Hossain, M. K. Hossain, M. J. Uddin, A. Haque, A. Saad, and Y. H. Tsang, "Efficient amorphous silicon solar cells: characterization, optimization, and optical loss analysis," *Results in physics*, vol. 7, pp. 4287–4293, 2017.
- [71] P. Grunow, S. Lust, D. Sauter, V. Hoffmann, C. Beneking, B. Litzenburger, and L. Podlowski, "Weak light performance and annual yields of pv modules and systems as a result of the basic parameter set of industrial solar cells," in *19th European Photovoltaic Solar Energy Conference*, 2004, pp. 2190–2193.
- [72] C. Frisk, C. Platzer-Björkman, J. Olsson, P. Szaniawski, J. Wätjen, V. Fjällström, P. Salomé, and M. Edoff, "Optimizing ga-profiles for highly efficient cu (in, ga) se<sub>2</sub> thin film solar cells in simple and complex defect models," *Journal of Physics D: Applied Physics*, vol. 47, no. 48, p. 485104, 2014.

- [73] H. Elanzeery, F. Babbe, M. Melchiorre, F. Werner, and S. Siebentritt, "High-performance low bandgap thin film solar cells for tandem applications," *Progress in Photovoltaics: Research and Applications*, 2018.
- [74] K. Jäger, M. Fischer, R. Van Swaaij, and M. Zeman, "A scattering model for nano-textured interfaces and its application in opto-electrical simulations of thin-film silicon solar cells," *Journal of Applied Physics*, vol. 111, no. 8, p. 083108, 2012.
- [75] A. Feltrin, T. Meguro, M. Ichikawa, F. Sezaki, and K. Yamamoto, "Light scattering and parasitic absorption in thin film silicon solar cells containing metal nanoparticles," *Journal of Photonics for Energy*, vol. 1, no. 1, p. 017003, 2011.
- [76] D. Zhang, W. Soppe, and R. E. Schropp, "Design of 4-terminal solar modules combining thin-film wide-bandgap top cells and c-si bottom cells," *Energy Procedia*, vol. 77, pp. 500–507, 2015.
- [77] A. Klein, C. Körber, A. Wachau, F. Säuberlich, Y. Gassenbauer, S. P. Harvey, D. E. Proffit, and T. O. Mason, "Transparent conducting oxides for photovoltaics: Manipulation of fermi level, work function and energy band alignment," *Materials*, vol. 3, no. 11, pp. 4892–4914, 2010.
- [78] H. Zheng, R.-J. Zhang, D.-H. Li, X. Chen, S.-Y. Wang, Y.-X. Zheng, M.-J. Li, Z.-G. Hu, N. Dai, and L.-Y. Chen, "Optical properties of al-doped zno films in the infrared region and their absorption applications," *Nanoscale research letters*, vol. 13, no. 1, p. 149, 2018.
- [79] T. Koida, H. Fujiwara, and M. Kondo, "Hydrogen-doped  $\text{In}_2\text{O}_3$  as high-mobility transparent conductive oxide," *Japanese Journal of Applied Physics*, vol. 46, no. 7L, p. L685, 2007.
- [80] A. W. S. Budhi, "Hydrogenated indium oxide (io:h) for thin film solar cell," Master's thesis, Delft University of Technology, 2016.
- [81] J. Müller, B. Rech, J. Springer, and M. Vanecek, "Tco and light trapping in silicon thin film solar cells," *Solar energy*, vol. 77, no. 6, pp. 917–930, 2004.
- [82] C. Battaglia, J. Escarré, K. Soderstrom, L. Erni, L. Ding, G. Bugnon, A. Billet, M. Boccard, L. Barraud, S. De Wolf *et al.*, "Nanoimprint lithography for high-efficiency thin-film silicon solar cells," *Nano letters*, vol. 11, no. 2, pp. 661–665, 2010.
- [83] R. Dewan, I. Vasilev, V. Jovanov, and D. Knipp, "Optical enhancement and losses of pyramid textured thin-film silicon solar cells," *Journal of Applied Physics*, vol. 110, no. 1, p. 013101, 2011.
- [84] C.-M. Hsu, C. Battaglia, C. Pahud, Z. Ruan, F.-J. Haug, S. Fan, C. Ballif, and Y. Cui, "High-efficiency amorphous silicon solar cell on a periodic nanocone back reflector," *Advanced Energy Materials*, vol. 2, no. 6, pp. 628–633, 2012.





## Appendix A

In this work, the variation of  $V_{OC} \times FF$  product of the bottom cell at different light intensity was performed with the help of optical density (OD) filters. Optical density (OD) filters used in this work are listed in Table A.1.

**Table A.1:** Average transmission of optical density filters used in this work

S.NO	Optical densities (OD)	Average transmission (%)
1	0.1	85.43
2	0.2	65.09
3	0.2 + 0.3	46.34
4	0.4	39.81
5	0.5	31.62
6	0.6	25.11
7	1	10

The transmission of the optical density filters can be calculated using Equation A.1.

$$T(\%) = 10^{-OD} \quad (\text{A.1})$$

The transmission spectra of the different OD filters are shown in Figure A.1

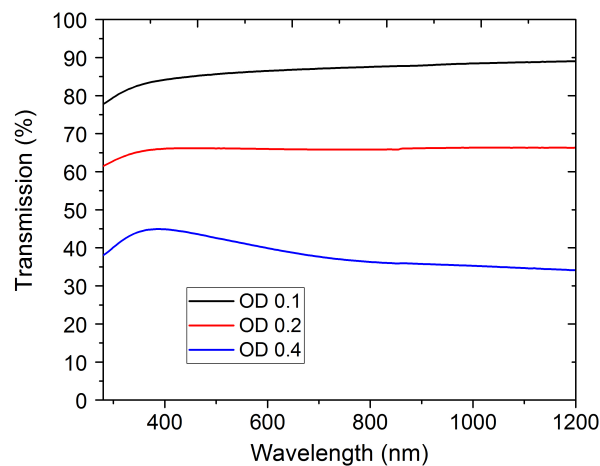


**Figure A.1:** Comparison of the transmission of different optical filters.



# B

## Appendix B

### B.1. Electrical parameters of p-layer for different RF power

**Table B.1:** Comparison of optical and electrical parameters of p layer with DYK.

Layer name	Growth rate (nm/min)	$E_{04}$ (eV)	$E_a$ (eV)	Conductivity $\times 10^{-7}$ (S/cm)
DYK- 5 W	6	2.17	0.43	7
1 W	2.76	2.01	0.47	5.91
2 W	6.1	2.03	0.47	4.69
3 W	7.89	2.05	0.49	2.87
4 W	9.14	2.06	0.50	1.59
5 W	12	2.08	0.51	1.56

**Table B.2:** Comparison of optical and electrical parameters of n-layer with DYK.

Layer name	Growth rate (nm/min)	E04 (eV)	Ea (eV)	Conductivity $\times 10^{-2}$ (S/cm)
DYK - 10 W	1.7	2.65	0.10	2.6
10 W	1.16	2.76	0.097	2.25
11 W	1.23	2.79	0.142	0.11
12 W	1.39	2.80	0.080	1.51
13 W	1.48	2.81	0.092	1.2
14 W	1.68	2.82	0.087	0.5